CHALMERS
UNIVERSITY OF TECHNOLOGY

Evolutionary optimization of steel truss footbridges

A study of parametric design and optimization in Karamba 3D, Galapagos and Octopus for different truss geometries

Master's thesis in Structural Engineering and Building Technology

VICTOR ANDERSSON
CECILIA HILLBERG

Department of Architecture and Civil Engineering
Division of Structural Engineering
CHALMERS UNIVERSITY OF TECHNOLOGY
Gothenburg, Sweden 2018
Master's thesis ACEX30-18-35

MASTER'S THESIS ACEX30-18-35

Evolutionary optimization of steel truss footbridges

A study of parametric design and optimization in Karamba 3D,
Galapagos and Octopus for different truss geometries

Master's thesis in Structural Engineering and Building Technology

VICTOR ANDERSSON
CECILIA HILLBERG

Department of Architecture and Civil Engineering
Division of Structural Engineering
CHALMERS UNIVERSITY OF TECHNOLOGY

Gothenburg, Sweden 2018

Evolutionary optimization of steel truss footbridges
A study of parametric design and optimization in Karamba 3D,
Galapagos and Octopus for different truss geometries
VICTOR ANDERSSON
CECILIA HILLBERG

Master's thesis ACEX30-18-35
Department of Architecture and Civil Engineering
Division of Structural Engineering
Chalmers University of Technology
SE-412 96 Gothenburg
Sweden
Telephone: +46 (0)31-772 1000

Cover: :
Warren sub model in Karamba 3D representing the case study over Genevadsån.

Gothenburg, Sweden 2018

Evolutionary optimization of steel truss footbridges
A study of parametric design and optimization in Karamba 3D,
Galapagos and Octopus for different truss geometries
Master's thesis in Structural Engineering and Building Technology
VICTOR ANDERSSON
CECILIA HILLBERG
Department of Architecture and Civil Engineering
Division of Structural Engineering
Chalmers University of Technology

ABSTRACT

In the early design phase of complex structures, there is often an urge of structural engineers to get detailed and informative preliminary designs, without compromising the constraint of time. According to the Swedish parliament and government, the environmental goals to have a sustainable energy provision and zero net emissions to the atmosphere in 2050, also affects the infrastructural sector (Ahston et al., 2017) and it is of importance to already in an early stage formulate viable propositions of designs with as little material as possible.

In this thesis a computational script and model of steel truss footbridges is created in Grasshopper and Karamba 3D respectively, which is based on the Swedish norms and regulations. The purpose is to optimize the models with the single- and multi-objective optimization plug-ins, Galapagos and Octopus, to minimize the mass and maximize the transparency of the structures.

Investigations, regarding steel truss bridges and parametric design, initiates the thesis constructing a knowledge which the next steps build upon. The model in Karamba 3D is first based on a real case from Ramböll, which it is verified with in FEM-Design and with hand calculations. Two additional geometries are added into Karamba 3D and verified the same way as before. All three sub models, which compose the three most common truss geometries Warren, Pratt and Howe, set the basis for an investigation of the optimization of the structures. The objectives of this thesis are to investigate if the results from Karamba 3D are reliable and what the difference in results from the single- and multi-objective optimization plug-ins Galapagos and Octopus are. In a second part, the most optimal bridge geometry is sought regarding given span lengths of 10 m, 20 m and 30 m, while having the width and a height constant for all sub models.

The results show that the model in Karamba 3D is reliable if the bridge deck is weakened with a factor 10 000. However, it needs to be stated that actions needed to be taken compensating for the differences in the results of the verification considering the utilization ratio of the elements and the global LT-buckling of the top chord. Additionally, the results proved that Octopus is the most beneficial plug-in and that the Howe sub model is the least suitable for all span lengths. The Pratt sub model proves to be most suitable for span length of 10 m and the Warren sub model for span length 20 m and 30 m, both considering mass and transparency. To conclude, the model, consisting of three sub models, can be used for a preliminary design to give an initial estimation of cross-sections and topology and also gives the opportunity to be further developed, adding more constraints if desired.

Keywords: Parametric design, Steel truss footbridge, Optimization, Karamba 3D, Galapagos, Octopus

Evolutionerande optimering av fackverks-GC-broar i stål
En studie om parametrisk design och optimering i Karamba 3D, Galapagos och Octopus for olika fackverksgeometrier
Examensarbete inom Building and Civil Engineering
VICTOR ANDERSSON
CECILIA HILLBERG
Instutition för Arkitektur och Samhällsbyggnadsteknik
Avdelning för Konstruktionsteknik
Chalmers Tekniska Högskola

SAMMANFATTNING

Behovet av att kunna formulera tidiga designförslag som är pålitliga och informativa är något som eftersträvas i tidiga skeden. Det är Trafikverkets vision att det år 2050 inte ska produceras några utsläpp överhuvud taget, vilket förstås också påverkar byggandet av infrastrukturen i Sverige. För att stödja dessa mål är det viktigt att kunna optimera och föreslå desginförslag som använder sig av så lite material som möjligt.

Målet med det här arbetet är att göra en parameterstyrd model av fackverks-GC-broar av stål i Karamba 3D som klarar de svenska normerna och kraven. Modellen ska därefter optimeras med två tilläggsmoduler, Galapagos och Octopus, för att kunna reducera massan och maximera genomsiktligheten av broarna.

En litteraturstudie om stålbroar och parametrisk design lägger grunden för att initiera modellering i Karamba 3D. Den första modellen baseras på en verklig bro som byggts över Genevadsån och har beräknats av Ramböll. Modellen i Karamba 3D verifieras med det verkliga fallet i FEM-Design och med handberäkningar. Därefter introduceras ytterligare två geometrier och verifieras på samma sätt. I nästa del ska dessa tre delmodeller - Warren, Pratt och Howe - optimeras med geometrin och profilerna av elementen som variabla parametrar. Delmålen i det här arbetet består av att avgöra graden på pålitligheten gällande kraven från Karamba 3D, undersöka vad som skiljer i resultaten mellan optimmeringen i Galapagos och Octopus och slutligen hitta den mest optimala geometrin och de bästa profilerna för en spannlängd av 10 m, 20 m och 30 m med en konstant bredd och höjd på bron.

Resultaten visar att modellen i Karamba 3D går att lita på om brobaneplattan försvagas med en faktor 10 000. Värt att nämna är skillnaderna som påvisades i verifieringen, huvudsakligen gällande utnyttjandegraden av vissa element samt den globala böjvridknäckningen av överramen på GC-broarna, som behövdes kompenseras för. Resultaten påvisar även att Octopus är den mest gynnsamma och tidseffektiva tilläggsmodulen vid optimering. Den mest optimala GC-bron för 10 m visar sig vara Pratt GC-bron och för 20 m och 30 m är det Warren GC-bron; detta med hänsyn till både massa och genomsiktlighet. Slutsatsen är att modellen kan användas för en preliminär design av tre fackverks-GC-broar som kan utgöra ett ungångsläge för vidare beräkningar och detaljer.

Nyckelord: GC-bro, Fackverk, Parametrisk design, Optimering, Karamba 3D, Galapagos, Octopus

CONTENTS

List of Figures

List of Tables

PREFACE

This master thesis has been written at the Department of Architecture and Civil Engineering, Division of Structural Engineering, at Charmers University of Technology as well as in collaboration with Ramböll Bridge Division in Gothenburg during the spring of 2018.

First, we would like to thank the Bridge Division at Ramböll, which gave us a lot of memories and joyful contributions during this master's thesis. Secondly, we would especially like to thank our supervisors at Ramböll, Georgi Nedev and Gustav Good, who showed great commitment and interest in this project.

Finally we would like to thank Joosef Leppänen, our supervisor and examiner at Chalmers University of Technology, who conducted and supported us during this semester.

Abbreviations

AM Additive manufacturing.

BOF Blast oxygen furnace.

CAD Computer aided design.

DLF Direct laser fabrication.

EA Evolutionary algorithm.

EAF Electric arc furnace.

FEM Finite element modeling.

GA Genetic algorithm.

HypE Hypervolume estimation algorithm for multi-objective optimization.

LENS Laser engineered net shaping.

LSF Laser solid forming.

MO Multi-objective optimization.

MOA Multi-objective optimization algorithm.

MOEA Multi-objective evolutionary algorithms.

MOP Multi-objective optimization problem.

NURBS Non-uniform rational b-spline.

SLS Serviceability limit state.

SPEA-2 Strength Pareto evolutionary algorithm 2.

ULS Ultimate limit state.

Nomenclature

Greek letters

χ_{LTmod}	Modified reduction factor for considering lateral torsional buckling
χ_{LT}	Reduction factor for considering lateral torsional buckling
γ_G	Partial coefficient for permanent load
γ_Q	Partial coefficient for variable load
C_{mLT}	Factor for equivalent constant moment
C_{my}	Factor for equivalent constant moment
C_{mz}	Factor for equivalent constant moment
k_{yy}	Interaction factor
k_{yz}	Interaction factor
k_{zy}	Interaction factor
k_{zz}	Interaction factor

1 Introduction

In the following sections the scope of the project is explained, starting with the background to the study and the aim and objective of the thesis, followed by a clarification of the demarcations and the method used.

1.1 Background

In the early design of complex structures, such as bridges, structural engineers and architects, often having conflicting goals, need to combine their special skill sets to design and analyze different conceptual designs. This process is often time consuming and little information is known about the project in its early stages, which makes it difficult to make informed decisions. The design choices made in the preliminary design phase will have precautions down the whole design chain, often resulting in more costly changes executed in a later phase than the preliminary design phase (Sharafi, Hadi, & Teh, 2013). This is an issue which the bridge department at Ramböll Sweden has reflected upon, resulting in a request to solve this matter.

Environmental, economical and time related profits are of importance, both considering the infrastructure globally and regionally, in Sweden. The Swedish parliament and government has a vision, based on the United Nation's framework for environmental goals (United Nations, 2018), to have a sustainable energy provision and zero net emissions to the atmosphere in 2050 (Ahston et al., 2017); this also affecting the infrastructural sector. These goals put an particular pressure on the ability to optimize structures correctly and time effectively. It needs to be stated that it is the responsibility of the consultant to already in an early stage consider the environmental and economical aspects and optimize them if possible.

Many studies have been made on the topic of structural optimization using varying kinds of software and methods (Rothwell, 2017; Camp, Pezeshk, & Cao, 1998; X. S. Yang, 2010; Sharafi et al., 2013; Nanakorn & Nimtawat, 2013). Most of the studies on optimization of bridges have been carried out on truss bridges (Balling, Briggs, & Gillman, 2006) and the parameter optimized is often the weight of the structure. However, there are optimization algorithms that can be used to optimize multiple parameters (Martini, 2015; Coello Coello, 2006). There have also been advances in the field of parametric design which is the design using changeable parameters instead of statically input values. Parametric design allows the designer to quickly analyze different design parameters without redoing the whole design process. The contribution of the advancing technologies in the steel industries, allowing more precise and complex parts to be produced, also pushes the optimization in production towards the realization of the preliminary design. The combination of all parts - parametric design, optimization tools and the ability to produce the wanted sections - finally leads to the possibility to make informed decisions early, resulting in environmental, economical and time related benefits.

1.2 Aim

The aim of the thesis is to create a computational model of steel truss footbridges in Rhinoceros and Grasshopper with the plug-in Karamba 3D, based on current norms and regulations in Sweden. This model is based on a case study, which gives the possibility to verify it with a model in FEM-Design and hand calculations. The created model in Karamba 3D is then optimized with the plug-ins Galapagos and Octopus, which entails to minimize the steel tonnage an to maximize the bridge transparency as much as possible presuming that all the requirements, for ultimate limit state (ULS) and serviceability limit state (SLS), are fulfilled. The intention of the optimization is to reduce the material use for propositions of steel truss footbridges in an early design, leading to a profit in terms of environmental and economical aspects. Additionally, it is of interest to evaluate the reliability of the optimized results and its potential use for further projects in the future, to get answers which type of truss is most efficient.

1.3 Objective

This thesis starts with accomplishing a literature study, studying the steel in its relation to its emissions during production and the standard dimensions of steel profiles and its place in the optimization world. Further, optimization techniques and parametric design are investigated to identify possibilities and good choices when optimizing models. Subsequently, the answers to following questions are sought, which reassemble the objectives of this thesis:

- Are the parametric models in the FE-solver Karamba 3D and its results reliable?
- Is there a difference between the results from the single-objective optimization plug-in Galapagos and the multi-objective optimization plug-in Octopus?
- Which bridge geometry - Warren, Pratt or Howe - is the most optimal one for the given span lengths of 10 m, 20 m and 30 m, having the bridge width and height constant?
- Can this created script in Grasshopper in the end contribute to more precise, informative and also time efficient results in an early stage of preliminary design?

1.4 Demarcations

In the scope of this report the designed bridge is presumed to be located in Sweden and the focus is restricted to the superstructure of steel truss footbridges. Truss types studied in this report are the Warren, Pratt and the Howe truss. The spans treated are 10 m, 20 m and 30 m and the loads used in the calculations are the self-weight of the construction (permanent load) and the crowd load (variable load). The study is focusing on the global behaviour of the truss bridges, meaning that local effects and details are neglected as it is not of prior interest in a preliminary design.

1.5 Method

The first part of this thesis consists of a literature study, giving fundamental knowledge to proceed and start developing a script in Grasshopper. The first sub model, created with Karamba 3D, is a Warren truss bridge, based on an existing case recently executed by Ramböll over Genevadsån. The verification of this model with the Strusoft FEM-Design model of the case includes a convergence study investigating the impact of the stiffness of the bridge deck on the normal force of all elements of the bridge. Further, the sectional forces, the maximum displacement, the natural frequencies and utilization ratio of all elements from Karamba 3D are compared with the results in FEM-Design. To broaden the range of choices, two additional geometries, the Pratt and Howe trusses, are added to the script in Grasshopper and the results from Karamba 3D verified with FEM-Design and hand calculations.

Once the three developed sub models are verified, the structures are optimized using the evolutionary single- and multi-objective optimization plug-ins Galapagos and Octopus. To achieve an optimal solution, the model needs to fulfill all design criterion, when reducing the mass and increasing the transparency of the footbridge. The following criterion were considered during optimization:

- Maximum allowable deflection of the footbridge (SLS)
- Cross-sectional capacity of the elements (ULS)
- Global lateral torsional buckling of the top chord (ULS)

Part 1 of the optimization comprises to evaluate the differences of the results from Galapagos and Octopus, having the case study as an initial condition when optimizing. In part 2 of the optimization, the focus lies in the achievement of the optimal solution considering given span lengths of 10 m, 20 m and 30 m of the footbridges, having the height and width constant for all three sub models.

2 Steel truss footbridges

The truss design belongs to the modern era and was rather slow developed compared to the other four basic bridge types: The beam, the cantilever, the suspension and the arch (Troitsky, 1994). It is said that Leonardo da Vinci was the first one to realize the strength of triangular structures which the truss is composed of. The diagonal and/or vertical members, see Figure 2.1, also referred to as web members, carry the shear force, either in tension or compression (Duan, 2017). The top and bottom chord, see Figure 2.1, carry the bending moment. The truss bridge became popular in the 19th and 20th centuries since the design is material efficient and can carry large loads (Rutgersson, 2008). An explanation of the most relevant parts of a truss bridge are described more in Figure 2.1.

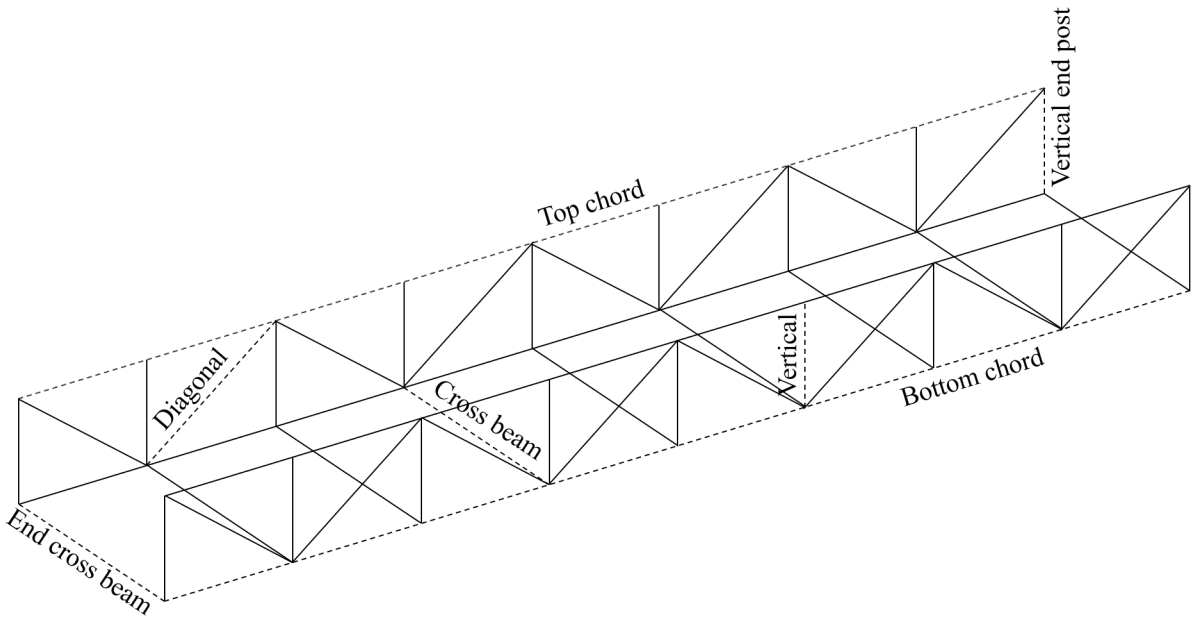

Figure 2.1: Explanation of the different parts in a truss bridge.

The truss bridges can be categorized into three main categories, depending on the location of the bridge deck and where the supports are put: Deck, half-through and through truss bridges, which can be seen in Figure 2.2 (Duan, 2017). The through bridge indicates that the bridge deck is put on the bottom chord, whereas the deck truss bridge has the bridge deck located on the top chord. For larger bridges, the section is closed in case of a through truss bridge, meaning that the users of the bridge must be able to pass under the top chord. The half-through bridge is a combination of the two mentioned before, having the deck between the top and and bottom chords.

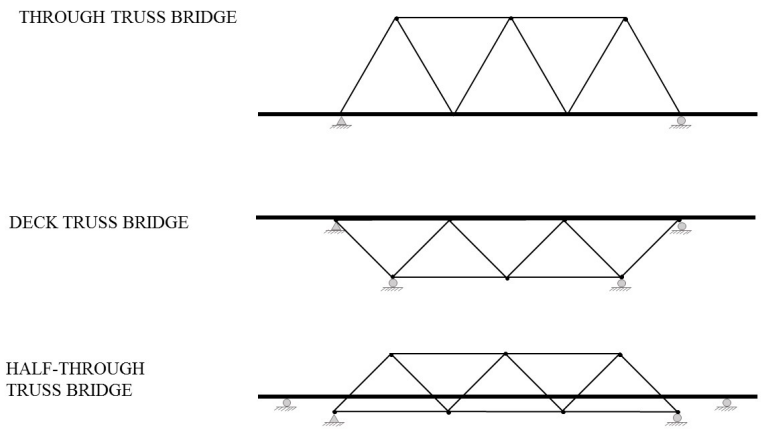

Figure 2.2: Three main categories (start from top): Through, deck and half-through truss bridge.

As can be seen in figure Figure 2.3 there are different types of concepts when it comes to bridge trusses (Kassimali, 1993). The Warren truss bridge is the most common one in which its web members take either tension or compression (Duan, 2017). The Pratt truss bridge is another concept, which concludes in the diagonals taking tension and the vertical members carrying compression. The Howe truss is similar to the Pratt truss, having the diagonals rotated 90 degrees, making them take compression and the verticals tension. There are several other concepts, being versions of the ones mentioned above, which are further subdivided in triangular formations. Two examples are the Baltimore truss and the K truss.

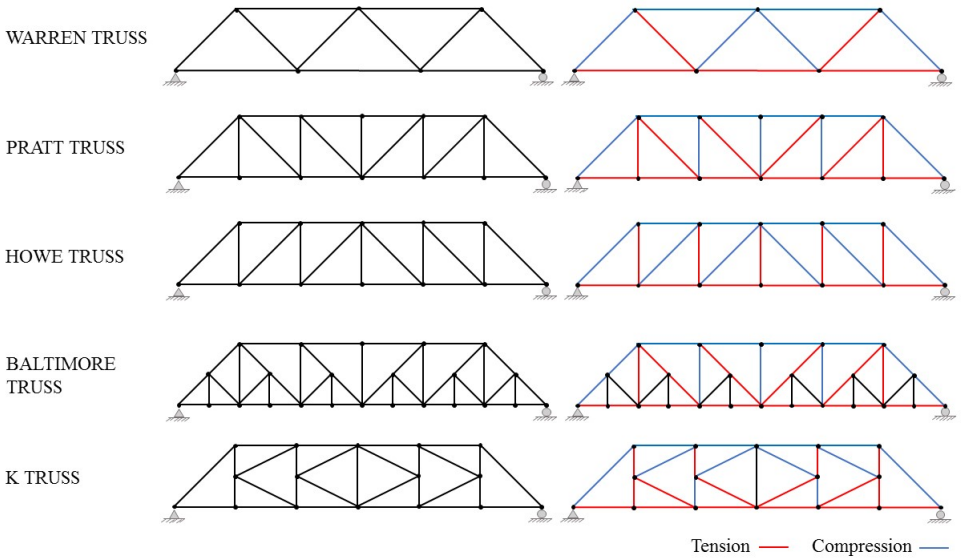

Figure 2.3: A visualization of different truss bridge concepts. To the right, only considering the self-weight, the load distribution of the members of the truss bridge concepts is presented.

The drawbacks of steel truss bridges are that they are expensive to maintain and require a lot of field labour because of the jointed layout of the members, which also makes the design hard to access for maintenance (Troitsky, 1994). The joints are considered as a risk zone often resulting in some kind of damage (Mehrjoo, Khaji, Moharrami, & Bahreininejad, 2008).

For instance, fatigue damage is often triggered by micro cracks caused by for example welding at the joint locations. These are also hard to visually recognize during inspections. Another drawback that is common for all light weight structures is that they are susceptible to dynamic problems (Craigh & Kurdila, 2006). Some of the advantages using a truss design is that the construction of the bridge can be built in a factory without interfering with the traffic (Ronnenbrant & Glans, 1996). The design of truss bridges is also very efficient in taking care of the loads and at the same time allowing some level of transparency. Nowadays truss bridges in Sweden are a common choice when designing footbridges.

2.1 Steel as a construction material

Metals have been used by mankind for a very long time, even giving names to historic periods like the Bronze Age and Iron Age (Domone & Illston, 2010). The properties are strong, hard and offered good perquisites, ideal for weapons for instance (Wagner, 1996). In the 18th century the production of iron was possible in a larger scale, probably first produced in China. The high temperature needed, to melt iron, was achieved using a forced air blast using coke as fuel (Domone & Illston, 2010). The product, binding with carbon from the fuel, is called pig iron or cast iron and could easily be shaped and used for larger structures. The manufacturing of iron was also significant in the early 19th century as the Industrial Revolution took place. The production of steel is a necessary part of many structures in peoples everyday life and the amount increases as the magnitude of the world's population does (Miljönytta, 2018).

Starting at a microscopic plane of description, metals consist of an atomic structure, where a net positively charged nucleus is surrounded by a cloud of orbiting, negatively charged electrons (Domone & Illston, 2010). Overall, the atom is electrically neutral, presuming that the number of protons and electrons are equal. The property of an element is very dependent on the number of electrons in the outermost layer of an atom. These so called valence electrons are the ones most likely to bond with other atoms, resulting in different properties of an element. Metallic atoms, compared to other atoms, have valence electrons which are able to move freely and therefore build structures, which are arranged in a crystal lattice (Berns & Theisen, 2008). This state gives metals the ability of a high thermal and electric conductivity (McGuire, 2008). Due to the freely moving valence electrons, it is possible to alloy different metals, having similar or slightly smaller sizes of the atoms, resulting in different properties of a metal (Mandal, 2015).

There is a great range of possible compositions of steel (Bhadeshia & Honeycombe, 2006). Only a small amount of carbon is enough to form iron to the strong and mostly tough alloy called steel, compared to iron which is rather soft. Steel is often categorized into two groups, one being plain carbons and the other being alloy steels (Mandal, 2015). During the production of plain carbon steel, no alloying components are added intentionally; thus small amounts of alloying substances can appear and be implemented during production. Alloys can be defined as a composition of iron and other components, but alloys without carbon are usually called irons (Krauss, 2005).

2.2 Steel in relation to its emissions

The environmental sustainability has been an important issue for years and forms the everyday life, inter alia it influences the infrastructure in Sweden (Ahston et al., 2017). The road and railway infrastructure is responsible for 1-2 millions emissions of carbon dioxide equivalents, which represents 5-10 % of the total emissions from vehicles, infrastructure and traffic in Sweden. The Swedish parliament and government has a vision, based on the United Nation's framework for environmental goals, especially sub section 11 (United Nations, 2018), to have a sustainable energy provision and zero net emissions to the atmosphere in 2050 (Ahston et al., 2017).

To reach this vision, Trafikverket (Swedish Transport Administration) has decided to demand a decrease of the emissions of 15 % until 2020 and 30 % until 2025, which finally ends up in a zero release of emissions in 2050 (Ahston et al., 2017). These percentages are referring to a representative value from 2015. It is also the goal of the Swedish Transport Administration to ensure an economical benefit throughout all processes, without compromising the long-term infrastructural goals with respect to the environmental and social aspects. The goals are to create a society with a developing infrastructure, entailing an improvement in efficiency concerning time, costs and performance.

Steel production is energy, resource and emission intensive (World Steel Association, 2018b), a lot depending on for instance the way of production, the coal and iron ore used and composition of the steel product (World Steel Association (WSA), 2015). Approximately 93 % of all greenhouse gas emissions caused by the steel industry consist of carbon dioxide emissions, which is an issue to be solved (World Steel Association, 2018b). The advantage is that steel components of structures can be recycled almost infinitely without deteriorating in quality (Domone & Illston, 2010).

There are mainly two ways to produce carbon steel (World Steel Association, 2018a). One way of manufacturing steel entails retrieving iron from iron ore in the blast oxygen furnace (BOF), which according to World Steel Association is the most common method used globally, representing 70 % of the production. In the blast oxygen furnace the pig iron is molten in a furnace, where oxygen is blown into (Rennie, 2016). The temperatures reach about 1250 degrees and the final product is molten steel, which is poured off. The BOF way of production is mainly used to produce both long and flat steel products, where in this case high-quality scrap (pre-consumer scrap) also can be recycled (Xylia, Silveira, Duerinck, & Meinke-Hubeny, 2017).

The second way of production is meant for the purpose to recycle the increasing amount of steel scrap, where an electric arc furnace (EAF) is used (Xylia et al., 2017). In the electric arc furnace an electric arc induced by electrodes is created, producing heat, which melts the metal (Rennie, 2016). Low-quality scrap (post-consumer scrap) can be recycled and is mostly formed into long products, but also used for the production of special kinds of steel as for instance stainless steel (Xylia et al., 2017). In this way of production and with the increasing recycling of steel scrap, less energy is used, to be exact 56 % less energy than with the BOF, ending up in an advantage not only environmentally, but also considering the economic energy costs. In the year 2050 it is predicted that the scrap availability of steel versus the production of crude steel, which means steel in its first solid state after it has been melted, will be at the same amount, indicating the importance of an environmental friendly disposal.

Considering the crude steel production globally, it has increased quite dramatically during the last 50 years, mostly due to the industrialization in China, Brazil, India, Iran and Mexico (World Steel Association, 2017). In 1950 approximately 189 million tonnes of crude steel were produced, with Europe as the leading producer representing 33.5 % of the total world's production and North America ranked second representing 25.8 %. In 2016 the production had increased to 1630 million tonnes of crude steel, having China as the main producer (49.6 %) and Europe ranked second representing 12.3 % of the total. Today many efforts are made to decrease the magnitude of emission, which in fact has resulted in a decrease of 50 % in specific energy consumption in iron and steel production, considering the last 30 years (Xylia et al., 2017).

In Sweden steel is produced in 3 ore based plants, 10 plants based on scrap and 15 plants focusing on the processing of steel (Miljönytta, 2018). The ore based plants cover approximately two thirds of the steel production in Sweden. The steel industry being a big part in the export business, representing a value of ca 41 billions of Swedish crowns, corresponding to 3.4 % of the total export of goods to approximately 140 different countries. The unsolved issue is the release of carbon dioxide, mainly caused during the reduction from iron to pure iron using coal or coke. This has started a cooperation project in northern Sweden in 2016 with the aim to produce iron without any carbon dioxide emissions at all. This could be achieved using hydrogen gas instead of coal and coke, which nowadays partly is imported from Australia (LKAB, 2018). The plan is to use hydrogen gas, produced with Swedish fossil free electricity, in which case the rest product would be water. If this vision becomes true, it would entail a reduction of the total carbon dioxide emissions in Sweden by 10 %.

2.3 Standard dimensions of steel load-bearing profiles

The purpose to optimize a structure at an early stage is that it can be realized in the end, implying that it is necessary to have the possibility to manufacture the optimized shapes wanted (Bates & Fistructe, 1991). The standard dimensions of structural elements as they are known today, started to evolve as regulations and standards were introduced. These were introduced in the early 19th century as the quantity and size of structural sections were increasingly produced in line with the rapid development of usage of steel as a structural material. Standard dimensions, generally cast and forged, can represent a limitation if a complex structure is longed for (Zietala et al., 2016). Parts need to be welded and connected to each other, resulting in weak spots exposed to corrosion for instance.

Today there are technologies available, allowing complex parts to be produced (Zietala et al., 2016). So called laser-additive manufacturing entails producing a layer-by-layer reproduction of a computer aided design (CAD), using powder, which is melted and added. The additive manufacturing (AM), also called 3D printing, has been developing since the 1980s (Gu, 2015). Today the AM is most commonly used with plastics, metals and alloys. There are several ways of laser additive manufacturing today, for instance direct laser fabrication (DLF), laser solid forming (LSF) and laser engineered net shaping (LENS) (Zietala et al., 2016).

The advantages of the laser-additive manufacturing is the time efficient production as the procedure is executed in one step (Gu, 2015). Not only is this a way of production allowing complex shapes to be manufactured, but also it is cost effective bypassing the need to transport products; rather producing them closely to the site where it is needed. Additionally, considering the environmental aspect, the laser-additive manufacturing leaves no waste behind, as the product is built, adding layer-by-layer,

with the exact amount needed. The costs of AM versus traditional manufacturing is depending on the quantity of the production (Dumitrescu & Tanase, 2016). Regarding the traditional way of manufacturing, costs for tools are included and implying an increased production to result in a decrease of costs. The costs for the AM, which does not require tools, are kept constant, regardless the extent of production. This entails that a small production with AM is less expensive compared to the traditional manufacturing, whilst a large production could mean that AM is more expensive.

The additive manufacturing method is nowadays mainly applied in the aerospace, automobile, biomedical and defense sector (Gupta, 2017). There are few examples where the method is used in the construction sector to build bridges though (Eindhoven University of Technology, 2017) and (infra, 2017). In Europe there have been some examples, where footbridges have been 3D-printed, one example being a cycle bridge in Gemert in the Netherlands, where a 8 m long bridge was printed with pre-stressed, reinforced concrete. Another example in the Netherlands, more accurate considering the focus of this thesis, is a 12 m long footbridge made out of stainless steel, which is printed in a lab and is to be installed in 2018 (Dunning, 2017). It is the first 3D-printed bridge in this scale and is to be placed across the Oudezijds Achterburgwal in Amsterdam.

The development of 3D-printing is improving and the prediction is that it will be more adapted and used in a large number of industries in the future (Kianian, Tavassoli, Larsson, & Diegel, 2016). Whilst the increased utilization of AM world wide, including countries close by like Germany and the United Kingdom, Sweden has shown a retraction regarding the use of AM, beyond its use for prototyping. A reason could be the lack of standards for the AM (Larsson, 2016). A study from 2016 is thus stating that the majority of the AM users in Sweden are expanding, finally leading to the possibility to participate in the global competitiveness (Kianian et al., 2016).

3 Optimization and parametric design

In the following chapters different optimization techniques as well as the concept of parametric design are explained. Additionally some software that can be used for parametric design are introduced and described.

3.1 Optimization in structural engineering

Any optimization problem can be defined by a maximization or minimization problem (Hasançebi, Çarbaş, Doğan, Erdal, & Saka, 2009). Even though there is a large variety of optimization methods available for designers to use, the designers are often still bound to the standard dimensions of steel produced by the steel mills. Due to the improvements and evolution of the steel industry explained in Section 2.3, there are now potentially more reasons to optimize structures.

Optimization in the early stages of the design process can help saving material (Rothwell, 2017). The weight reduction can help creating light weight structures to counteract the high cost of today's high performance materials. Reducing the weight of the cross-section not only generates less material costs but also decreases the manufacturing and operational costs (COX, 1965). However, material reduction have some drawbacks as well (Rothwell, 2017). Light weight structures entail an increased slenderness of the structure having the consequence of an elevated risk of buckling. This is an example of two conflicting goals, where a decrease of the buckling risk implies that more material is needed, resulting in a higher cost. The conflict between these two goals can be handled using optimization tools (Beck & Gomes, 2012).

Conventional design methods, as stated in Eurocode (EC), are used to get as close to the recommended design values as possible. The design process is carried out and then repeated, parameters modified and analyzed until satisfactory terms are met, for instance an acceptable utilization ratio of the cross-sections (Nanakorn & Nimtawat, 2013). This process often demands many iterations until the design criterion is met (Rothwell, 2017). Drawbacks with the conventional design process are time consuming calculation processes and the selected focus on only one parameter. In the design of a structure there are often several conflicting design parameters which make it hard to find a optimal design using the conventional design method (Coello Coello, 2006). To get a more efficient structure, design methods that can handle and optimize several design parameters are needed.

3.1.1 Optimization techniques

The optimization techniques can basically be divided into two categories, one being the deterministic algorithms, the other being the stochastic algorithms (X.-S. Yang, 2010). The deterministic method can be described as a procedure which can be repeated, resulting in the same outcome if the same starting values are used. The stochastic algorithm on the other hand includes some random numbers, resulting in different outcomes each time the procedure is repeated. In the end, the results of the two methods are similar.

As can be seen in Figure 3.1, the different optimization techniques can be divided into one-dimensional and multi-dimensional methods (Sahab, Toropov, & Gandomi, 2013). The multi-dimensional methods are divided further into continuous and discrete methods (Black, Hashimzade, & Myles, 2017) and

(Colman, 2015). The difference between discrete and continuous methods is that variables used, can only take a certain number of values in the discrete case, whereas an infinite number of possible values within a given span can be taken in the continuous case.

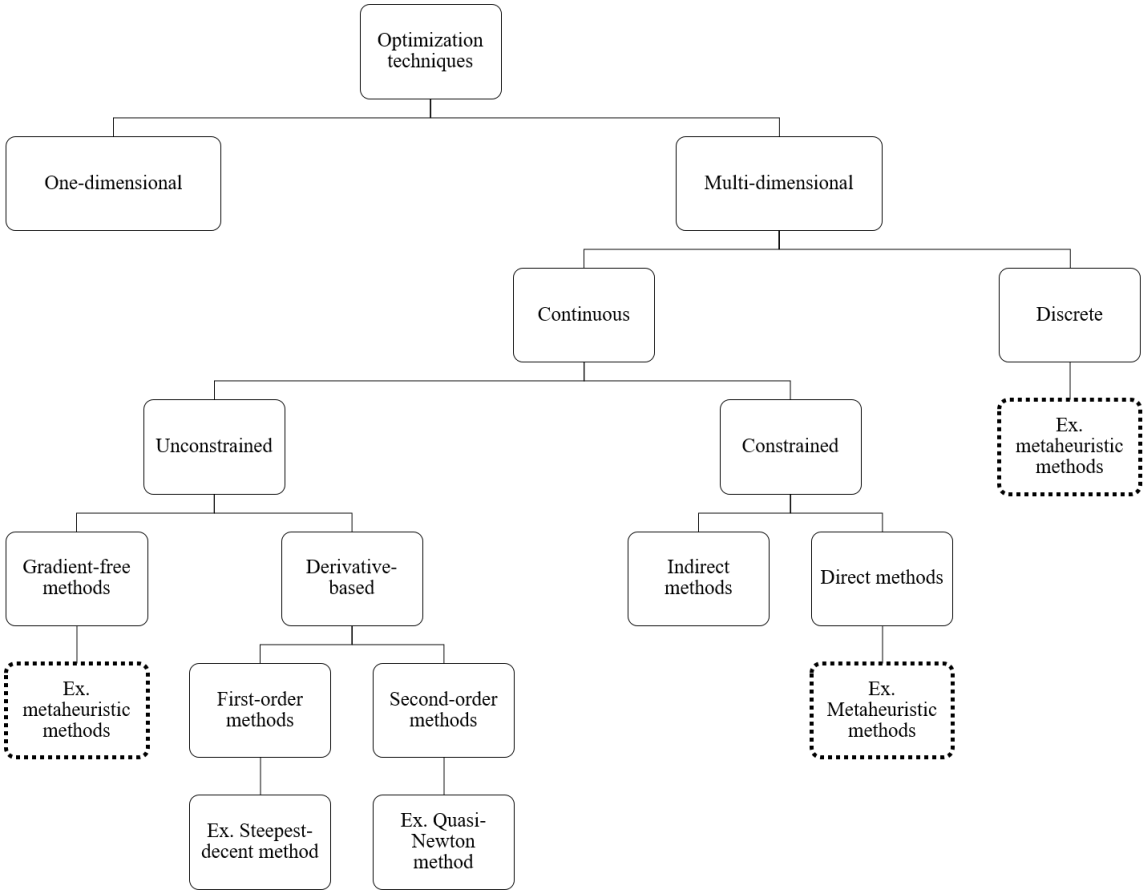

Figure 3.1: Classification of optimization methods, modified after an original by (Sahab, Toropov, & Gandomi, 2013).

In order to understand the different optimization techniques, the fundamentals need to be explained, which can be done using a problem defined with Equations (3.1) to (3.4), also called the generic form of a problem (X.-S. Yang, 2010). The functions $f_i(x)$, $h_j(x)$ and $g_k(x)$ are called objective or cost functions, which describe the design vector. It is also possible to shift the objective functions representing a maximization problem instead of a minimization problem, where $g_k(x)$ could be larger than 0, see Equation (3.3). The design or decision variables x in Equation (3.4) are real numbers and the variable *i* describes the search or design space as is expressed in Equation (3.1).

$$Find\ \mathbb{x}_i \in \mathbb{R}\ to\ minimize\ f_i(x),\ (i = 1, 2, ..., M) \tag{3.1}$$

$$h_j(x) = 0, (j = 1, 2, ..., J) \tag{3.2}$$

$$g_k(x) \leq 0, (k = 1, 2, ..., K) \tag{3.3}$$

$$\mathbb{x}_i = (x_1, x_2, ..., x_n)^T \tag{3.4}$$

A problem can either be single-objective, where $M = 1$, or multi-objective, where $M > 1$ (X.-S. Yang, 2010). If J and K, also called constraints, are equal to zero, the problem is unconstrained. Should there not be any objective at all, but only constraints, it is called a feasibility problem. Some of the most basic unconstrained numerical methods are zero-order methods, see Figure 3.1, also called gradient-free methods as for instance the Hooke's and Jeeves' method, explained in Appendix A.1 (Rothwell, 2017). Gradient-based methods, also called derivative-based, like first and second-order methods, further explained in Appendix A.1, which can also be seen in Figure 3.1, are related to the unconstrained optimization problems (X. S. Yang, 2010). First-order methods, like the steepest descent method, give a linear approximation to the objective function, whereas second-order methods, like the Quasi-Newton method, uses the second-order derivatives to improve the search direction at each iteration (Rothwell, 2017). The gradient-based methods result in an improved convergence regarding the optimization process compared to the gradient-free method (Martini, 2015).

Logically if there are values for J, K or both, the problem is constrained (Sahab et al., 2013). In structural optimization design the building codes, for instance Eurocode, usually represent the constraints. There are two subcategories to the constrained optimization: The indirect and direct method, see Figure 3.1. The indirect method starts to find optimal conditions of a function and discretizes it afterwards, whereas for the direct method it is the other way around (Potschka, 2014). The advantage of the direct method is that the result is generic.

3.1.2 Metaheuristic algorithms

Metaheuristic algorithms are a family of stochastic algorithms and have become popular in civil engineering to optimize truss structures, seismic analyses, traffic flow analyses, lay-out designs of floor beams and many more applications (Gandomi, Yang, Talatahari, & Alavi, 2013b). Metaheuristic means higher level and are often stochastic algorithms with randomization and global exploration. Metaheuristic algorithms can be used in a variety of optimization problems, for instance for discrete, constrained and unconstrained optimization as can be seen in Figure 3.1, which is a factor why it is an advantageous technique commonly used.

Compared to traditional numerical optimization, solvers based on metaheuristic algorithms are inspired by nature, mimicking optimization processes in nature, one example being Darwin's law of "survival of the fittest" (Gandomi, Yang, Talatahari, & Alavi, 2013a). In a metaheuristic algorithm each solution is called an individual and forms a large pool of solutions called a population (Rothwell, 2017). One benefit with metaheuristic algorithms is that due to their stochastic behaviour they cover a larger part of the design space than traditional solvers. As individuals will be generated all over the design space, it increases the possibility to find a local optimum, where a local optimum is a solution that is optimal within its closest neighboring solutions. Since the first population defined by metaheuristic algorithms is stochastically generated, there is no need for an initial guess to start the computation (Sahab et al., 2013).

The metaheuristic algorithms use two different features to search for solutions, the intensification and the diversification (X.-S. Yang, 2010). Intensification, also called exploitation, means directing the focus to a local area, concentrating to select the best solution (Gandomi et al., 2013a). The diversification on the other hand, called exploration, is the process of generating many different types

of solutions to facilitate the global search space, making it more efficient. Diversification is used to make sure the solutions do not get trapped in a local optimum. It is important to find a balance between the two features, avoiding difficulties due to convergence if the intensification is too dominant, or complications finding the global optimum if the diversification is influencing more (X.-S. Yang, 2010).

One of the metaheuristic algorithms is the evolutionary algorithm (EA), which is combining the intensification and diversification. Evolutionary algorithms are based on the inspiration on the biological evolution in nature (Sahab et al., 2013). The most commonly used evolutionary algorithm is the genetic algorithm (GA), which is a solver trying to replicate a natural selection process where the "best" (fittest) solutions, also called individuals, in a population is evolved (Simon, 2013). This algorithm is, as in the natural selection process, based on the facts that the population is diverse and that each individual has a finite life span and is able to reproduce. In a GA the first generation of individuals is randomly generated, resulting in some of them having high and some having low fitness (Sahab et al., 2013). Individuals with high fitness are more likely to survive and reproduce, which is why the individuals with low fitness are removed (Simon, 2013). To create a second generation, the individuals from the first generation (parents), having a high fitness, will cross-over (mate) with each other and thus create a new population (children). The cross-over process gives the children a combination of "genetic" information from the parents. This process is replicating Darwin's theory of natural selection. Since the individuals with high fitness will mate, their offspring will achieve a higher fitness and thus get closer to an optimum solution.

Another way to increase the fitness of a population is to use a so called penalty function (Smith & Coit, 1995). The idea of a penalty function is to penalize bad or unfeasible solutions so that the fitness of the population is not decreased. The penalty function can be seen as a barrier that hinders solutions that violates the constraints from being considered. Once a solution violates the constraints the penalty function changes the fitness value of the solution so it gets a really low fitness, thus hindering the solution from being considered.

If there is a small variety in a population there is a risk of inbreeding. In the terms of evolutionary computing, this means that the solution would not converge and the iteration hits a dead-end (Simon, 2013). To avoid inbreeding, some sort of mechanism is needed to apply more diversity to the population (Camp et al., 1998). Thus the concept of mutation is introduced, which in the context of GA entails changing one of the parameters in the offspring when cross-over takes part, creating new unique individuals (Simon, 2013). This creates a larger diversity in the population and reduces the risk of inbreeding. A balance is sought to avoid inbreeding, having a too small rate of mutation, and to bypass the behaviour of a random number generator when having a too large amount of mutation. The diversification will affect the convergence of a GA, but it is also highly dependent on the choice of population size, fitness function and other parameters (Gandomi et al., 2013a). GAs are commonly robust but take long time to reach a global optimum, meaning a slow convergence rate (Mitropoulou, Fourkiotis, Lagaros, & Karlaftis, 2013).

Other than GA there are several other evolutionary algorithms, for example evolutionary strategies and evolutionary programming (Simon, 2013). All algorithms are based on the same framework but have different foci on the population size, the recombination, the extension of mutation and fitness evaluation for instance.

Problems in civil engineering are seldom so easy that they can be defined by one simple goal and thus the need arises for multi-objective optimization algorithm (MOA) (Simon, 2013). Often EAs are modified and used in multi-objective optimization (MO) (Mitropoulou et al., 2013). When optimizing single-objective problems the goal is to find the best solution to a single objective (Tapabrata, 2018). Even though the process might be straight forward, there are a lot of parameters that need to be taken into account even when using single-objective optimization (Simon, 2013). Logically, for a multi-objective optimization problem (MOP) the complexity is further increased. In MOP there is no single solution that is optimal but rather several solutions that are compromises of different objectives (Mitropoulou et al., 2013). To validate if a specific combination of solutions in a MOP is good enough, a different approach to standard single-objective optimization is needed. In MOP the best trade-off between several objectives is explained using a set of Pareto-optimal solutions (Martini, 2015).

Looking at Figure 3.2, the Pareto-optimal solutions can be explained (Martini, 2015). The two axes represent two objective functions, f_1 and f_2, and the points (A to E) show different solutions of the problem (Martini, 2015), as there is hardly ever just one single solution that will be an optimum when using MOAs (Mitropoulou et al., 2013). The set of solutions are often compromises between different objectives, which implies that a change of an objective cannot be increased without decreasing another objective. As the minimum value is sought in the example, see Figure 3.2, B is a better solution than C, and D is better than E, having the smaller value in either one or both objective functions, i.e lower fitness (Martini, 2015). This implies that B is dominant compared to C, and D dominates E, thus solutions C and E are called dominated solutions. Looking at the solutions B and D, neither of them dominates the other, showing an example of non-dominance. The solutions A, B and D are called non-dominated front or Pareto-optimal set, as they represent a set of solution, which are non-dominant towards each other.

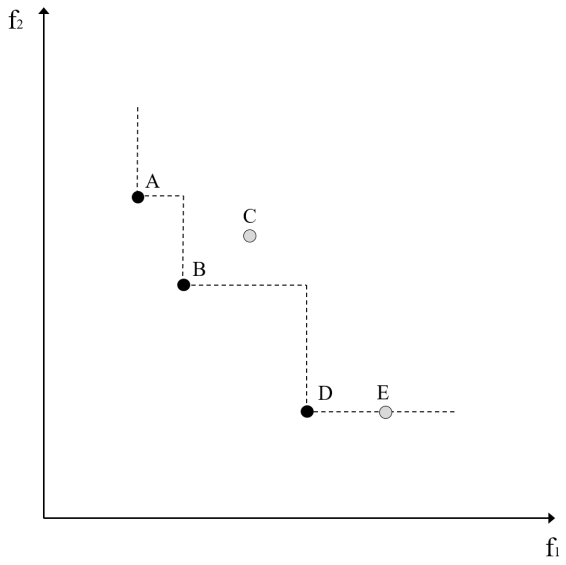

Figure 3.2: A graph explaining the Pareto-optimal set, which is represented by the black points, A, B and D.

There are classical gradient based methods which can solve MOPs, thus not very efficient yet, which can result in a single solution instead of a set of solutions (Tapabrata, 2018). Gradient based methods have difficulties handling the shape of the Pareto-optimal set, if the shape is concave

(Coello Coello, 2006) or if the function is discontinuous (Tapabrata, 2018). EAs do not have this problem and can handle the convex shape of the Pareto-front, which is one advantage of EAs in MOP, also known as multi-objective evolutionary algorithms (MOEA).

Even though non-dominated solutions have been found in a generation it is not sure that this solution is the best for another generation (Coello Coello, 2006). There is a risk that good solutions can be lost in the process of mutation or cross-over, making the new offspring having lower fitness than the parents (Gro, Oltean, & Oltean, no date). To make sure that the best non-dominated solution is always found and kept some MOEA have a method for storing non-dominated solutions in a archive, also know as an secondary population, from a generation and comparing these to other generations. This concept is called elitism and is used to find the best non-dominated solutions for all generations. If better individuals are found, the secondary population is updated with these individuals.

One of the more advanced MOEAs that uses elitism are the strength Pareto evolutionary algorithm 2 (SPEA-2) (Coello Coello, 2006). In addition to the archive with previously found non-dominated solutions SPEA-2 uses a ranking system called strength. The strength is calculated based on how many other individuals an individual is dominating as well as how many individuals are dominating it. The fitness is calculated based on the strengths of all non-dominated solutions in the current and secondary population. When calculating the fitness, SPEA-2 also considers how close the solutions are to the Pareto-front as well as the distribution of individuals. This is used to keep the individuals evenly distributed on the front. The algorithm also preserves solutions that are boundary solutions.

Another advanced MOEA is the hypervolume estimation algorithm for multi-objective optimization (HypE) (Bader, Zitzler, & Rudolph, 2010). HypE optimization methods works similarly to SPEA-2, but instead of using the strength of the solutions to determine the fitness, it uses the hypervolume, meaning it measures the area underneath the Pareto-front, which represents the area dominated by the Pareto-optimal solutions (Bader & Zitzler, 2011). Since HypE wants to find the largest hypervolume it turns the multi-objective optimization problem into a single-objective problem, as only the hypervolume is optimized. The unique thing about hypervolume calculation is that it is non-decreasing, monotonic, with respect to Pareto-dominance, meaning that a Pareto-optimal front is achieving the largest hypervolume. The main drawback of hyper volume based optimization methods is that they are highly demanding with regard to computer power.

3.2 Parametric design

In parametric design the geometry of a structure is based on parameters that can be changed (Dominik Holzer, Richard Hough, 2007). This is opposed to static analysis where the input values will remain the same through the design process. Using parametric design the variables and algorithms used allows the designer to quickly change the layout of the design by changing the initial parameters without redoing the design.

The benefit of using parametric design tools to integrate the work of both architects and structural engineers is that the structural optimization can be done during the structural design phase (Dominik Holzer, Richard Hough, 2007). In this thesis different parametric design software are used to optimize steel truss bridges, which are explained in the following chapters.

3.2.1 Rhinoceros

Rhinoceros (Rhino) is a 3D modeling tool commonly used by architects and designers in the early design phase (McNeel, 2018). Rhino uses non-uniform rational b-spline (NURBS) which are mathematical representations of a 3D geometry. NURBS are very flexible and uses little information to represent a shape (Ruiz-Geli, 2017). In this thesis Rhinoceros version 5.0 has been used. In Figure 3.3, the different software used in this thesis are displayed. It can be seen that Rhino is the basis software, having a first plug-in to Rhino called Grasshopper. As plug-ins into Grasshopper, Karamba 3D, Galapagos and Octopus are used. The different plug-ins are explained in the subsections that follow.

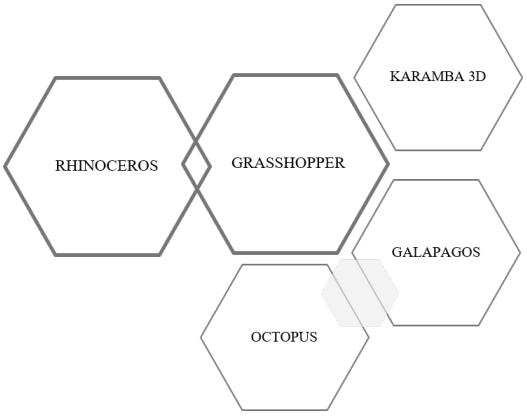

Figure 3.3: Schematic overview of the software that form the parametric design script.

3.2.2 Grasshopper

Grasshopper is a visual algorithm editor and is widely popular due to the ease with plug-ins which can be used in the software; some plug-ins being Karamba 3D, Octopus and Galapagos, see Figure 3.3 (Davidson, 2018). Unlike other programming languages like Python or C++, Grasshopper is a visual programming language. This implies that no scripting is needed, even though possible; instead components and outputs are created on a canvas and connected together with inputs, see Figure 3.4a.

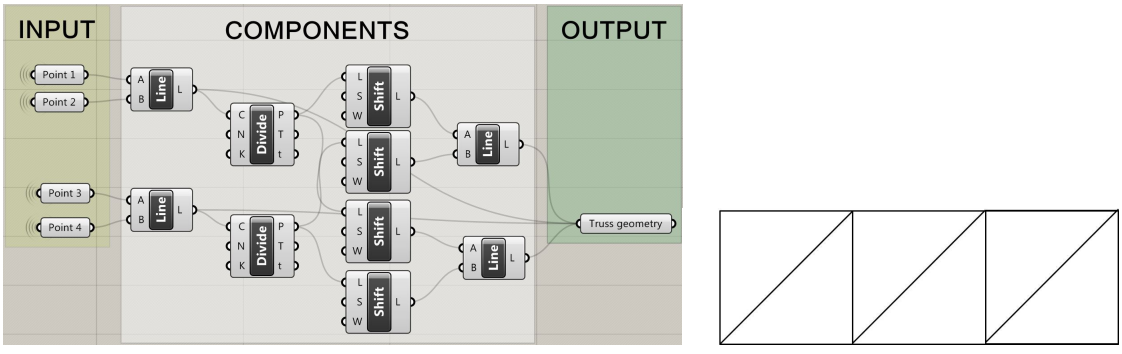

(a) (b)

Figure 3.4: (a) Example of how a truss structure can be created in Grasshopper. (b) Truss geometry output, visualized in Rhino.

As can be seen in Figure 3.4a the inputs to the left, which are changeable - in this case starting points for the truss - are connected via components, to achieve the wanted output in the end. The middle part in white represents all the components that are used to create the geometry of the truss. To the

right, in green, there is a geometry component containing the final truss geometry. The generated truss geometry can be seen in Figure 3.4b. Grasshopper version August 27 2014 build 0.9.0076 has been used in this thesis.

3.2.3 Karamba 3D

Karamba 3D is a structural analysis plug-in to Grasshopper which makes it possible to combine the parametric design environment of Grasshopper with structural analysis (Preisinger & Bollinger-Grohmann-Schneider, 2018). Karamba 3D takes the geometry created in Grasshopper and translates it into beams, shells, joints and other cross sections. Like in any structural analysis, supports as well as loads can be specified. All the parts can thereafter be assembled and analyzed with first or second-order theory. Karamba 3D can handle phenomenons like buckling and natural frequency. It contains also a result viewer where displacements and reaction forces can be displayed. In this thesis Karamba 3D version 1.3.0 WIP (180304) is used.

Some known limitations with Karamba 3D are pointed out in the Karamba 3D manual and listed below (Preisinger, 2016):

- Karamba 3D does not take global buckling into consideration.
- k_z and k_y are set to 1 for lateral torsional buckling
- The interaction factors, used in EC3 to calculate interaction between bending moment and normal force, C_{my}, C_{mz} and C_{mLT}, are restricted to values between 0.9 and 1.
- It is not possible to view global forces, like the bending moment across the whole structure. Instead Karamba 3D displays the internal forces.

3.2.4 Galapagos and Octopus

Galapagos is also a plug-in to Grasshopper that can optimize one parameter using single-objective EA. Since Galapagos comes together with Grasshopper it uses the same version as Grasshopper. In Galapagos, see Figure 3.5a, the user can first specify a genome which is the parameters that can be changed to optimize the structure. Secondly, the fitness can be chosen, for instance minimizing the vertical displacement. Galapagos then uses GA explained in Section 3.1.2 to generate a population and trying to optimize the fitness function.

In Galapagos there are some settings that can be changed to specify the speed or accuracy of the optimization, see Figure 3.5b. One of these settings are the size of the population, a large population means larger possibility to find local maximum and minimum but it increases the computation time. Another setting is the initial boost which is a factor that sets the population of the first iteration to a larger value to cover more of the design space. Drawbacks with a large initial boost is increased computation time. However, it reduces the chance of Galapagos being stuck in local maximum or minimum. Finally, the number of max stagnant means after how many iterations Galapagos stops if it does not find a better fitness value.

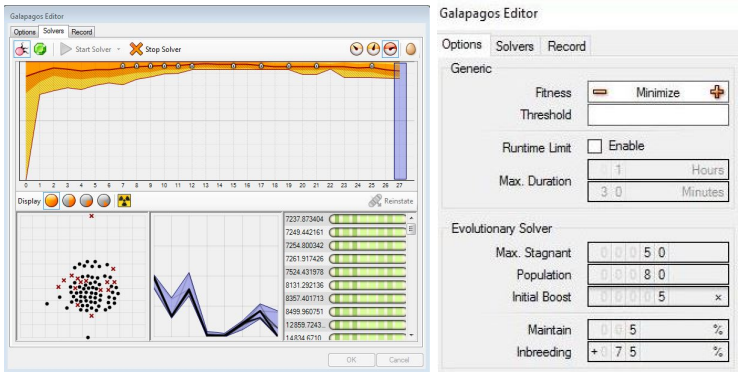

(a) (b)

Figure 3.5: (a) Galapagos solver (b) Settings in the Galapagos editor.

Octopus is another optimization software, that has two different optimization algorithms, SPEA-2 and HypeE both explained in Section 3.1.2. Since both SPEA-2 and HypE are MOEA:s, they have the possibility to optimize several fitness functions at the same time. Thus, Octopus allows the user to find the best trade off between several goals. Worth mentioning is that since Octopus uses a MOA, there will not be a single optimal solution but many solutions that are all optimal. Thus, it is up to the designer to chose which of these solutions that should be chosen. Since Octopus is a plug-in to Grasshopper the optimization can be used in combination with the structural analysis in Karamba 3D. For the scope of this report SPEA-2 is used for the multi-objective optimization in Octopus. HypE is disregarded since it is highly demanding regarding computational power. The version of Octopus used in this thesis is version 0.3.6.

Octopus has several settings that can be adjusted to change the behaviour of the optimization algorithm, see Figure 3.6. As for Galapagos, the first generation in Octopus starts with a larger population, in this case twice the preset population. The elitism setting means how much of the non-dominated solutions are stored into the secondary population. Mutation probability controls how likely it is that an individual mutates. The cross-over rate determines how much of the genes from the parent solutions is combined. A cross-over rate of 0.5 means half of the genes come from either parent. Finally, the size of the population can be chosen.

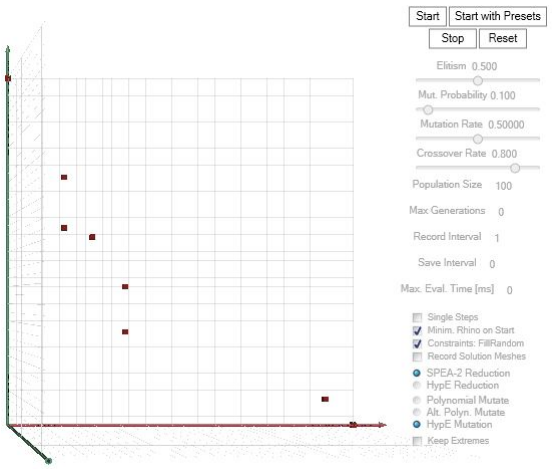

Figure 3.6: Octopus solver with solutions marked as cubes and the settings listed to the right.

4 Development and verification of the model in Karamba 3D

In this chapter a steel truss bridge over Genevadsån, an accomplished case from Ramböll, is presented and the development of a parametric model with the same conditions as the case, created in Rhino, Grasshopper and Karamba 3D, is described. In a next step the developed model is compared with the FEM-model from the case study with regard to sectional forces, natural frequency, maximum displacement of the bridge and utilization ratio of specified members of the bridge. Subsequently, two additional geometries are implemented and all the verification results are discussed.

4.1 Description of the case which the model is to be verified with

The considered case is a steel truss footbridge built over the stream Genevadsån, see Figure 4.1, which is located just south of Halmstad along side the highway E6 and represents a part of the planned cycle path between Gothenburg and Helsingborg - the so called Kattegattsleden (Alexandersson, 2014). The truss bridge was built in a factory and placed on site 14th of February 2018.

Figure 4.1: Reference project over the stream Genevadsån, picture from Ramböll (2018).

The bridge is a one span Warren truss bridge in steel and has a span length of 20 m, a width of 2.7 m and a height of 1.4 m. Hot-rolled hollow profiles (VKR) are used for the structural elements, except for the cross beams, for which IPE profiles are used. The bridge deck is a 10 mm thick steel plate and the steel quality for all elements is S355. The end cross beams are constructed to withstand a replacement of the bearings used for the supports. Further details are shown in Appendix B.

The reference bridge has been modeled in FEM-Design by Ramböll, see Figure 4.2, and to some extent simplified and adjusted to the focus of this thesis. FEM-Design is an advanced Finite element modeling (FEM) tool that allows the user to do detailed structural analysis and design (StruSoft, 2018) and is based on Eurocode with the accompanying national adjustments. All structural elements are modeled as steel beams except the bridge deck which is modeled as a shell structure. In the adjusted FEM-Design model all the members are fixed and the support conditions of the bridge are simply supported, see Figure 4.2, where the directions locked are shown as arrows. In this model the self-weight and crowd load are included as well as a line load from the railings of 0.5 kN/m along each bottom chord. This model is used to retrieve sectional forces, maximum displacements, natural frequencies and the utilization ratios, which are then compared with the model developed in Karamba 3D, described in the next section.

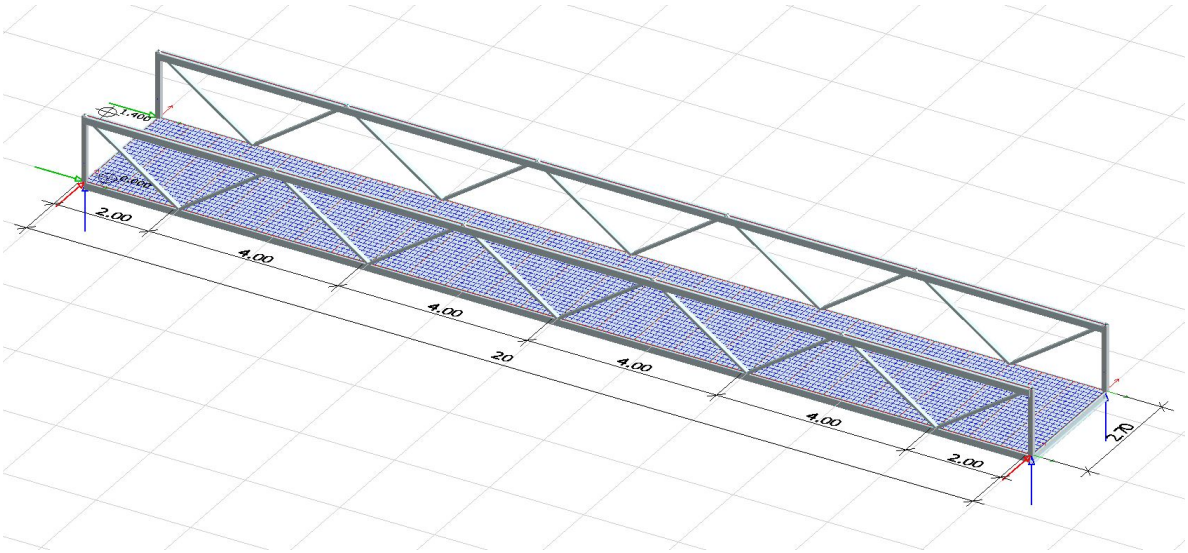

Figure 4.2: The reference bridge modeled in FEM-Design. The distances are shown in meters.

4.2 Development of the Warren sub model in Karamba 3D

In this section the geometry and the chosen structural properties of the Warren steel truss sub model in Karamba 3D are described more in detail. The loads and load combinations are also presented concluding in the assembly of all parts into the final model.

4.2.1 Development of the geometry in Grasshopper

The first step when creating a parametric model is defining the geometry of the studied bridge. From the presented bridges in Figure 2.3, it was decided to go further with the Warren truss bridge as it is a common footbridge type and since the reference bridge presented in Section 4.1 is a Warren truss bridge. The geometry of the bridge is created in Grasshopper using components as explained in Section 3.2.2. Starting with a single point in the origin (0/0/0) the geometry is created with components, duplicating and moving points into a final geometry, seen in Figure 4.3.

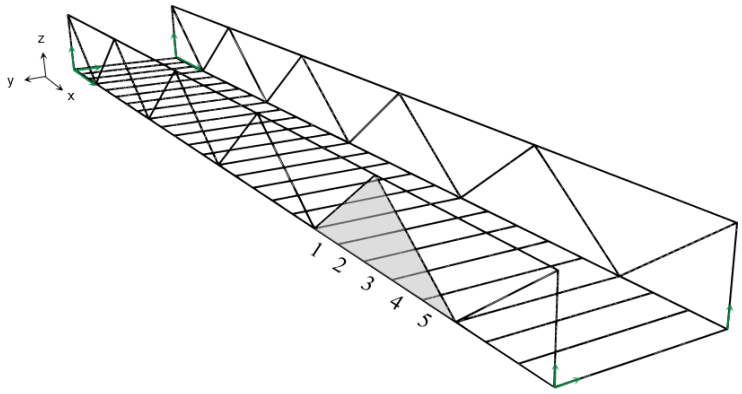

Figure 4.3: The final geometry of the Warren truss footbridge in Grasshopper. The support conditions are shown as arrows (locked direction) and the number of n_{cb}, within one diagonal triangle, are shown as numbers 1 to 5.

To adjust the appearance of the bridge, the designer can define the input parameters as the length, width and height of the bridge. Additionally the number of diagonal triangles ($n_{\triangle}$) and number of spacings between the cross beams (n_{cb}) within a diagonal triangle can be defined by the designer. It is arranged that the designer first chooses the $n_{\triangle}$, which are defined as 5 in the case of Figure 4.3. Afterwards n_{cb} can be set, which is also 5 in Figure 4.3. The same n_{cb} is then set at all the other truss triangles. At the start and end diagonal triangle, n_{cb} is half of the amount as for the ones in the mid sections. Should n_{cb} be an uneven number, the number is rounded up to the next number, i.e. to three in the case of Figure 4.3.

The geometry is divided into six main components of the bridge: The four longitudinal chords, the diagonals, the cross beams, the end cross beams, the vertical end posts and the bridge deck. The complete geometry is used as an input to Karamba 3D, where the structural analysis is executed.

4.2.2 Structural analysis in Karamba 3D

Even though the bridge geometry is created in Grasshopper, the finished geometry still needs to be translated into structural components and be given material properties. In Karamba 3D all the lines are translated into beams, which includes the longitudinal chords, the diagonals, the cross beams and the vertical end posts, which can be seen in Figure 4.4. The bridge deck, which is simulated as a mesh between the four corner points is translated into a shell.

Karamba 3D offers the user a list of cross-sections to apply to the geometry. There is also a possibility to add additional cross-sections, which is done in this case. VKR and circular hollow sections (KCKR) are added into Karamba 3D by specifying cross-sectional parameters into an excel-sheet where all cross-sections used in Karamba 3D are stored. The cross-sections used in this thesis for the beam elements are IPE, VKR and KCKR, which are all adjusted and based on the input values from (TIBNOR, 2011), which can be found in Appendix C. Worth mentioning is that the effective shear areas in y- and z-direction respectively for the IPE profiles are considered so that A_y only includes the area of the flange and A_z only includes the area of the web. The shear area for the VKR profiles are calculated according to EN 1993-1-1 chapter 6.2.6. VKR and IPE cross-sections are included in the model since they are used in the reference project. The circular cross-sections represent an addition to broaden the range of cross-sections. The final geometry with applied cross-sections is shown in Figure 4.4.

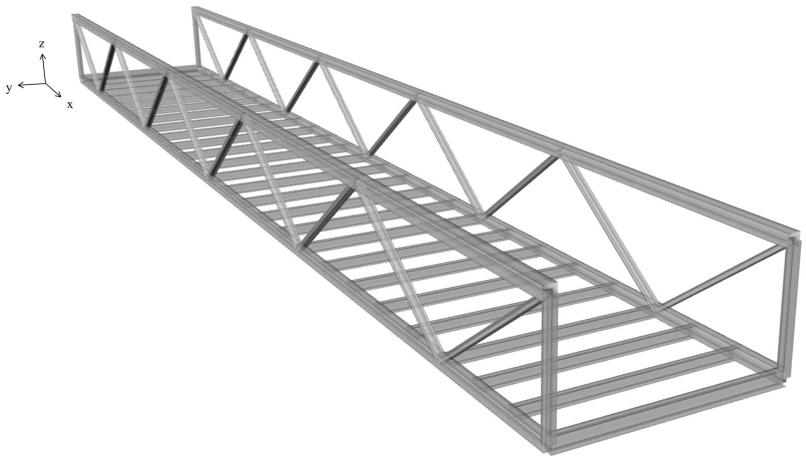

Figure 4.4: Final appearance of the Warren sub model in Karamba 3D with the the applied beam and shell elements.

The material and material class for the elements is specified to steel S355 and the Shear and Young's modulus used are 81 GPa and 210 GPa respectively. The density of the steel is set to 7 850 kg/m^3 and the gravitational constant to 9.82 m/s^2. Four supports are introduced in accordance to the case study, which are locked in the directions of the arrows, seen in Figure 4.3.

4.2.3 Definition of loads and load combinations

In case of footbridges there are a several loads that need to be considered, which are - according to Eurocode SS-EN 1991-2 table A2.2 - described in Table 4.1. The loads considered in this thesis are the self-weight of the construction and the crowd load. The uniformly distributed load is considered as a crowd load of 5 kN/m^2 and is a recommended value according to SS-EN 1991-2. The vehicle load representing a service vehicle is not included in this thesis, the reason being that it is not always considered, which is the case for the case over Genevadsån. Additionally, the wind and temperature load are not studied as the thesis is focusing on the global preliminary analysis. According to Eurocode, snow loads need not to be combined with load groups gr1 and gr2 and are therefore neglected.

Table 4.1: An overview of the included loads in this thesis.

Loads	Description		Symbol	Considered in this thesis
Permanent load	Self-weight of construction		Q_c	Yes
Variable load	Traffic load	Load group 1	gr1	Yes
		Concentrated load	Q_{fwk}	No
		Load group 2	gr2	No
	Snow load		$Q_{snk,k}$	No
	Wind load		$F_{W,k}$	No
	Temperature load		T_k	No

In Karamba 3D the self-weight of the structure can be retrieved automatically as the chosen element material and geometry is defined. However, the crowd load is simulated as line loads on each cross beam, which should then carry the load to the bottom chords and finally to the supports. Each cross beam is defined to take the load of the area with half the distance to the next cross beam on each side, times the width of the bridge.

The load combinations considered are ULS 6.10a, ULS 6.10b and SLS 6.15a-b (frequent) and the bridge is considered to be in safety class 3. The recommended values for the ψ-factors and the γ-values for the permanent and variable loads are shown in Table 4.2.

Table 4.2: Relevant factors for the permanent and variable loads.

Permanent loads	ψ-factors	
	Max	Min
Self-weight of construction, characteristic nominal value	1	1

Variable load	Comb ψ_0	Freq ψ_1	Quasi ψ_2	γ_Q
Load gr1: Uniformly distributed load (q_{fk}) + horizontal forces (Q_{flk})*	0.4	0.4	0	1.5

*neglected in this thesis

The final factors for the permanent and the variable loads for each load combination are shown in Table 4.3. Primary loads are the leading variable actions, i.e. the load is the main load. The secondary loads are accompanying variable actions, meaning that another load is the main load.

Table 4.3: Factors for permanent and variable loads in the three load combinations considered.

Permanent loads	6.10a ULS		6.10b ULS		6.10ab SLS	
	Max	Min	Max	Min	Max	Min
γ_G - factors	1.35	1	1.2	1	1	1

Variable loads	Primary	Secondary	Primary	Secondary	Primary	Secondary
	$\gamma_Q \bullet \psi_0$	$\gamma_Q \bullet \psi_0$	ψ_0	$\gamma_Q \bullet \psi_0$	ψ_1	ψ_2
Load gr1: Uniformly distributed load (q_{fk}) + horizontal forces (Q_{flk})*	0.6	0.6	1.5	0.6	0.4	0

*neglected in this thesis

The load combinations used in Karamba 3D are implemented in Grasshopper with the factors given in Table 4.3. The load combinations shown in Table 4.4 are all possible combinations for the loads used. The worst load combination is $6.10b_1$, which is the one used for all the verification results in the next section.

Table 4.4: All load combinations with the factors for the self-weight and crowd load respectively, which are used in the created model in Karamba 3D.

Load combination	Type	Name	Self-weight	Crowd load
6.10a	ULS	$6.10a_1$	1.35	0.6
		$6.10a_2$	1	0.6
6.10b	ULS	$6.10b_1$	1.2	1.5
		$6.10b_2$	1.2	0.6
		$6.10b_3$	1	1.5
		$6.10b_4$	1	0.6
6.10a-b	SLS	$6.10ab_1$	1	0.4
		$6.10ab_2$	1	0

4.3 Verification of the Warren sub model in Karamba 3D with the case study in FEM-Design

To see if the bridge developed in Karamba 3D is working properly it needs to be verified. First, the similarity of the input data of the developed model in Karamba 3D and the model in FEM-Design of the case study, see Section 4.1, is stated, which can be seen in Table 4.5, and is in accordance to each other.

Table 4.5: Input data of the developed Warren sub model, which is in accordance to the input data of the FEM-Design model of the case study.

Element	Cross-section	Dimensions [mm]	Steel quality	Quantity
Top chord	VKR	150x100x6.3	S355J2H	2
Bottom chord	VKR	150x100x6.3	S355J2H	2
Diagonals	VKR	100x60x5	S355J2H	20
Vertical end post	VKR	100x100x5	S355J2H	4
Cross beam	IPE	140	S355J2	25
End cross beam	IPE	180	S355J2	2
Bridge deck	Plate (LxWxH)	20 100 x 2 500 x 10	S355J2	1

Further, the structural analysis is of interest and to be compared for the two software. Using the components in Karamba 3D, a first order, plastic analysis is made to calculate the reaction and sectional forces, the maximum displacement and the utilization ratios of the bridge, which are compared with the ones from the FEM-model from the case study. Also the natural frequency is verified with the results from FEM-Design and hand calculations. As a first attempt to verify the results of the two models, the reaction forces of a simple equilibrium of the bridge is investigated, which can be seen in Table 4.6. The difference between the results is rather small and sets the basis for further verification of the results.

Table 4.6: Comparison of the reaction forces of the two models in a first attempt of verification.

	Reaction forces [kN]		
Load applied	Karamba 3D	FEM - Design	Difference
Self-weight	24.8	24.4	2 %
Crowd load	62.5	62.5	0 %

In a next step the normal force N, the moment M_y and the shear force V_z of the two models are compared. This is executed with the preconditions that the railing of 0.5 kN/m is included in the permanent load and load case $6.10b_1$, see Table 4.4, is used. In this case, $6.10b_1$ is chosen as it is the worst case in ULS when only considering the crowd load. The choice of load combination is of no importance in the verification, as long as it is the same in the two software. Due to symmetry, only one half of the bridge is investigated and its results presented. First, the normal force diagram of the bottom chord is displayed in Figure 4.5 and the associated numbers shown in Table 4.7.

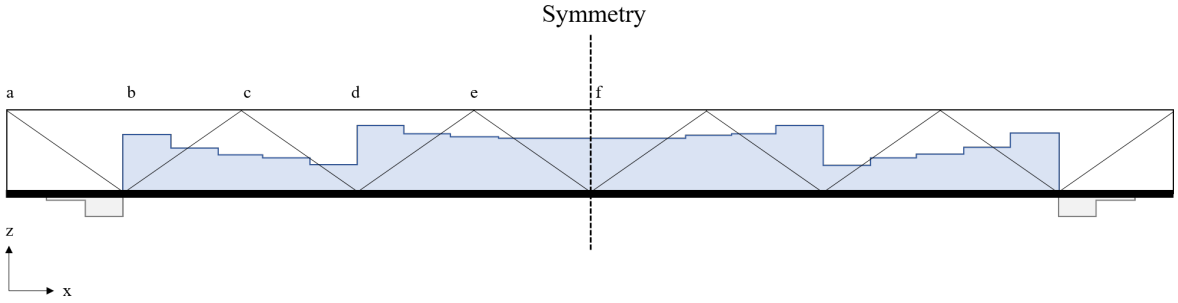

Figure 4.5: Normal force diagram of the bottom chord from Karamba 3D.

Table 4.7: Comparison of the absolute values of the normal force from position a to f of the bottom chord from Karamba 3D with FEM-Design.

		Normal force N [kN] (absolute values)		
Member	Position	Karamba 3D	FEM-Design	Difference
Bottom chord	a	1.0	1.8	-42 %
	b (left)	31.1	91.3	-66 %
	b (right)	77.6	141.5	-45 %
	d (left)	32.0	0.5	6 709 %
	d (right)	86.7	122.7	-29 %
	f	71.6	73.9	-3 %

As can be seen in Table 4.7, the normal forces in the bottom chord do not seem to match, which indicates a difference between the two models. The difference in results originates from the behaviour of the bridge deck. In both software, the bridge deck is included with the same supporting conditions, namely fixed. Reasoning that the design of the bridge deck is of no interest when optimizing, focusing on the structure and behaviour of the truss footbridge, it is decided to weaken the bridge deck. When dividing the Young's and Shear modulus with a weakening factor, the stiffness of the bridge deck is weakened, but the mass of it remains. In Figure 4.6 a convergence study is presented, showing the influence of the stiffness of the bridge deck on the normal force at position f in the bottom chord by increasing the weakening factor.

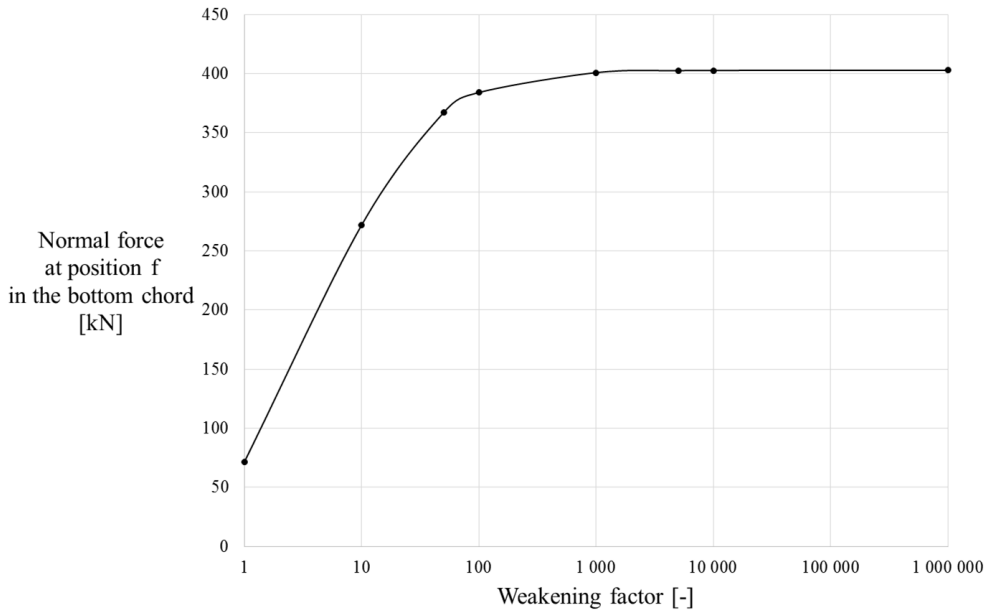

Figure 4.6: Convergence study of the normal force in the bottom chord at position f for different weakening factors in the bridge deck.

As can be seen in Figure 4.6, the normal force at position f of the bottom chord seems to start converging with a weakening factor 1 000. Due to this fact, being somewhat on the safe side, a weakening factor of 10 000 is henceforth chosen for all results, if not mentioned otherwise. A more detailed investigation of all normal forces with different weakening factors is found in Appendix D. The new results of the normal force in the bottom chord with a weakening factor of 10 000 is shown in Figure 4.7 and Table 4.8. As can be seen, the results now cohere well to each other, having the largest difference of 4 %.

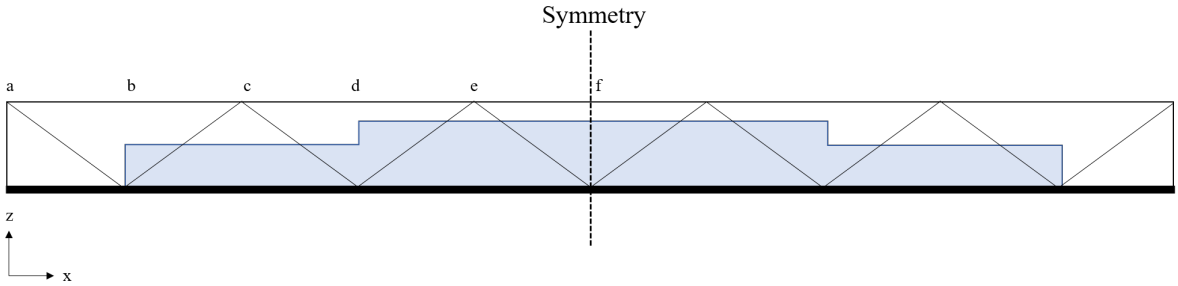

Figure 4.7: Normal force diagram of the bottom chord from Karamba 3D with a weakening factor 10 000.

Table 4.8: Comparison of the absolute values of the normal force at position a to f in the bottom chord from Karamba 3D with FEM-Design with a weakening factor 10 000(*).

		Normal force N [kN] (absolute values)		
Member	Position	Karamba 3D, 10 000*	FEM - Design, 10 000*	Difference
Bottom chord	a	3.2	3.0	4 %
	c	266.3	270.1	-1 %
	f	403.0	411.2	-2 %

Secondly, the moment distribution in the bottom chord is analyzed and presented in Figure 4.8 and the results, compared to the ones in FEM-Design, are shown in Table 4.9. The results are quite in accordance, having the largest deviation of 6 % at position a.

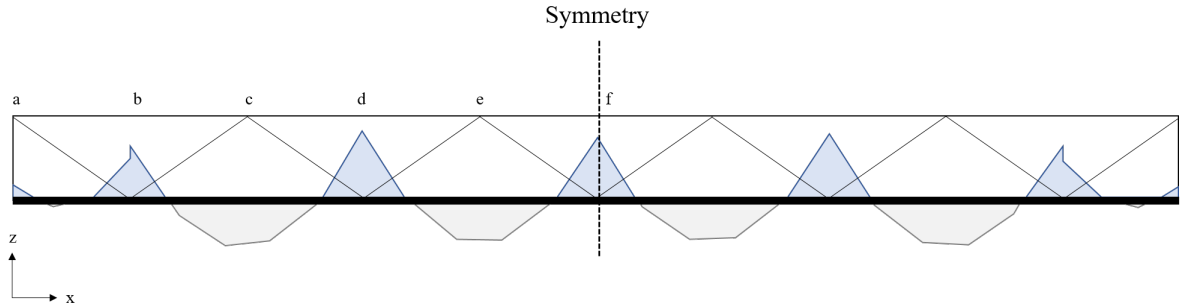

Figure 4.8: Moment diagram of the bottom chord from Karamba 3D.

Table 4.9: Comparison of the absolute values of the moment at position a to f in the bottom chord from Karamba 3D with FEM-Design.

		Moment My [kNm] (absolute values)		
Member	Position	Karamba 3D	FEM - Design	Difference
Bottom chord	a	2.5	2.3	6 %
	b	10.3	10.4	-1 %
	c	10.2	10.5	-3 %
	d	14.0	14.4	-3 %
	e	9.1	9.3	-2 %
	f	12.2	12.6	-3 %

Thirdly, the shear forces of the bottom chord are investigated, shown in Figure 4.9 and the results and comparison with FEM-Design displayed in Table 4.10. As can be seen, these results also cohere well to each other, having the largest deviation of 5 %.

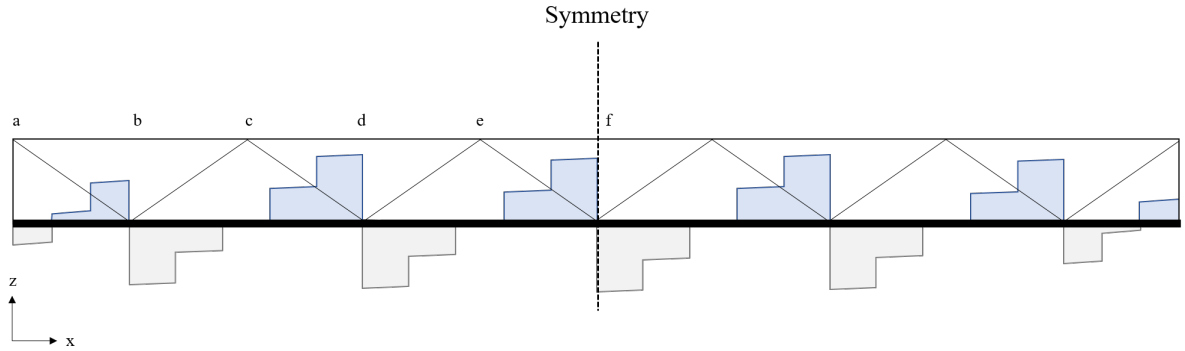

Figure 4.9: Shear force diagram of the bottom chord from Karamba 3D.

Table 4.10: Comparison of the absolute values of the shear forces at position a to f in the bottom chord from Karamba 3D with FEM-Design.

		Shear force Vz [kN] (absolute values)		
Member	Position	Karamba 3D	FEM - Design	Difference
Bottom chord	a	6.0	5.7	4 %
	b (left)	12.3	11.7	5 %
	b (right)	17.7	18.3	-3 %
	d (left)	19.6	20.3	-4 %
	d (right)	19.0	19.7	-4 %
	f	18.2	18.9	-3 %

In Table 4.11, the maximum displacement downwards in the middle of the Warren sub model (position f see Figure 4.9) can be seen. Worth mentioning is that still load case 6.10b_1 (ULS) is applied when retrieving the results for the comparison. The displacements between the two models cohere well to each other. Further results of the sectional forces of all elements and maximum displacements with an unweakened bridge deck (weakening factor 1) are shown in Appendix D.

Table 4.11: Comparison of the absolute values of the maximum displacement at position f in the bottom chord from Karamba 3D with FEM-Design.

		Max displacement [mm] (absolute values)		
Member	Position	Karamba 3D	FEM - Design	Difference
All	f	52.2	53.2	-2 %

Considering the utilization ratio of the bridge members, a small study is executed to verify if the utilization component in Karamba 3D works as intended. In an attempt to verify the utilization ratio, the results from Karamba 3D are compared with the ones from FEM-Design from the case study. The utilization ratios are calculated according to SS-EN 1993-1-1, sections 6.2-6.3. In both Karamba 3D and FEM-Design following controls are considered, see Table 4.12.

Table 4.12: Considered controls in Karamba 3D and FEM-Design.

Control	Chapter in EN 1993-1-1
Normal stress	6.2.1
Normal capacity	6.2
Flexural buckling	6.3.1
Torsional-flexural buckling	6.3.1
Lateral torsional buckling	6.3.2.2
Interaction between normal force and bending, 1st and 2nd order	6.3.3
Shear resistance	6.2.6, 6.2.8
Torsional resistance	6.2.7

When looking at all elements, the worst maximum utilization ratio for each element is detected in both Karamba 3D and FEM-Design and presented in Table 4.13.

Table 4.13: Comparison of the largest utilization ratios for each element, based on load case $6.10b_1$, from Karamba 3D with FEM-Design.

	Maximum utilization ratio		
Element	Karamba 3D	FEM-Design	Difference
Bottom chord	62 %	67 %	-6 %
Top chord	51 %	53 %	-2 %
Diagonals	65 %	60 %	5 %
Vertical end posts	31 %	30 %	1 %
Cross beams	18 %	47 %	-29 %
End cross beams	9 %	15 %	-7 %

Looking at Table 4.13, the largest difference of the maximum utilization ratios between the two models is detected to be for the cross beams, which is why they are investigated further. In the case of load combination $6.10b_1$, see Table 4.4, the maximum utilization ratios of the normal, moment and shear resistances of the mid cross beam at position f are compared between the two models, which can be seen in Table 4.14.

Table 4.14: Maximum utilization ratios of each sectional force and the difference between them. The load case applied is $6.10b_1$ and the element considered is the mid cross beam at position f.

	Maximum utilization		
Member	Karamba 3D	FEM-Design	Difference
Normal force N	0 %	0 %	0 %
Moment My	18 %	47 %	-29 %
Moment Mz	1 %	0 %	1 %
Shear force Vy	0 %	0 %	0 %
Shear force Vz	7 %	5 %	2 %

Additionally, the details retrieved from the utilization component in Karamba 3D are compared with the corresponding ones from FEM-Design, which is shown in Table 4.15, still looking at the mid cross beam with load case $6.10b_1$. During this step, the buckling length of the cross beams, including the end cross beams, in x- and y-direction is detected to be 0.27 m in Karamba 3D. This is wrong and therefore changed to 2.7 m in both x- and y-direction, which is the same as in the FEM-Design model. The calculation procedure from FEM-Design of the cross beam at position f can also be found in Appendix D.2. In Table 4.15 the normal resistance (N_{Rd}), critical normal force capacity (N_{cr}) moment resistance (M_{yRd}), critical moment capacity (M_{cr}), shear resistance (V_{yRd}, V_{zRd}), the lateral torsional reduction factor χ_{LT} and all interaction values (k_{yy}, k_{zz}, k_{yz}, k_{zy}) of the cross beam, with adjusted buckling length, at position f from Karamba 3D and FEM-Design are presented.

Table 4.15: Results of the normal resistance (N_{Rd}), critical normal force capacity (N_{cr}), moment resistance (M_{yRd}), critical moment capacity (M_{cr}), shear resistance (V_{yRd}, V_{zRd}), the lateral torsional reduction factor (χ_{LT}) and all interaction values (k_{yy}, k_{zz}, k_{yz}, k_{zy}) of the cross beam at position f from Karamba 3D and FEM-Design after adjustment of the buckling lengths.

	Karamba 3D	FEM - Design	Difference
N_{Rd} [kN]	591.5	583.1	1 %
N_{cr} [kN]	127.9	127.7	0 %
M_{yRd} [kNm]	31.8	31.4	1 %
M_{cr} [kNm]	18.0	16.1	11 %
V_{yRd} [kN]	209.4	215.1	-3 %
V_{zRd} [kN]	123.3	156.6	-21 %
χ_{LT}	0.51	0.42	21 %
k_{yy}	1	1	0 %
k_{zz}	1.00	1.03	-3 %
k_{yz}	0.6	0.8	-27 %
k_{zy}	1.0	0.5	92 %

As can be seen in Table 4.15 there are still some differences, considering the critical moment capacity (M_{cr}), shear resistance (V_{zRd}), the lateral torsional reduction factor χ_{LT} and the interaction values k_{yz} and k_{zy}. Nevertheless, the maximum utilization values for the cross beams and the end cross beams result in somewhat better ratios after all, see Table 4.16. Also, the buckling length of the bottom chord was detected to be wrong and changed from 0.8 m to 4 m in z-direction, which also resulted in somewhat better results than before the adjustment, see Table 4.16.

Table 4.16: Comparison of maximum utilization ratios for the bottom chord, cross beams and end cross beams in Karamba and FEM-Design with adjusted buckling lengths.

	Maximum utilization ratio		
Element	Karamba 3D	FEM-Design	Difference
Bottom chord	64.0 %	67.0 %	-3 %
Cross beams	35.3 %	47.0 %	-12 %
End cross beams	14.9 %	15.0 %	-0 %

To be able to have a look at the natural frequency, the bridge deck needs to be stiff, i.e. the weakening factor needs to be 1 - only for the verification of the natural frequency. As can be seen in Table 4.17, the results from Karamba 3D are compared with the ones from FEM-Design and with hand calculations, which can be found in Appendix E. The results seem to cohere well to each other, especially the results from Karamba 3D compared to the hand calculations. The shapes of the first modes from Karamba 3D and FEM-Design are shown in Figure 4.10 and look the same.

Table 4.17: Natural frequency for mode 1 from Karamba 3D compared with the results from FEM-Design and hand calculations.

	Natural frequency mode 1 [Hz]			Natural frequency mode 1 [Hz]		
Element	Karamba 3D 1*	FEM-Design	Difference	Karamba 3D 1*	Hand calculations	Difference
All	6.7	7.0	-3 %	6.7	6.7	0 %

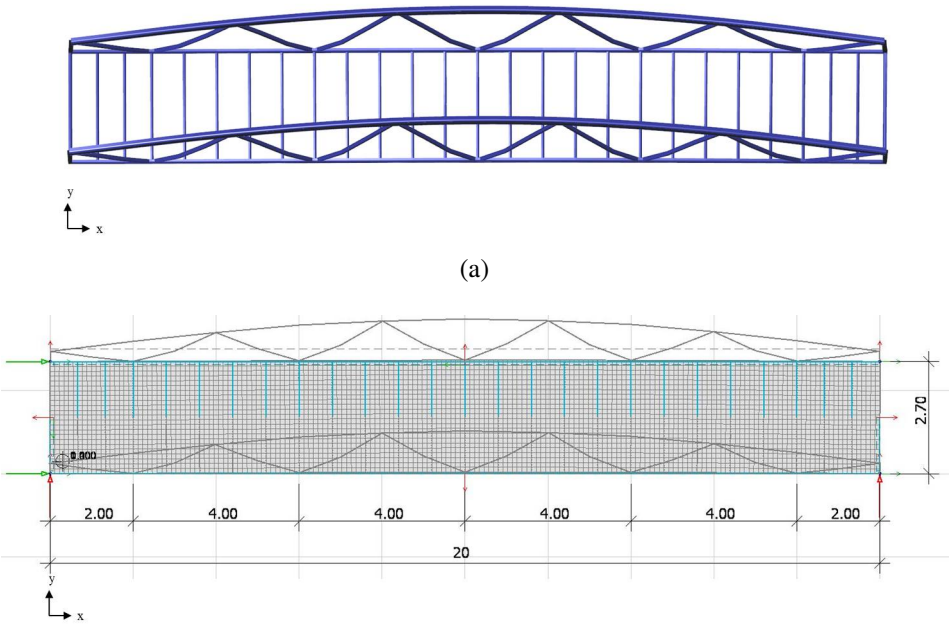

Figure 4.10: The natural frequency (mode 1) of the Warren sub model in Karamba (a) and FEM-Design (b).

4.4 Development and verification of the Pratt and Howe sub models

To give the designer a variety of truss bridge designs to chose from, two additional geometries are added to the script in Grasshopper. As the two most common trusses, the geometries of the Pratt and Howe truss, constituting two additional sub models in Karamba 3D, are implemented. The process of implementing these two extra geometries is similar to the one for the Warren truss explained in Section 4.2.1. At the beginning of the Grasshopper script there is an option to choose which of the three trusses to do the calculations on. Both the Pratt and Howe truss have been verified with a created FEM-Design model in the same way as for the Warren truss, see Section 4.2, having a weakening factor 10 000 for the bridge deck and using load case 6.10b_1. Additionally the same perquisites as for the case study are used, i.e. the length is 20 m, the width 2.7 m and the height 1.4 m. The cross-sections of the members are the same as in Table 4.5 and $n_{\triangle}$ is 5 and n_{cb} is 5. For the Pratt and Howe truss sub models $n_{\triangle}$ can only be an even number. This implies, that if an uneven number is set, it is rounded up to the next number.

Starting with the verification of the Pratt sub model, the sectional forces, the maximum displacement of the bridge and utilization ratio of the elements of the bridge in Karamba 3D are - accordingly to the verification of the Warren truss bridge - compared to the created FEM-Design Pratt model. In Figure 4.11 the shape of the Pratt truss is presented, followed by results for the reaction force of one support and the maximum displacement of the bridge from both Karamba 3D and FEM-Design, see Table 4.18. The difference of both results seem to coincide well to each other.

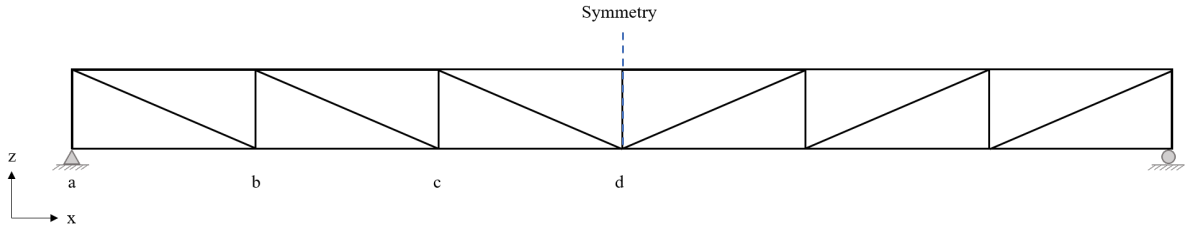

Figure 4.11: The Pratt truss bridge with position identifications.

Table 4.18: Reaction force of one support and the maximum displacement of the Pratt truss sub model.

Description	Load	Karamba 3D	FEM-Design	Difference
Reaction force (1 support) [kN]	Self-weight	20.4	20.7	-2 %
Max. displacement [mm]	Load case $6.10b_1$	57.9	57.9	0 %

In Table 4.19, the maximum utilization ratios for the different members of the bridge are presented for both Karamba 3D and FEM-Design. All the results of the sectional forces of the members can be found in Appendix F and are not shown in this chapter as the results are very satisfying. The results in Table 4.19 seem to correspond well to each other, having the largest difference of 6 % for the utilization ratio of the cross beams.

Table 4.19: Maximum utilization ratios for each member with the perquisites of the case study and load case $6.10b_1$ for the Pratt truss sub model.

	Maximum utilization ratio		
Member	Karamba 3D	FEM-Design	Difference
Bottom chord	52 %	54 %	-2 %
Top chord	47 %	48 %	-1 %
Diagonals (a-b)	52 %	53 %	-1 %
Vertical end posts (a)	52 %	53 %	-1 %
Cross beam (f)	31 %	37 %	-6 %
End cross beams	13 %	14 %	-1 %

In a next step, the Howe truss sub model in Karamba 3D is verified with the created FEM-Design Howe model. For this model all the results including the sectional forces of the different members are presented in Appendix G. The sectional forces proved also in this case to correspond well to each other. The Howe truss is shown in Figure 4.12 and the results of the reaction force in one support and the maximum displacement of the bridge is displayed in Table 4.20. The maximum displacement and reaction force from both software agree well to each other.

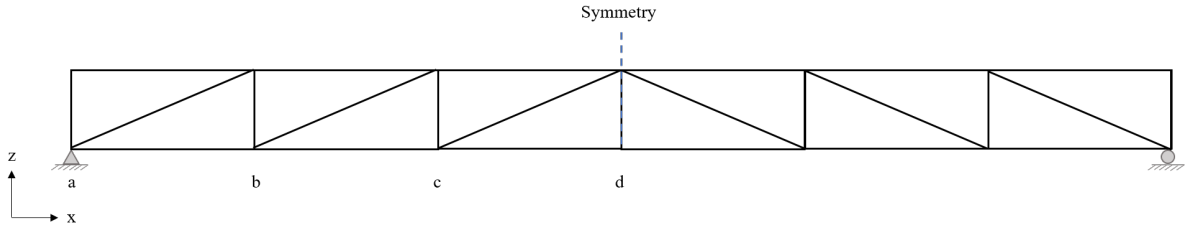

Figure 4.12: Position identifications of the truss elements for the Howe truss bridge.

Table 4.20: Reaction force of one support and the maximum displacement of the Howe truss sub model.

Description	Load	Karamba 3D	FEM-Design	Difference
Reaction force (1 support) [kN]	Self-weight	20.4	20.9	-2 %
Max. displacement [mm]	Load case $6.10b_1$	61.0	60.7	1 %

As for the Pratt truss sub model, the maximum utilization ratio of all elements for the Howe truss sub model is shown in Table 4.21. Also for this model, the differences between the results between the two software cohere well to each other, having the largest difference again for the cross beams. It needs to be added that the buckling length of the cross beams is adjusted to 2.7 m in both x- and z-direction for all results in this section, as was previously done for the Warren truss.

Table 4.21: Maximum utilization ratios for each member with the perquisites of the case study and load case $6.10b_1$ for the Howe truss sub model.

	Maximum utilization ratio		
Member	Karamba 3D	FEM-Design	Difference
Bottom chord	57 %	60 %	-3 %
Top chord	43 %	45 %	-2 %
Diagonals (a-b)	229 %	226 %	3 %
Vertical end posts (a)	36 %	37 %	-1 %
Cross beam (f)	31 %	37 %	-6 %
End cross beams	13 %	13 %	0 %

4.5 Discussion of the verification results for the Warren, Pratt and Howe truss sub models

The reaction forces from Karamba 3D and FEM-Design differ insignificantly, that is 2 % considering the Warren, Pratt and Howe truss sub models. The reason for the deviation is probably due to the small differences in the input data of the two software.

The normal forces in the bottom chord are the ones that are the most affected by the stiffness of the bridge deck. The influence of the stiffness of the bridge deck on the normal force distribution on the bottom chord of the Warren truss sub model can be seen by comparing Figures 4.5 and 4.7. The normal forces in the bottom chord, having a weakening factor 1, vary a lot between Karamba 3D and FEM-Design. However, results with a weakening factor 10 000, see Table 4.8, show a good correspondence to each other between Karamba 3D and FEM-Design for the Warren truss sub model.

Considering the normal force in the bottom chord for the Warren, Pratt and Howe truss sub models with a weakening factor 10 000, the results from Karamba 3D and FEM-Design coincide well with each other, having the largest difference of 4 % at position *a* for the Warren truss bridge sub model, which can be accepted as the values are rather small compared to the other results in Table 4.8.

The results of the bending moment *My* from Karamba 3D and FEM-Design at the positions *a* to *f* correspond well to each other, see Table 4.9, thus having a difference of 6 % in the Warren truss sub model at position *a* in the bottom chord. Yet again the results in the end span can be accepted since the values are low compared to the rest of the bending moments in the bottom chord.

The results of the shear forces *Vz* between Karamba 3D and FEM-Design are also in good accordance to each other, see Table 4.10. The largest difference between the two software considering the shear force of the bottom chord is 5 % at position *b (left)*. The difference of the results can be explained by small differences in effective shear area for Karamba 3D and FEM-Design, due to the facts mentioned in Section 4.2.2. Also more decimals of the input data of the cross-sections are implemented into FEM-Design. This can explain some of the differences of the shear force along the bottom chord.

Another explanation for the small deviations of all the sectional forces between the results in Karamba 3D and FEM-Design could be the difference in calculation points on a member. Karamba 3D defines an element to be between two points. Having points created on for instance the bottom chord, reassembling connection points for the cross beams with the bottom chord or the connection points for the diagonals with the bottom chord, many small elements represent the bottom chord as one member. For each element of a member only the results of the start and end points are displayed in Karamba 3D, which are then connected linearly to each other, which can be seen in for instance Figure 4.8 or Figure 4.9. This does not give accurate results in between the start and end points of an element, only an average. FEM-Design on the other side calculates the sectional forces in much more points, giving a more accurate picture of many more results of a member. Due to this fact, for instance the results of the bending moment from Karamba 3D at position *c* in the bottom chord, see Table 4.9, is actually not exactly at position c, but the largest value of the element at position *c*. Knowing this, the values from Karamba 3D are already smaller than the one from FEM-Design, which means that an exact calculation of the mean value at the exact position *c* would not help for the better for Karamba 3D.

Further, looking at the normal force in the bottom chord with a weakening factor 1, the average value of each small element at the given positions are compared to the peak points in FEM-Design, which seems quite unfair to compare with. The overall shape of the normal forces of the bottom chord can be found in Appendix D and are approximately the same in both Karamba 3D and FEM-Design, which indicates that the same conditions are applied for the bridge deck in both software. The results, as stated before, are differing though, due to the average values in Karamba 3D.

Looking at the displacement, the Warren truss sub model in Karamba 3D shows a larger maximum displacement compared to FEM-Design. All in all it only represents a difference of 2 % corresponding to 1 mm which is a very small value and insignificant. Considering the Pratt and Howe truss sub models, the maximum displacement is 0 % and 1 % respectively and also negligible. One explanation for the small deviations is that the self-weight differs about 2 % between Karamba 3D and FEM-Design, which makes it acceptable that the displacements differ about 2 % as well.

The maximum utilization ratio for different members, see Table 4.13, first showed large differences between Karamba 3D and FEM-Design, especially considering the cross beams. Investigating the cross beams further, the utilization of the moment My turned out to be the issue. The utilization of the moment My is dependent on among others the factor χ_{LT}, which in turn is dependent on critical moment capacity M_{cr} and the moment and interaction factors. The crucial cause why the results differ is the way how the interaction values and moment factors are calculated. In FEM-Design method 1 in Annex A in EN 1993-1-1 is used, while Karamba 3D uses method 2 in Annex B in EN 1993-1-1. Additionally the critical moment capacity relies on the critical normal capacity N_{cr} which is dependent on the buckling length of the cross beams. Having the buckling length of the cross beams between the start and end points of all elements, as mentioned before, the buckling length of the cross beams in Karamba 3D was too short. Adjusting the buckling length to 2.7 m in both x- and z-direction, the results in Table 4.16 showed somewhat better results. Still, the difference for the cross beams is 12 % and not to forget, there still is a difference of 5 % considering the maximum utilization ratio of the diagonals. The differences can at this state only be explained by the fundamental difference between Karamba 3D and FEM-Design when calculating the moment and interaction factors and is only stated and not to be considered further in this thesis, even though some of the results are not quite acceptable and on the unsafe side compared to the results in FEM-Design.

Regarding the natural frequency, the results show great accordance looking at the Warren sub model, both compared to the results in FEM-Design and the hand calculations with a difference of 3 % and 0 % respectively. Unfortunately, this thesis does not comprise a further investigation of the natural frequencies of the Pratt and Howe sub models and gives the opportunity to be developed further in the future. Due to the fact that the weakening factor needs to be changed to 1 to retrieve the results for the natural frequency, it also constitutes an issue when optimizing, as the factor needs to remain one number, either 1 or 10 000. As the majority of the results rely on a weakening factor of 10 000, this factor is used and the natural frequency is left behind, but can be checked separately, changing the weakening factor to 1.

5 Development of the optimization features

Multi-objective optimization is advanced and it can be difficult to confirm what solution is the most optimal one since the solution is a compromise of several solutions. To get a grip on what solutions are reasonable for a multi-objective optimization, some optimization runs are executed using single-objective optimization. This is why in the first phase of the optimization Galapagos is used, since it is a plug-in designed for single-objective optimization. Once the optimization process works for one fitness function several fitness functions can be introduced and then Octopus is used. This section starts with describing the constraints used when optimizing and how they are implemented into Karamba 3D and concludes in specific settings and features used when optimizing with Galapagos and Octopus.

5.1 Constraints when optimizing

To avoid getting unreasonable solutions from a optimization, constraints are introduced. The constraints, see Table 5.1, are the maximum allowable displacement of the whole bridge (SLS), the maximum utilization of the cross-sections (ULS) and a global lateral torsional buckling criteria for the top chord (ULS), see Table 5.1.

Table 5.1: These are the used constraints when optimizing the Karamba 3D models.

Maximum displacement (SLS)	L/400
Maximum utilization ratio for each the cross-section (ULS)	85 %
Maximum normal force in top chord (ULS)	$N_{ED}<N_{b,RD}$

The displacement criterion is limited to L/400 according to Krav Brobyggande TDOK 2016:0204 section B.3.4.2.2. According to Krav TDOK 2016:0204 section B.3.4.2.1 only the frequent values should be used when calculating the maximum displacement, implying that the self-weight is ignored for this constraint. Only the frequent load, being the crowd load, is considered and multiplied with the ψ_1-factor of 0.4, see Table 4.3. This also presumes that the bridge is precambered with the height being the displacement that the self-weight alone would cause.

The utilization constraint is set to 85 % of the cross-section capacity, not 100 %, having a 15 % safety buffer considering the somewhat unsatisfying results in Section 4.2.2 for the utilization ratio. Since the biggest difference between the Karamba 3D model and the FEM-Design model in utilization ratio is around 12 % the safety buffer of 15 % seems warranted.

As mentioned in Section 3.2.3 Karamba 3D only considers local buckling of elements. For through truss bridges without top lateral bracing, global buckling of the top chord could be a limiting factor. To include the phenomenon of lateral torsional buckling of the top chord into the model, which should be considered according to the statement SS-EN 1993-2 section 6.3.4.2 equation (2), calculations are executed according to (Wahlström, 1971), which are based on empirical results.

The calculations are included in the script in Grasshopper according to Appendix H, where the top chord is modeled as a column loaded in axial compression with the maximum normal force N_{Ed} of the top chord, supported on a spring bed. The spring stiffness of the springs is calculated by applying

a unit load of 1 000 kN onto the truss system, leaving the top chord out, see Figure 5.1, which shows the Warren sub model. The supports can also be seen in Figure 5.1, where the arrows reassemble the directions which are locked. All joints are defined as rigid, except at the joint where the load is applied. At this location the rotational condition is defined as free. The verification of the global LT-buckling of the top chord is only executed on the Warren sub model. The corresponding figures of Figure 5.1 of the Pratt and Howe sub models can be found in Appendix H.

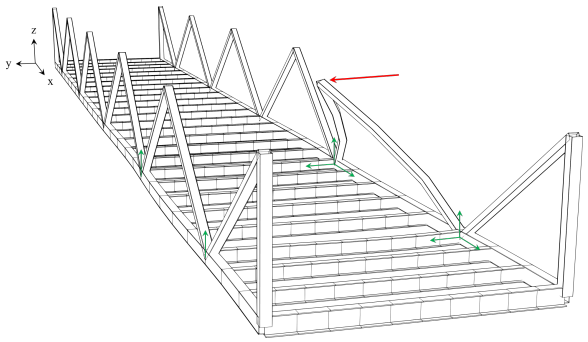

Figure 5.1: The Warren sub model without the top chords. A unit load of 1 000 kN is applied to calculated the displacement in y-direction.

To verify the displacement (δ) received after applying the unit load, the same is executed in FEM-Design. The Warren sub models in Karamba 3D and FEM-Design have the same perquisites as in the case study, see Section 4.2. The displacement in y-direction for the Warren truss bridge from Karamba 3D and FEM-Design are presented in Table 5.2. The displacement for the Warren truss in Karamba 3D seems to correspond well to the results from FEM-Design. The maximum reduced normal capacity (N_{bRd}), which is based on δ, is also presented in Table 5.2. The maximum normal force in the top chord, N_{ED}, must not exceed N_{bRd}.

Table 5.2: The displacement in y-direction after applying a unit load of 1 000 kN and the maximum normal capacity N_{bRd} of the top chord.

	Karamba 3D	FEM-Design	Difference
δ in y-direction [m]	7.1	7.0	0 %
N_{bRd} [kN]	507.0	507.5	0 %

Table 5.2 shows that the results from the Warren sub model in Karamba 3D corresponds well to the results from FEM-Design. The constraint considering the global lateral torsional buckling is implemented in Karamba 3D as an additional model, which is continuously updated each time a parameter changes during optimization.

5.2 Settings for the optimization features

The model can be optimized according to different fitness functions. In this thesis the mass and transparency are chosen to be fitness functions. The mass of all elements can easily be retrieved from an implemented component in Karamba 3D. The side view area on the other hand is calculated, using the dimensions of the cross-sectional profiles. The elements affecting the side view area are the top chord, the bottom chord, the diagonals, the verticals and the vertical end posts.

The two fitness functions are depending on other parameters such as the choice of cross-section and the topology of the bridge. For the topology two parameters are changeable, $n_{\triangle}$ as well as n_{cb}. The minimum of $n_{\triangle}$ is set to 1 and the maximum to 20, seeTable 5.3. The value of n_{cb} can vary between 1 and 10 within a diagonal triangle. Considering the cross-sections the sections are restricted to VKR-, KCKR- and IPE-profiles, as mentioned in Section 4.2.2, which gives the availability to chose between 163 different cross-sections. All variable parameters are shown in Table 5.3; the span length, width and height of the footbridges are kept constant during one optimization. Since the bridge deck has been weakened with a factor 10 000, the cross-section of the bridge deck is not of interest and therefore not optimized.

Table 5.3: Variable parameters when optimizing. The span length, width and height of the bridge are kept constant.

Variable parameters	Min	Max
$n_{\triangle}$	0	20
n_{cb}	0	10
Cross sections	-	-

When optimizing, Galapagos and Octopus aims to maximize the fitness of the design space. In the case of this thesis, to maximize the fitness, the mass should be minimized, whereas the transparency should be maximized, i.e. the side view area is minimized. Even though there may be solutions that violate the constraints, theses solutions can give high fitness. For instance if the goal is to minimize the weight of the construction, Galapagos or Octopus may choose a solution where there are no structural elements, making the weight of the structure zero, which is a unreasonable solution but the one with highest fitness. To avoid this problem, the changeable parameters are restricted to solutions which generate a complete geometry. Furthermore, if Galapagos or Octopus chooses a solution which violates at least one constraint, the solution is punished. To do this, a penalty function, as mentioned in Section 3.1.2, is introduced, see Figure 5.2a. In short meaning that if violating any of the shown constraints, the fitness function of the solution is redirected and multiplied with a high value, giving the solution low fitness, to facilitate the elimination of the bad solutions.

Since the purpose of the optimization is to get an optimal design of the main load bearing structure, the truss sub models are optimized with the worst load combination only including the permanent load and the evenly distributed crowd load, which is load case $6.10b_1$, see Table 4.4. The constraint for the maximum displacement relies on load combination $6.10ab_1$ (SLS), see Table 4.4, not including the self-weight, as explained in Section 5.1.

To summarize the procedure of optimization, it can be stated that it consists of many loops, which is shown in Figure 5.2b. The loops start with the variable parameters which are tested, which form a geometry and finally a structural model in Karamba 3D. The solution is then checked if it fulfills all the constraints. If the solution violates at least one of the three constraints, it is multiplied with the penalty function and receives a very low fitness value and is ranked low in a list of solutions. If the solution is acceptable, it gets a high fitness value and is ranked high. Before starting a new optimization loop, the evolutionary algorithm evaluates the solutions and the good ones are crossbred to then create even better starting values and solutions for the next loop, as explained in Section 3.1.2.

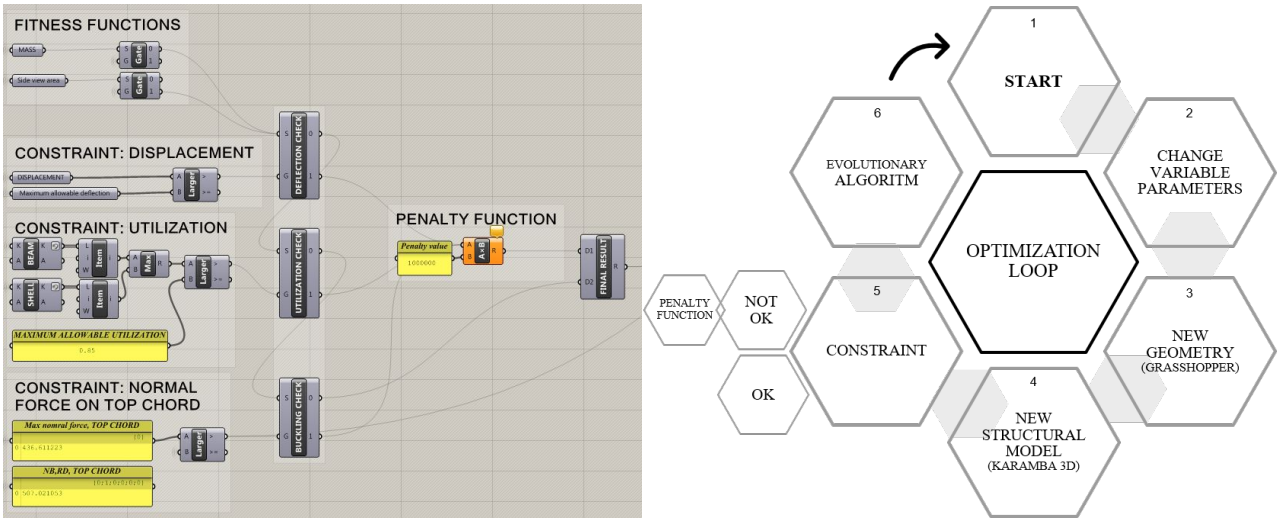

(a) (b)

Figure 5.2: (a) Grasshopper script that penalize the fitness functions if the solutions violates any of the implemented constraints. (b) Optimization procedure consisting of many loops.

In the optimization plug-ins, Galapagos and Octopus, specific initial conditions are defined before starting. The settings for the single-objective plug-in Galapagos are presented in Table 5.4a and the settings for the multi-objective plug-in Octopus are presented in Table 5.4b.

Description	Galapagos
Max. stagnant	50
Maintain	5 %
Inbreeding (+)	75 %
Population	100
Initial boost	2

(a)

Description	Octopus
Elitism	0.5
Mutation probability	0.1
Mutation rate	0.5
Cross over rate	0.8
Population	100
Initial boost	2

(b)

Table 5.4: Settings in: Single-objective optimization plug-in Galapagos (a), multi-objective optimization plug-in Octopus (b).

All values in Table 5.4a and Table 5.4b are default values, except the ones for the population and initial boost for Galapagos. Technically having the default values of 50 and 2 for the population and initial boost respectively, it would not be exactly comparable with the results from Octopus. Based on this, the same values are preset for Galapagos as for Octopus, also giving the opportunity to avoid local maximums and minimums.

5.3 Optimization procedures

In this thesis the aim is to first investigate how the results between the single- and multi-objective optimization plug-ins Galapagos and Octopus differ, henceforth called part 1. This is executed by

using the case study as an initial condition and then optimizing it with the two plug-ins. The procedure when optimizing is shown in Table 5.5 and starts with Galapagos, which first aims to minimize the mass of the footbridges (run A to C). In the first run (A), only the topology is changed, i.e. $n_{\triangle}$ as well as n_{cb} are variable parameters, and the cross-sections are kept constant as in Table 4.5. In a second run the topology, as can be seen in Figure 4.3, is fixed and the cross-sections are variable to detect if the mass can be reduced once the topology is fixed, seen as run B in Table 5.5. In a third run (C), both the cross-sections of the elements and the topology of the bridge can be changed, see Table 5.5. The optimization procedure for the transparency will undergo the same three steps (run D to F in Table 5.5). To increase the chance of Galapagos finding a global optimum, run C and F in Table 5.5 are executed three times. First, the optimization starts with parameters from the case study. Thereafter, the optimization starts with the results from the previous optimization.

Table 5.5: Procedure of the optimization with Galapagos and Octopus, called part 1. For part 1 only the Warren sub model with a span length of 20 m is considered.

Plug-in	Optimization run	Cross-section	Topology	Fitness function	Repetitions
Galapagos	A		x	Mass	1
	B	x		Mass	1
	C	x	x	Mass	3
	D		x	Transparency	1
	E	x		Transparency	1
	F	x	x	Transparency	3
Octopus	G	x	x	Mass and transparency	3

After using the single-objective optimization plug-in Galapagos, the multi-objective optimization plug-in Octopus is used, optimizing the parameters for both the cross-sections and the topology, optimizing both mass and area, run G in Table 5.5. Also in this case the optimization is executed three times.

Secondly, the aim is to investigate which solution is the most optimal one for a given span length, having the bridge width and height constant with the values 2.7 m and 1.4 m respectively, which is henceforth referred to as part 2. Now all the three sub models, Warren, Pratt and Howe, are considered and the sub models are optimized with Octopus for the span length 10 m, 20 m and 30 m, see Table 5.6. These sub models are evaluated by optimizing the mass and transparency while changing both topology and cross-sections at the same time. Also in this case, the optimization is execute 3 times for each span length, starting with the initial condition of the case study, see Table 4.5 and with $n_{\triangle}$ and n_{cb} equal to 5 respectively. The repetitions are then based on the optimization solutions from before. The reason why only Octopus is used, is the more efficient way of optimizing, considering the number of fitness function which can be optimized at the same time.

Table 5.6: Procedure for the second part of the optimization, where the most optimal solution for a given span length is sought, referred to as part 2.

Plug-in	Span length	Geometry	Cross-section	Topology	Fitness function	Repetitions
Octopus	10 m	All 3	x	x	Mass and transparency	3
	20 m	All 3	x	x	Mass and transparency	3
	30 m	All 3	x	x	Mass and transparency	3

6 Results of optimization of Warren, Pratt and Howe trusses

In this chapter the results from the optimization of part 1 and part 2, mentioned in Section 5.1, are presented. Part 1 includes the comparison of the results from Galapagos and Octopus for the Warren sub model with a span length 20 m and part 2 reveals the best optimization results for the span length of 10 m, 20 m and 30 m for all three sub models.

6.1 Part 1 - Galapagos versus Octopus

As explained in Section 5.1, the Warren truss bridge is first optimized with the same preconditions as in the case study, i.e. load case $6.10b_1$ and the bridge span of 20 m, the height of 1.4 m and the width of 2.7 m is used. In Table 6.1, the results from run A, B, C and G are presented, see Table 5.5. Run A, B and C were optimized in Galapagos and run G is retrieved from Octopus, all results having the mass as fitness value.

Table 6.1: Optimization results of the Warren truss bridge with the mass as fitness value.

	Input values	Galapagos results			Octopus result
Optimization run	Case study	A	B	C	G
Utilization of displacement	41 %	23 %	41 %	35%	29 %
Utilization of elements	77 %	88 %	99 %	96 %	92 %
Utilization of N (top chord)	86 %	70 %	94 %	87 %	98 %
Side view area [m^2]	7.74	7.85	7.14	7.05	6.25
Fitness value: Mass [kg]	8 060	7 600	7 010	6 470	6 290

The results, from the optimization of the Warren truss sub model with the mass as fitness value, show that all the new solutions have lower mass than the case study. Changing only the topology (run A) generated a slight decrease in weight, i.e. 6 % compared to the case study. Keeping the original topology but changing the cross-sections (run B) generated a solution which gave a reduction in mass by 13 %. Changing both topology and cross-sections (run C), the weight of the bridge is reduced by 20 %. The fitness value from Octopus is reduced by 22 % compared to the mass of the case study.

In Table 6.2 the results from run D, E, F and G of the Warren truss bridge, with the transparency as fitness values, are presented.

Table 6.2: Optimization results of the Warren truss bridge with the transparency as fitness value.

	Input values	Galapagos results			Octopus result
Optimization run	Case study	D	E	F	G
Utilization of displacement	41 %	21 %	22 %	24%	25 %
Utilization of elements	77 %	84 %	87 %	92 %	97 %
Utilization of N (top chord)	86 %	90 %	99 %	100 %	98 %
Mass [kg]	8 060	9 970	8 790	8 200	6 690
Fitness value: Side view area [m^2]	7.74	7.74	6.60	6.08	5.75

Looking at the results in Table 6.2, it can be stated that in run D, when only changing the topology, the side view area could not be decreased, instead the value is the same and the mass even larger than for the case study. However, only changing the cross-sections (run E) generated a side view area that is 15 % less than the one from the case study. Run F shows a solution having 21 % less side view area and Octopus, finding the best fitness value, decreased the side view area by 26 % compared to the case study.

Putting all solutions from Galapagos and Octopus together, including the case study, Figure 6.1 gives an overview. In the multi-objective optimization plug-in Octopus, the number of possible solutions after one optimization can vary. The distribution of solutions shows the best considering only mass or transparency or possible options in between, where both fitness functions are considered (Pareto-front). However, for Galapagos only one solution is retrieved after each run. As mentioned in Table 5.5, run A, B, D and E have either the topology or the cross-sections as variable parameters, while run C, F and G have both as changeable parameters.

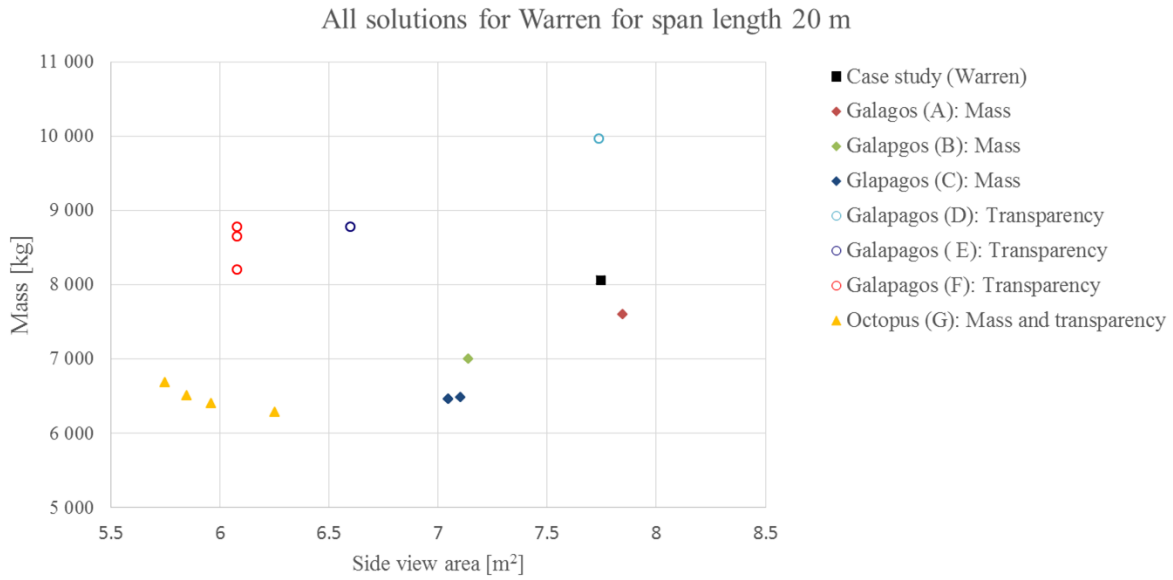

Figure 6.1: Results from the case study and the solutions for Warren 20 m optimized with Galapagos and Octopus with specified fitness values.

To summarize, all the extreme solutions in Octopus, meaning the solutions with lowest mass or highest transparency, have better values than Galapagos. Further, since Octopus generates more than one solution, Octopus contains solutions which are compromises between mass and transparency. These solutions form the non-dominated front or Pareto-front, see Figure 6.1. Even though these solutions are compromises between mass and transparency they are still optimal solutions. Thus Octopus gives the possibility to chose a solution which is between the extremes of optimizing mass and transparency, which gives more flexibility than in Galapagos. Another observation from the optimization in both Galapagos and Octopus is that the optimization in Octopus is faster than in Galapagos, also since Octopus optimizes both transparency and mass at the same time, the computation time needed, to get new results, is drastically lowered.

In Table 6.3 the two best solutions, from the optimization of the Warren sub model with a span length of 20 m, are presented. Both solutions are retrieved from optimization runs with Octopus. Comparing

the new solutions with the case study, it is apparent that the optimized results use the material more efficiently since the utilization ratios are higher. The natural frequency for mode 1 is 3.5 Hz and 5.0 Hz for the solution with the highest transparency and lowest mass respectively.

Table 6.3: The best results from the optimization of the Warren truss sub model compared with the case study.

	Initial condition	Lowest mass	Lowest side view area
Plug-in	Case study	Octopus	Octopus
$n_{\triangle}$	5	6	5
n_{cb}	5	1	1
Bottom chord	VKR 150x100x6.3	VKR 100x100x4	VKR 100x100x4
Top chord	VKR 150x150x6.3	VKR 120x120x4.5	VKR 100x100x10
Diagonals	VKR 100x60x5	VKR 100x60x4	VKR 120x60x3.6
Vertical end post	VKR 100x100x5	VKR 100x60x3.6	VKR 100x60x3.6
Cross beams	IPE 140	KCKR 219.1/12.5	KCKR 219.1/12.5
End cross beams	IPE 180	VKR 100x60x3.6	VKR 100x60x3.6
Utilization of displacement	41 %	29 %	25 %
Utilization of elements	77 %	92 %	97 %
Utilization of N (top chord)	86 %	98 %	98 %
Mass [kg]	8 060	6 290	6 690
Side view area [m^2]	7.74	6.25	5.75

In Figure 6.2 a part of the solution with lowest mass from Table 6.3 is shown with the different cross-sections. Worth noting is the height of the cross beams compared to the height of the bottom chords.

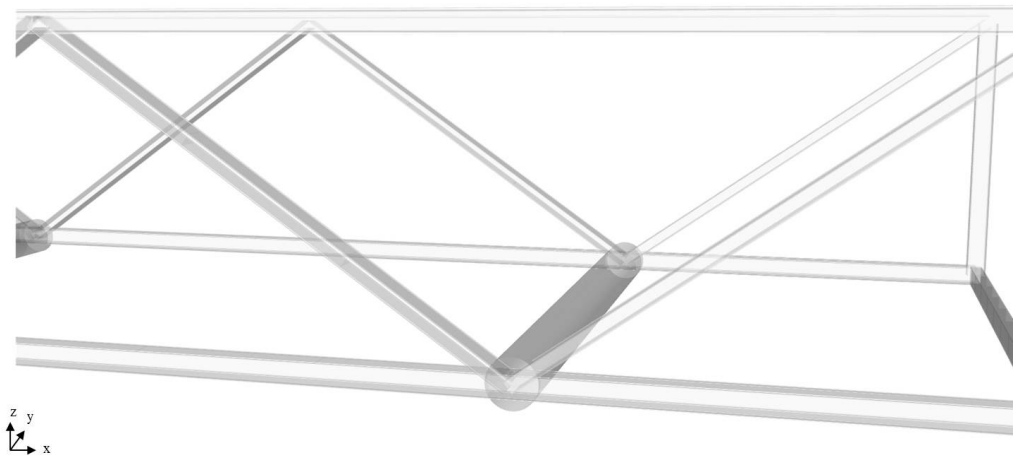

Figure 6.2: Zoom-in of the solution with lowest mass in Table 6.3.

6.2 Part 2 - Optimization of the Warren, Pratt and Howe sub models for given span lengths

In this section the results from optimization of the Warren, Pratt and Howe truss sub models with different span lengths are presented. For the results that follow, load case 6.10b_1 is used.

For the span length of 10 m, all the results from Octopus are shown in Figure 6.3. It can be stated that the Pratt truss sub model shows the best results, regarding both the transparency and the mass looking at the clear Pareto-front shown in Figure 6.3. The topology of the Pratt truss for the best solutions concerning mass and transparency is shown in Figure 6.4, since both solutions has the same topology.

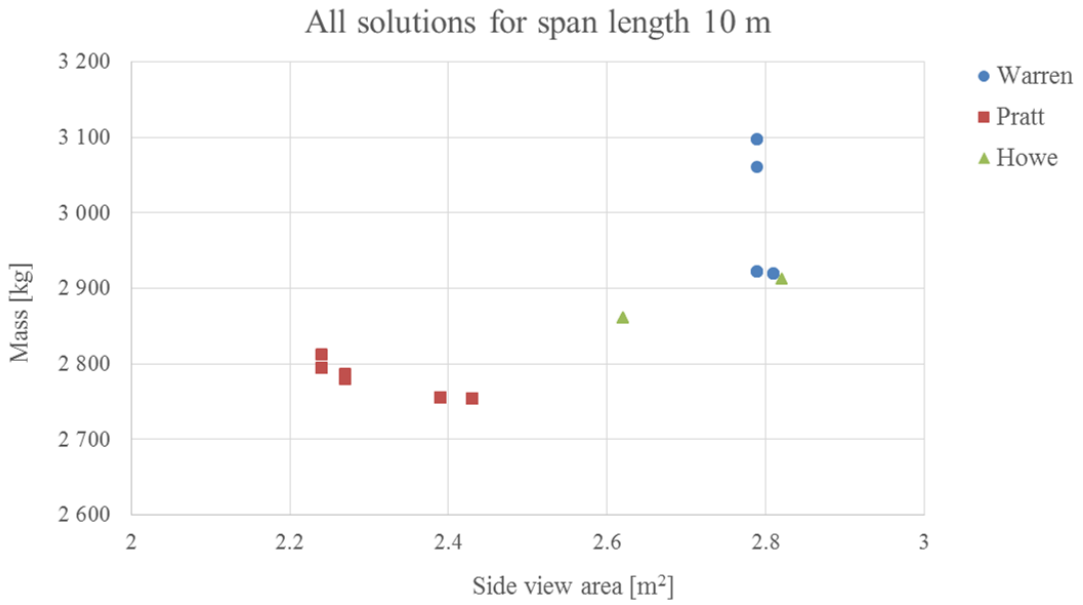

Figure 6.3: All solutions from Octopus, optimizing the Warren, Pratt and Howe sub models with a span length of 10 m.

The topology of the best results from Octopus considering both the mass is shown in Table 6.4. For a span length of 10 m, the Pratt sub model showed the best results.

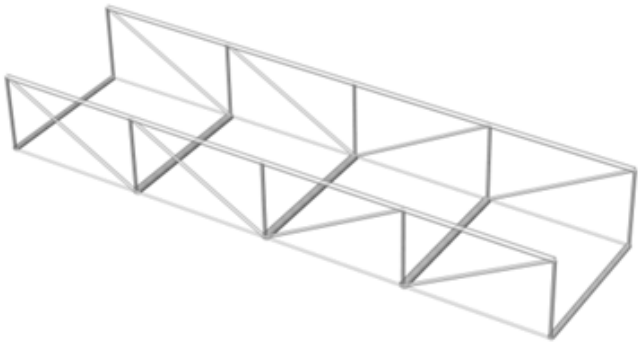

Figure 6.4: The most optimal topology for a span length of 10 m.

It can be concluded, as already seen in Figure 6.3, that the Pratt sub model has the lowest mass with a value of 2 750 kg, also having the most utilized elements and normal force capacity on the top chord. Second place is the Howe sub model differing in mass with 4 % and third place the Warren sub model, differing with 6 % compared to the Howe sub model.

Table 6.4: The best solutions of the Warren, Pratt and Howe sub models considering mass for 10 m.

	Warren	Pratt	Howe
$n_{\triangle}$	3	3 (=4)	4
n_{cb}	1	1	1
Bottom chord	VKR 100x60x3.6	KCKR 40.4/3	IPE 80
Top chord	KCKR 88.9/4	KCKR 88.9/4	KCKR 76.1/4
Diagonals	VKR 100x60x3.6	KCKR 60.3/4	VKR 100x60x3.6
Vertical end post	KCKR 48.3/3	KCKR 60.3/3	KCKR 40.4/3
Cross beams	VKR 100x100x5	KCKR 139.7/4	VKR 120x80x4
End cross beams	VKR 100x60x3.6	KCKR 101.6/4	VKR 100x60x3.6
Utilization of displacement	37 %	31 %	35 %
Utilization of elements	91 %	88 %	98 %
Utilization of N (top chord)	77 %	94 %	64 %
Side view area [m^2]	2.81	2.43	2.62
Fitness value: Mass [kg]	2 920	2 750	2 860

Looking at the transparency as fitness value, the best results for each sub model is presented in Table 6.5. As concluded before, the Pratt sub model shows the best results, one reason being the almost fully utilization of the normal force capacity in the top chord and the utilization. The next best solution is the Howe sub model, differing with 15 % compared to the Pratt sub model. The least suitable solution shows the Warren sub model, differing with 20 %.

Table 6.5: The best solutions of the Warren, Pratt and Howe sub models considering transparency for 10 m.

	Warren	Pratt	Howe
$n_{\triangle}$	3	4	4
n_{cb}	1	1	1
Bottom chord	VKR 100x60x3.6	KCKR 40.4/3	IPE 80
Top chord	KCKR 88.9/4	KCKR 101.6/6	KCKR 76.1/4
Diagonals	VKR 100x60x3.6	KCKR 40.4/3	VKR 100x60x3.6
Vertical end post	KCKR 40.4/4	KCKR 48.3/4	KCKR 40.4/3
Cross beams	VKR 100x100x5	KCKR 139.7/4	VKR 120x80x4
End cross beams	VKR 100x60x3.6	KCKR 114.3/4	VKR 100x60x3.6
Utilization of displacement	37 %	31 %	35 %
Utilization of elements	91 %	98 %	98 %
Utilization of N (top chord)	77 %	98 %	64 %
Mass [kg]	2 920	2 790	2 860
Fitness value: Side view area [m^2]	2.79	2.24	2.62

Now, analyzing the sub bridge for span length 20 m, all the results from Octopus are shown in Figure 6.5, where three quite distinct Pareto-fronts are displayed. It can be stated that the Warren sub model seems to be the best choice looking at both the mass and the transparency, followed by the Pratt sub model. The Howe sub model seems the least suitable for span length 20 m considering both mass and transparency.

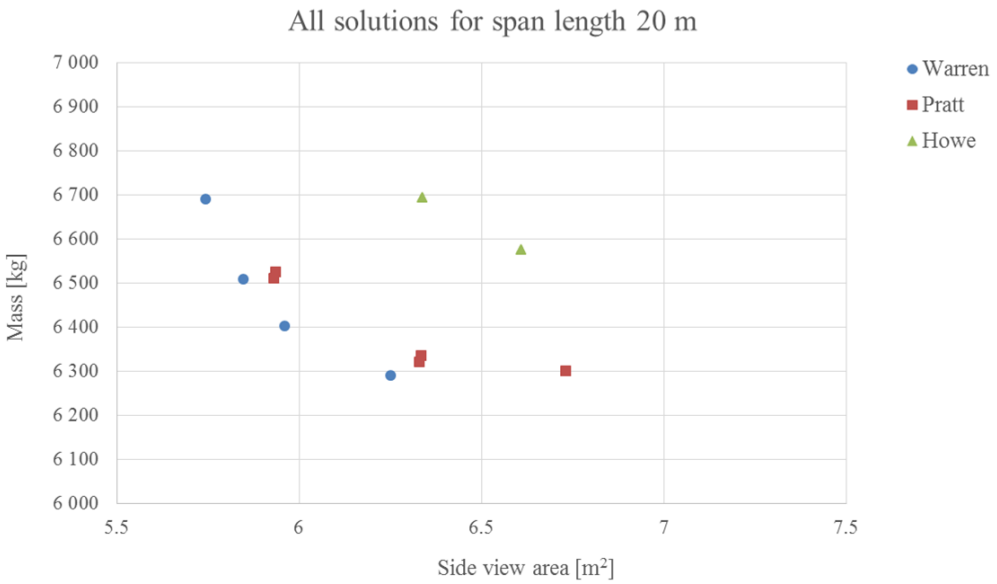

Figure 6.5: All solutions from Octopus, optimizing the Warren, Pratt and Howe sub models with a span length of 20 m.

The topology of the best optimization results, regarding both mass and transparency, for a span length of 20 m is presented in Figure 6.6.

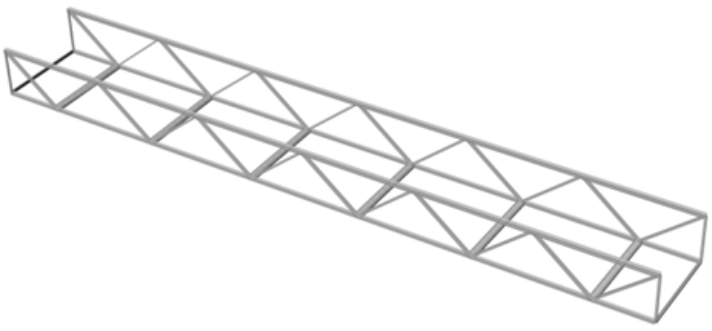

Figure 6.6: The most optimal topology for a span length of 20 m.

In Table 6.6 the best solution for each sub model, considering the lowest mass, is presented. The Warren sub model shows the best result with 6 290 kg. However, the results for the Warren and Pratt sub models are very similar and only differ with about 2 %, corresponding to 10 kg. The Howe truss bridge seems to be the least suitable choice with a mass of 6 570 kg, having a larger mass even though the utilization of the normal force capacity on the top chord and the utilization is higher than for the Warren and Pratt sub models. The Warren sub model, proving to have the best results regarding the mass, has a natural frequency (mode 1) of 5.0 Hz as mentioned in Section 6.1.

Table 6.6: The best solutions of the Warren, Pratt and Howe sub models considering mass for 20 m.

	Warren	Pratt	Howe
$n_{\triangle}$	6	5 (=6)	12
n_{cb}	1	1	1
Bottom chord	VKR 100x100x4	VKR 120x60x4	VKR 100x100x4
Top chord	VKR 120x120x4.5	VKR 120x120x5	VKR 100x100x5
Diagonals	VKR 100x60x4	VKR 100x60x3.6	VKR 120x60x3.6
Vertical end post	VKR 100x60x3.6	KCKR 76.1/4	KCKR 40.4/3
Cross beams	KCKR 219.1/12.5	KCKR 168.3/4	VKR 120x60x3.6
End cross beams	VKR 100x60x3.6	KCKR 101.6/4	VKR 100x60x3.6
Utilization of displacement	29 %	42 %	44 %
Utilization of elements	92 %	98 %	98 %
Utilization of N (top chord)	98 %	93 %	95 %
Side view area [m^2]	6.25	6.73	6.61
Fitness value: Mass [kg]	6 290	6 300	6 570

In Table 6.7, the best results considering the transparency for all three sub models are presented. As mentioned before, the Warren sub model is the best choice with an area of 5.75 m^2. Second best is the Pratt sub model, differing with about 3 %, followed by the Howe truss model with 6.34 m^2, differing with about 9 % compared to the Warren sub model. The Warren sub model, proving to have the best results regarding the transparency, has a natural frequency (mode 1) of 3.5 Hz as mentioned in Section 6.1.

Table 6.7: The best solutions of the Warren, Pratt and Howe sub models considering transparency for 20 m.

	Warren	Pratt	Howe
$n_{\triangle}$	5	5 (=6)	10
n_{cb}	1	1	1
Bottom chord	VKR 100x100x4	VKR 100x100x4	VKR 100x100x4
Top chord	VKR 100x100x10	VKR 100x100x8	VKR 100x100x5
Diagonals	VKR 120x60x3.6	VKR 100x60x3.6	VKR 120x60x5
Vertical end post	VKR 100x60x3.6	KCKR 76.1/4	KCKR 40.4/3
Cross beams	KCKR 219.1/12.5	VKR 160x80x4	VKR 120x60x3.6
End cross beams	VKR 100x60x3.6	VKR 100x60x3.6	VKR 100x60x3.6
Utilization of displacement	25 %	37 %	45 %
Utilization of elements	97 %	96 %	100 %
Utilization of N (top chord)	98 %	97 %	95 %
Mass [kg]	6 690	6 510	6 690
Fitness value: Side view area [m^2]	5.75	5.93	6.34

All the solutions obtained in Octopus for the span length of 30 m are presented in Figure 6.7. Also this time, the results show clear Pareto-fronts for each sub model. For 30 m the Warren sub model

performed the best considering mass and area. The topology of the best solutions for mass and transparency is shown in Figure 6.8, since both solutions has the same topology.

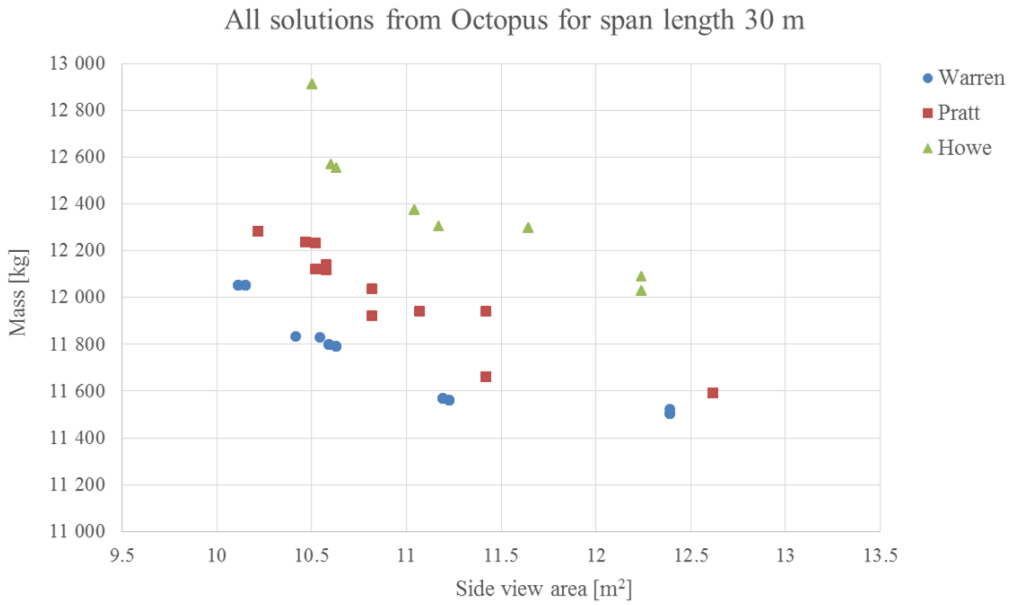

Figure 6.7: All solutions from Octopus, optimizing the Warren, Pratt and Howe sub models with a span length of 30 m.

The topology of the best optimization results, regarding both mass and transparency, for a span length of 30 m is presented in Figure 6.8.

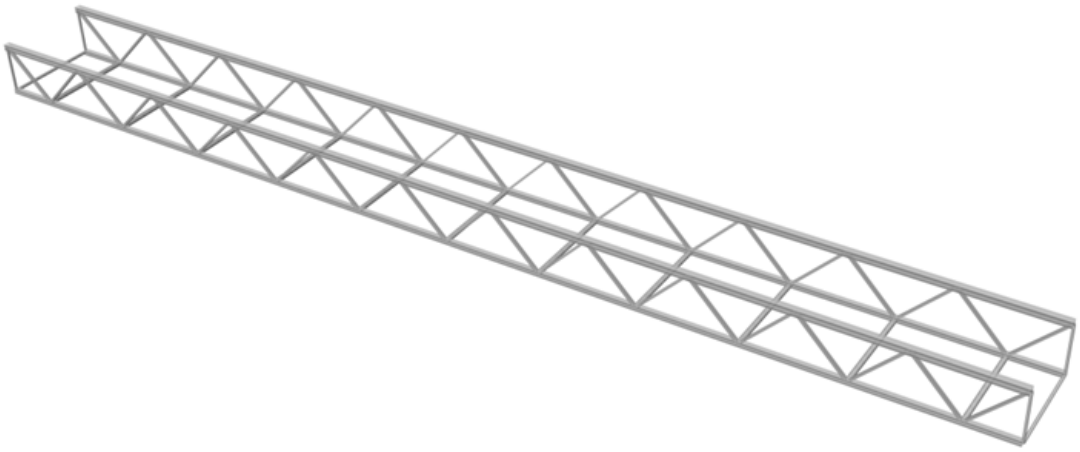

Figure 6.8: The most optimal topology for a span length of 30 m.

Presenting the best solution for each sub model with a span length of 30 m with the lowest mass, see Table 6.8, it can be stated that the Warren and Pratt sub models show a quite similar solution when looking at the mass. However, the Warren sub model gives the best solution, followed by the Pratt sub model differing with only 1 %. The solution for the Howe sub model differs with 4 % compared to the Warren sub model. All three solutions are very utilized looking at the utilization ratio and the normal force capacity of the top chord. The sub model which has the lowest mass for 30 m has a natural frequency (mode 1) of 4.2 Hz.

Table 6.8: The best solutions of the Warren, Pratt and Howe sub models considering mass for 30 m.

	Warren	Pratt	Howe
$n_{\triangle}$	11	9 (=10)	14
n_{cb}	1	1	1
Bottom chord	VKR 140x140x6.3	VKR 140x140x6.3	VKR 100x100x10
Top chord	VKR 180x180x6.3	VKR 180x180x6.3	VKR 160x160x6.3
Diagonals	VKR 100x60x4	VKR 120x60x4	VKR 160x80x4
Vertical end post	KCKR 76.1/5	VKR 120x60x3.6	KCKR 40.4/3
Cross beams	KCKR 139.7/4	VKR 140x70x4	VKR 120x60x4
End cross beams	KCKR 88.9/4	VKR 100x100x4	120x60x3.6
Utilization of displacement	51 %	58 %	59 %
Utilization of elements	99 %	100 %	99 %
Utilization of N (top chord)	98 %	97 %	97 %
Side view area [m^2]	12.39	12.62	12.24
Fitness value: Mass [kg]	11 500	11 590	12 030

Looking at the best solutions considering the transparency, the Warren sub model performs with the highest transparency, followed by the Pratt sub model with 1 % difference. The solution of the Howe sub models differs with 4 % compared to the Warren sub model, representing the least suitable solution considering the transparency for a span length of 30 m. Still, the results do not differ a lot. The sub model with the highest transparency has a natural frequency (mode 1) of 4.4 Hz.

Table 6.9: The best solutions of the Warren, Pratt and Howe sub models considering transparency for 30 m.

	Warren	Pratt	Howe
$n_{\triangle}$	12	10	14
n_{cb}	1	1	1
Bottom chord	VKR 100x100x10	VKR 100x100x10	VKR 100x100x10
Top chord	VKR 140x140x10	VKR 140x140x10	VKR 120x120x10
Diagonals	VKR 120x60x3.6	VKR 120x60x4	VKR 140x70x6.3
Vertical end post	KCKR 76.1/5	VKR 100x60x6.3	KCKR 40.4/3
Cross beams	KCKR 139.7/4	VKR 160x80x6.3	KCKR 139.7/4
End cross beams	KCKR 101.6/4	VKR 100x100x4	VKR 140x70x4
Utilization of displacement	46 %	51 %	53 %
Utilization of elements	94 %	97 %	100 %
Utilization of N (top chord)	100 %	98 %	100 %
Mass [kg]	12 050	12 280	12 910
Fitness value: Side view area [m^2]	10.12	10.22	10.50

7 Discussion

This chapter starts off with a discussion about the results in part 1, i.e. the comparison of the results between Galapagos and Octopus. Thereafter a discussion of the results from part 2, where the most optimal solutions for the different span lengths of 10 m, 20 m and 30 m are debated. Finally, a discussion of the model in Karamba 3D and its verification results is introduced, concluding in an analysis of the optimization results.

7.1 Part 1 - Galapagos versus Octopus

Starting with the comparison of the results with load case $6.10b_1$ in Galapagos and Octopus, see Table 6.1 and Table 6.2, it can clearly be stated that Octopus concluded in the best result both having the mass and area as fitness values. In Table 7.1 the different runs are presented again to facilitate the understanding of the discussion which follows.

Table 7.1: Procedure of the optimization with Galapagos and Octopus, called part 1. For part 1 only the Warren sub model with a span length of 20 m is considered.

Plug-in	Optimization run	Cross-section	Topology	Fitness function	Repetitions
Galapagos	A		x	Mass	1
	B	x		Mass	1
	C	x	x	Mass	3
	D		x	Transparency	1
	E	x		Transparency	1
	F	x	x	Transparency	3
Octopus	G	x	x	Mass and transparency	3

Investigating the results from Galapagos, optimization run A/D show the worst fitness values. Looking at run D, the side view area could not even be decreased, moreover resulting in an even larger mass than the case study. For run A/D the topology was a variable parameter, only offering two values to be changed resulting in few possibilities to optimize with. Therefore it is difficult for Galapagos to find a good fitness value for the solutions, leading to a longer computation time than for run B/E. Still, the best result from run A has a better fitness value than the initial condition being the case study.

Run B and E in Galapagos, having the cross-sections only as variable parameter, gives better fitness values than run A and D, which is due to the fact that the topology from the case study is already quite optimal, but not the cross-sections with the given constraints implemented in Karamba 3D. Also, the range of cross-sections is large, giving the plug-in more options and combinations to optimize with, which ends up in a shorter computation time as for run A/D.

Run C and F in Galapagos, having both the topology and the cross-sections as a variable parameters, offer the plug-in a lot of different possible combinations to optimize with, which results in the best fitness value looking at the results from Galapagos. Still, the computation time for Octopus is much faster and the best result even better. This can be explained by the optimization algorithm used in Octopus, SPEA-2, which is more powerful than the GA used in Galapagos. Since Octopus, as

mentioned in Section 3.1.2, stores the best solutions in an archive and uses this to mutate the population, the population is less likely to be trapped in a local optimum than Galapagos, which relies only on the current population to find the optimal solution.

Having a more detailed look at the best results with the mass as fitness value, see Table 6.1, it is interesting to analyze the utilization of the three constraints. Run G from Octopus shows a 98 % utilization for the normal capacity of the top chord, while run C from Galapagos has a value of 87 %. Both values are high, but the result from Octopus is more utilized, having this as the limiting factor, as it is the highest number of all utilization ratios for run G. Run C on the other hand seems to have the utilization of the elements as the limiting value, reaching 96 %. The best result from Octopus shows a value of 92 %. The utilization of the displacement seems not to be limiting at all, both considering the best solution in Galapagos and Octopus, with a utilization of 35 % and 29 % respectively.

Analyzing the results with the side view area as fitness value, see Table 6.2, the results from Octopus are almost fully utilized both considering the normal capacity of the top chord and the utilization with the values 98 % and 97 % respectively. The best result from Galapagos, run F, is fully utilized looking at the normal capacity of the top chord, 100 %, and quite utilized looking at the utilization ratio, 92 %. For both Galapagos and Octopus, the utilization of the normal capacity seems to be the limiting value. The utilization of the displacement is again not at all decisive with 24 % and 25 % for run F and G respectively.

Investigating the details of the best results for the lowest mass and highest transparency, see Table 6.3, the first reflection is that both solutions are very similar. Looking at $n_{\triangle}$, the best solution, having the mass as fitness value, has $n_{\triangle}$ equal to 6, while the best solution with the transparency as fitness value and the case study both have $n_{\triangle}$ equal to 5. The difference compared to the case study lies though in n_{cb}, which is equal to 1 for both optimized solutions, whereas it is 5 for the case study. It can also be stated that the dimensions of the cross-section of the cross beams for both optimization solutions are rather large, having KCKR 219.1/12.5 as a suggestion. The result of n_{cb} being equal to 1 gives rise to several issues that will be further discussed in Section 7.4.

It is rather understandable that Octopus, having the transparency as fitness value, tries to increase the dimensions of the cross beams as much as possible while decreasing the side view dimensions for the cross-sections for the top and bottom chord, the diagonals and the vertical end posts as much as possible, knowing that the dimensions of the cross beams, including the end cross beams, do not affect the side view area at all.

Worth mentioning is the fact why the focus did not lie in how the case study could be optimized. The two main differences are two details which were not implemented in the optimization, which are considered in the case though. The first difference is the calculation of the end cross beams, which was constructed to withstand a change of the bearings used for the supports in the case over Genevadsån, but not in the model in Karamba 3D. This resulted in a somewhat larger cross-section of the end cross beam compared to the optimization results from Galapagos and Octopus. The second difference is the c-c distance of the cross beams, which in the case over Genevadsån considers the deflection of the bridge deck, which is not included in the optimization results. This is further discussed in Section 7.3.

7.2 Part 2 - The Warren, Pratt and Howe sub models for given span lengths

Looking at the best solutions for each span length, the optimization results show that the Pratt truss gives the best results for a span length of 10 m and the Warren truss bridge for span length of 20 m and 30 m. However, when analyzing the results more in detail, it is not so obvious which sub model actually is the best one.

From Tables 6.4 and 6.5, the utilization ratios of the normal force capacity in the top chord for the Warren and Howe sub models for span length 10 m seems to be low, with the corresponding values of 77 % and 64 % for both mass and area. For the Pratt sub model, these values are 94 % and 98 % respectively. Looking at the utilization of the elements, the numbers are quite high for all three sub models, both having the mass and transparency as fitness values. Based on this, the possibility arises that the Warren and Howe sub models have potential to be further optimized, while the Pratt sub model is almost fully utilized considering the normal force capacity on the top chord and the utilization and therefore gives the best results. Looking at the final fitness values of a span length of 10 m, the Howe sub model gives the second best results, which are very close to the ones from the Pratt sub model. This, even though the solution is not as fully utilized as the Pratt sub model. Therefore it is difficult to say, which sub model is the most suitable one for a span length of 10 m, as they are not quite comparable.

Analyzing the results for span length 20 m, the Warren sub model gives the best results. For span length 20 m, all three sub models are almost fully utilized considering the normal force capacity on the top chord and the utilization. This makes the comparing process more equitable, showing very similar results between the Warren and Pratt sub model. In fact, The Warren sub model only differs with less than 1 %, corresponding to 10 kg, looking at the best solution considering the mass and 3 %, corresponding to 0.18 m^2, considering the best solution for the transparency, compared to the Pratt sub model.

As mentioned in Section 4.4, $n_{\triangle}$ can only be an even number for the Pratt and Howe trusses. Therefore, as shown in Table 6.6, for a span length of 20 m, the Warren and the Pratt sub models have the same topology with $n_{\triangle}$ equal to 6 and n_{cb} equal to 1, whereas the Howe truss has the double amount of $n_{\triangle}$, 12, than the other two sub models. However, this allows the Howe truss to have more slender beams even though it has more diagonals, which in the end still ends up in a larger mass and side view area.

Investigating the results with a span length of 30 m, the Warren sub model shows the best results again. Also for these results, the utilization ratios are almost maximized to 100 % for all three sub models, except the one considering the displacement. The utilization of the displacement did increase to about 50 % for all three sub models, which seems reasonable as the span length increased.

Looking at the results with the mass as fitness value, the Warren and Pratt sub models showed quite similar results, 11 500 kg and 11 590 kg respectively, with almost the same topology. The best solution for the Warren sub model proposes $n_{\triangle}$ to be equal to 11, whereas the Pratt sub model has $n_{\triangle}$ equal to 10. The Howe bridge has some additional verticals and diagonals with $n_{\triangle}$ equal to 14. For all three cases n_{cb} equal to 1 is proposed.

The results having the transparency as fitness value are very similar for all three cases with 10.12 m^2, 10.22 m^2 and 10.50 m^2 for the Warren, Pratt and Howe sub model respectively. The Warren sub model has in this case $n_{\triangle}$ equal to 12, whereas the Pratt sub model has $n_{\triangle}$ equal to 10, giving the second best solution. The cross-section for the elements that influence the side view area are exactly the same, except the vertical end posts, being the decisive factor for the Warren sub model, together with two more $n_{\triangle}$.

To summarize, studying the results from the best solutions for 10, 20 and 30 m, it is apparent that the deflection criterion was never the limiting constraint for the optimization. Rather the utilization ratio of the elements or normal force capacity in the top chord are factors that limit the design. Since the deflection demand according to Krav TDOK 2016:0204 section B.3.4.2.1 states that only the frequent values of the load combinations are needed to check the deflection in SLS, the self-weight of the structure was ignored. Thus, even for larger span lengths, as for instance 30 m, the utilization of the displacement lies around 50 %, whereas the utilization of the elements and utilization of the normal force capacity are closer to 100 %.

All in all, considering the results for all studied span lengths in Section 6.2, there is no clear winner between the sub models, rather there are clear losers. Having the worst results, for all but one of the studied span lengths, the Howe truss is indeed the worst sub model considering the chosen fitness values. Whereas for the winner, it could be argued that both the Warren and the Pratt work equally good for these studied span lengths, with the Pratt being better at 10 m, both being approximately equal at 20 m and the Warren being a better solution at 30 m.

7.3 The model in Karamba 3D and its verification results

Considering the verification as mentioned in Section 4.3, there is a fundamental difference between how Karamba 3D and FEM-Design calculates the utilization of structural elements. The main problem is that there are two possible methods to calculate the interaction factors in EC3, which explains some of the differences between the verification results in Karamba 3D and FEM-Design. The possibility to investigate changes in the calculation procedure in Karamba 3D could be initiated in further studies if desired, resulting in better verification results with FEM-Design.

To get sectional forces for the sub models in Karamba 3D that correspond to the sub models in FEM-Design, the bridge deck had to be weakened with a factor of 10 000. This, as the behaviour and optimization of the bridge deck was out of interest in this thesis and the focus only relied on the truss footbridge structure and its behaviour. Naturally, weakening the bridge deck means that it has no stiffness and therefore can take no load. Although the sub models in Karamba 3D have sectional forces that correspond well to the sectional forces in FEM-Design, the weakened bridge deck causes problems in other areas of the structural analysis.

First, as mentioned in Section 7.1, the deflection of the bridge deck is large, since it has no stiffness and therefore needs to be ignored when looking at the maximum displacement of the bridge. Even if the bride deck would have a weakening factor 1, the displacements would be rather big as the distances between the cross beams are large in the optimization results, see Chapter 6. Secondly, the natural frequencies of the sub models cannot be introduced in the optimization runs of the sub

models with a weakened bridge deck, since this leads to really low natural frequencies as it is very flexible. The verification results of the natural frequency with a weakening factor 1 for the Warren sub model showed very good results though, indicating that it can be relied on but cannot be a part of the optimization as the bridge deck is weakened with a factor 10 000.

Discussing the topic of Karamba 3D, there are mainly three issues with the software. First, the global treatment of all analysis, meaning that Karamba 3D performs well looking at the structural behaviour locally. Globally, the answers are hard or even impossible to find. This was the reason why the extra script with the calculations for the normal force restriction on the top chord considering LT-buckling was implemented, as this check did not exist globally in the calculations in Karamba 3D, only locally. Also, the issue with the buckling length comes into this subject, as Karamba 3D finds it hard to define the length and behaviour of a beam, which needs to be defined manually to be sure of the right interpretation from Karamba 3D.

The second issue is the post processing in Karamba 3D, which is very time consuming. All solutions, looking for instance at the sectional forces, can be found in lists, which are hard to understand and locate onto the elements in the bridge. There is also an alternative to see the solutions for the sectional forces in a visual picture with numbers, which has the disadvantage though to put several numbers on top of each other, making it hard to read. Furthermore, the results need to be found and typed into an external sheet manually, which opens up and allows the possibility of writing errors. There are ways in Karamba 3D to store the results in excel sheets, which was tried and neglected as the update of the numbers in the excel sheet was unreliable and inaccurate.

The third problem is the definition of the behaviour of all joints in the structure. According to the definition in Karamba 3D, if the elements are connected to each other with no further input, the connection is rigid. If the properties of the joint should be changed, the specific node is to be found and the properties changed. This was executed when applying a unit load of 1 000 kN, retrieving the δ to calculate the spring stiffness. The issue is though, that finding this exact node needs to be generalized, as the optimization brings a change of topology and cross-sections with it. The process of generalizing the search of a specific node, in list that consists of a lot of nodes, with varying orders in the system is very time consuming.

7.4 Overall optimization results

Having a look at the constraints used in this thesis, which are the maximum displacement, the maximum utilization ratio of an element and N_{bRd} being the maximum reduced normal capacity of the top chord, the subject can be more expanded. For instance, continuing on the discussion from before, Section 7.2 states that all solutions obtained with Octopus have n_{cb} equal to 1. This gives rise to the issue of the displacement between the cross beams, should there be a bridge deck. As the bridge deck is not considered in the optimization in this thesis, there is no problem, as both solutions from Octopus fulfill the implemented constraints. In reality though, when there actually is a bridge deck, the issue can be solved by implementing a constraint. This could be executed locking the maximum c-c distance of the cross beams, which is adapted to geometry and properties of the bridge deck and its maximum allowable displacement. Further, the first mode of the natural frequency could be added as a constraint, which would restrict the solutions to be above 5 Hz, to avoid further investigations of the natural frequency.

It is of course of importance to adapt the sub models and optimization results to the reality and aim for the actual possibility that the footbridges can be constructed. The results obtained from the optimization runs using Galapagos and Octopus do for instance not consider the production of the footbridges, meaning that the possibility to weld the different connections of the cross-sections is not considered. Since no constraint was introduced restricting the maximum height of for instance the cross beams to the the height of the bottom chord, unreasonable solutions were obtained, which can be seen in Figure 6.2. This can also be solved, implementing additional constraints adapting the connection of the elements. Practically this would mean restricting the height of the cross beams to be less or equal to the height of the bottom chord. The diagonals and vertical end posts cannot be wider than the width of the bottom chord and top chord. These restrictions would ensure that the bridge could actually be constructed.

Further, as welding is rather expensive, this could be implemented as a constraint, only allowing as few connections of elements as possible. Also, the number of different dimensions and cross-sections within one footbridge could be minimized, to facilitate the production of the footbridges. Additionally, most optimization results seem to have KCKR cross-sections for the cross beams, which might not be preferable considering the application of a bridge deck for instance. This could also easily be implemented as a constraint, where the allowable cross-sections for each element can be restricted or further expanded. The possibilities for the designer to specify the optimization and its constraints are endless.

A final constraint could be to implement the calculations of a replacement of the bearings of the supports. If this load case and restriction were to be implemented, as it was in the case study which is discussed in Section 7.1, the final optimization results of the structure would contain larger end cross beams.

The fitness functions chosen in this thesis were the mass and the transparency of the footbridges. Starting with the mass, it might not always be good to reduce the mass as much as possible, for instance looking at the dynamics of the sub models, since reducing the mass leads to lower natural frequency, which is not looked into in detail in this thesis. Further, obvious but still important, only using transparency as a fitness function showed to be sub-optimal since the mass of the sub-models was increased, which is an unwanted side effect. Thus, only using transparency as a fitness function serves no purpose. However, in combination with mass as a fitness function it works to give the bridge a more slender expression.

In this thesis only the extremes of the solutions in Octopus were presented. However, Octopus generates several Pareto-optimal solutions, the best trade offs between the fitness functions. These solutions give the designer the choice to weigh the preferences in mass or transparency. There is no actual optimal solution, it all depends on if the designer is more concerned about the mass or the transparency of the footbridge.

The variable parameters in this thesis were $n_{\triangle}$, n_{cb} and the cross-sections. These allowed the optimization plug-ins, Galapagos and Octopus, to choose from quite a large range; turning out to be almost too large, as it affected the optimization time. A recommended restriction is for instance to limit the number of cross-sections to the ones longed for, looking at the design, and the ones most likely to be used. Also, additional cross-sections and properties could be added or replace the ones

used in this thesis. Additionally, when optimizing with the cross-sections as variable parameters, the number of different cross-sections which are the same should be rewarded. This, to maybe match the expectancy of the reality, where 5 different cross-sections in one footbridge might not be appreciated.

Based on the experience when optimizing in Galapagos and Octopus, it can be stated that one optimization run can take time, for instance an optimization run in Galapagos takes between 1.5 - 4 hours. As has been stated in Section 7.1, Octopus is faster than Galapagos considering the computation time and also gives better results due to the more advanced algorithm used. An optimization run in Octopus often took less than 1 hour to complete, which could be reduced with a few adjustments to the script.

One reason for the long optimization time could be the way the structure of the model is built up. Having quite a lot of variable parameters plus an inexperienced background when starting this project, the structure of the model could probably be more efficiently rebuilt, thus reducing the computation time. Another way to reduce the computation time could be to adapt the settings in Galapagos and Octopus, depending on if the designer prioritizes to find the most optimal solution or a short computation time.

In this thesis the settings in Galapagos and Octopus were set to a population of 100 and a initial boost of 2. This choice is based on the default values in Octopus, which was adapted in Galapagos. To make sure how the setting should be preset, among others depending on the number of fitness functions and variable parameters, a sensitivity analysis should be executed to find the optimal presetting conditions. Moreover, the number of repetitions of an optimization until the best utilized result is met, can be debated and investigated.

All in all, the possibilities for the designer are endless. A lot of more aspects regarding cost and environmental analyses could be implemented, including the whole process of the development of steel truss footbridges. For instance the life cycle assessment of the footbridges could be implemented, introducing the choice of material, its transportation, the procedure of construction until the disassembling of the bridges at the end of the lifespan. Further, the optimization results in this thesis only consider steel elements with standard dimensions, which probably is most accurate and useful as the demand looks like today. In the future though, when optimized and unique shapes become more available and the belonging standards are introduced, this gives the possibility to deviate from the standard dimensions. This would probably result in even better results, regarding the chosen fitness functions. This is an amazing opportunity that is handed over to the designers and Civil engineers in the future though.

8 Conclusion

In this thesis a computational script of the superstructure of steel truss footbridges was created in Grasshopper and translated into a parametric model with structural elements in Karamba 3D, based on Swedish norms and regulations. The model was optimized with the single- and multi-objective optimization plug-ins Galapagos and Octopus, to minimize the mass and maximize the transparency of the structures.

First, it can be concluded that the script, the way it is built, and its results with respect to sectional forces and maximum displacement are reliable, if the bridge deck is weakened with a factor 10 000. There are some limitations that the user of Karamba 3D needs to be aware of, for instance the results considering the utilization of the elements. The difference lies in the calculation methods used in Eurocode; FEM-Design uses method 1 and Karamba 3D uses method 2 to calculate the interaction factors. The second limitation is the global LT-buckling, which is not automatically included in the calculations in Karamba 3D, but was implemented as an additional constraint and works for the intended purpose. The natural frequency of mode 1 works for the Warren sub model and gives satisfying results, if the weakening factor is changed to 1, i.e. the stiffness of the bridge deck is not weakened.

Secondly, the conclusion considering the optimization plug-ins Galapagos and Octopus is the fact that Octopus is more beneficial to use than Galapagos. This mainly due to the fact that problems in structural engineering seldom can be condensed into one simple fitness function and thus there are needs to express the problem using multiple fitness functions, as was the case in this thesis. Also, Octopus needed less computation time and gave more solutions to choose from than Galapagos which only gives one solution, often at the cost of other potential fitness functions. In combination with the fact that all solutions from Octopus are optimal, it gives more options which are possible for a preliminary design. Furthermore, the best solutions in Galapagos were worse than the best solutions obtained with Octopus. The reason for Octopus finding better solutions is due to the more advanced optimization algorithm used.

Thirdly, it can be concluded that the Howe sub model preformed the worst out of all trusses. Also, it can be said that for 10 m the Pratt sub model is the best geometry and for 20 m as well as for 30 m the Warren sub model is the best. It needs to be pointed out though, that both Warren and the Pratt sub model are viable results for 20 m and 30 m, since the differences between them are almost negligible.

Finally, the developed model can be used in preliminary design to give a good initial estimation of cross-sections and topology for the three included sub models. Since Octopus gives a variety of results in a short time the preliminary design process could be reduced. This information could then be used further as initial values for the detailed design. At the same time the user should be aware of all the possibilities that the model now offers, regarding development of constraints for instance, which is discussed in Section 7.4. Now as the basis script is created, there is an opportunity to develop it further and adapt all the constraints and preferences that the designer desires. Some examples of further studies, which could be implemented to develop the script and model, are explained in Section 8.1.

8.1 Further studies

In this section suggested improvements to the model as well as topics for further studies are proposed.

- Additional geometries, not only truss bridges could be added, verified and developed to broaden the span of design choices.
- The possibility of adding more loads, for instance wind and temperature loads, should be investigated further. Additionally, the opportunity of adding extra supports as well as the new load combinations that come with it could be introduced and analyzed. Also, the service vehicle, or moving concentrated loads in general, could be implemented.
- The issue of the bridge deck could be solved to allow the possibility to introduce constraints regarding natural frequencies and deflections of the bridge deck.
- The calculation procedure of the utilization of the elements in Karamba 3D could be reprogrammed to achieve a better coherence with the utilization ratios in FEM-Design.
- More fitness functions and constraints could be introduced to steer the optimization process towards designs that are more feasible, which is mentioned in Section 7.4.
- Galapagos and especially Octopus are powerful tools regarding optimization. Nevertheless, it would be beneficial to conduct a sensitivity analysis for Octopus and Galapagos to determine how large the population and other initial values need to be to get fast and/or accurate results. It would be of interest to see how the initial values should be set for any amount of parameters and fitness functions.
- Other materials than steel could be introduced - for instance fibre reinforced polymers, reinforced concrete and timber - and their behaviour in Karamba 3D investigated, which sets the basis for further and a more broadened opportunities to optimize.
- Finally, economical and environmental assessments and aspects could be implemented in the optimization.

References

Ahston, C., Aldin, N., Andersson, J.-O., Gustafsson, Å., Hedgren, E., Lidegran, G., … Slunga, K. (2017). *Trafikverkets strategiska inköpsarbete samt arbete med att arbetsrättsliga krav efterlevs i upphandlad verksamhet*. Borlänge. (Cited on pages i, 1, 7).

Alexandersson, S. (2014). Halmstads kommun , Teknik- och fritidsförvaltningen Ny gång- och cykelbro över Genevadsån Bakgrund. *2*, 1–7. (Cited on page 19).

Bader, J., Zitzler, E., & Rudolph, G. (2010). Hypervolume-based search for multiobjective optimization: theory and methods. *Optimization*, 1–310. Retrieved from https://sop.tik.ee.ethz.ch/publicationListFiles/bade2010a.pdf. (Cited on page 15)

Bader, J. & Zitzler, E. (2011). HypE: An Algorithm for Fast Hypervolume-Based Many-Objective Optimization. *Evolutionary Computation*, *19*(1), 45–76. doi:10.1162/EVCO_a_00009. (Cited on page 15)

Balling, R. J., Briggs, R. R., & Gillman, K. (2006). Multiple Optimum Size/Shape/Topology Designs for Skeletal Structures Using a Genetic Algorithm. *Journal of Structural Engineering*, *132*(7), 1158–1165. doi:10.1061/(ASCE)0733-9445(2006)132:7(1158). (Cited on page 1)

Bates, W. & Fistructe, C. (1991). HISTORICAL STRUCTURAL STEELWORK HANDBOOK Properties of U .K . and European Cast Iron, Wrought Iron and Steel Sections including Design, Load and Stress Data since the Mid 19th Century. (Cited on page 8).

Beck, A. T. & Gomes, W. J. D. S. (2012). A comparison of deterministic, reliability-based and risk-based structural optimization under uncertainty. *Probabilistic Engineering Mechanics*, *28*, 18–29. doi:10.1016/j.probengmech.2011.08.007. (Cited on page 10)

Berns, H. & Theisen, W. (2008). *Ferrous materials: Steel and cast iron*. doi:10.1007/978-3-540-71848-2. (Cited on page 6)

Bhadeshia, H. & Honeycombe, S. R. (2006). Iron and its Interstitial solid solutions. In H. Bhadeshia & S. R. Honeycombe (Editors), *Steels: Microstructure and properties* (Third, Chapter 1, Pages 1–16). ASM International. doi:https://doi-org.proxy.lib.chalmers.se/10.1016/B978-075068084-4/50003-0. (Cited on page 6)

Black, J., Hashimzade, N., & Myles, G. (2017). A Dictionary of Economics. Retrieved February 16, 2018, from http://www.oxfordreference.com.proxy.lib.chalmers.se/view/10.1093/acref/9780198759430.001.0001/acref-9780198759430-e-837. (Cited on page 10)

Camp, C., Pezeshk, S., & Cao, G. (1998). Optimized Design of Two-Dimensional Structures Using a Genetic Algorithm. *Journal of Structural Engineering*, *124*(5), 551–559. doi:10.1061/(ASCE)0733-9445(1998)124:5(551). (Cited on pages 1, 13)

Chinneck, J. W. (2001). Chapter 17 : Pattern Search for Unconstrained NLP. *Practical Optimization: a Gentle Introduction*, (0), 1–7. (Cited on page 65).

Coello Coello, C. A. (2006). Evolutionary Multi-Objective Optimization: A Historical View of the Field. *IEEE Comput. Intell. Mag. 1*(1), 28–36. doi:10.1109/MCI.2006.1597059. (Cited on pages 1, 10, 15)

Colman, A. M. (2015). A Dictionary of Psychology. Retrieved February 16, 2018, from http://www.oxfordreference.com.proxy.lib.chalmers.se/view/10.1093/acref/9780199657681.001.0001/acref-9780199657681-e-1855%7B%5C#%7D. (Cited on page 11)

COX, H. (1965). Introduction: Theory in Design. *The Design of Structures of Least Weight*, 1–5. doi:10.1016/B978-1-4831-9755-5.50005-8. (Cited on page 10)

Craigh, R. & Kurdila, A. (2006). *Fundamentals of structural dynamics* (Second edi). John Wiley & Sons, Inc. (Cited on page 6).

Davidson, S. (2018). Grasshopper - Algorithmic modeling for Rhino. Retrieved February 26, 2018, from http://www.grasshopper3d.com/. (Cited on page 16)

Dominik Holzer, Richard Hough, M. B. (2007). Parametric Design and Structural Optimisation for Early Design Exploration. *International Journal of Architectural Computing*, *5*(4), 625–643. doi:10.1260/147807707783600780. (Cited on page 15)

Domone, P. & Illston, J. (2010). *Construction Materials: Their Nature And Behaviour* (4th) (P. Domone & J. Illston, Editors). Abdingdon: Spon press. (Cited on pages 6, 7).

Duan, L. (2017). Truss bridge. Retrieved March 2, 2018, from http://www.accessscience.com.proxy.lib.chalmers.se/content/712890. (Cited on pages 4, 5)

Dumitrescu, G. C. & Tanase, I. A. (2016). 3D Printing - A New Industrial Revolution. *Knowledge Horizons. Economics*, *8*(1), 32–39. Retrieved from http://proxy.lib.chalmers.se/login?url=https://search-proquest-com.proxy.lib.chalmers.se/docview/1793552762?accountid=10041. (Cited on page 9)

Dunning, H. (2017). The world's first 3D printed steel bridge will be a 'living laboratory'. Retrieved February 13, 2018, from http://www3.imperial.ac.uk/newsandeventspggrp/imperialcollege/newssummary/news%7B%5C_%7D20-10-2017-16-21-38%7B%5C%%7D0A. (Cited on page 9)

Eindhoven University of Technology. (2017). The world's first 3D printed reinforced concrete bridge starts to take shape. Retrieved February 13, 2018, from https://www.tue.nl/en/university/news-and-press/news/16-06-2017-the-worlds-first-3d-printed-reinforced-concrete-bridge-starts-to-take-shape/. (Cited on page 9)

Gandomi, A. H., Yang, X. S., Talatahari, S., & Alavi, A. H. (2013a). *Metaheuristic Algorithms in Modeling and Optimization* (First Edit). Elsevier Inc. doi:10.1016/B978-0-12-398364-0.00001-2. (Cited on pages 12, 13)

Gandomi, A. H., Yang, X. S., Talatahari, S., & Alavi, A. H. (2013b). *Metaheuristic Applications in Structures and Infrastructures*. doi:10.1016/C2011-0-08778-1. (Cited on page 12)

Gro, C., Oltean, M., & Oltean, M. (no date). The role of elitism in Multiobjective Optimization with Evolutionary Algorithms, 83–90. (Cited on page 15).

Gu, D. (2015). *Laser Additive Manufacturing (AM): Classification, Processing Philosophy, and Metallurgical Mechanisms*. doi:10.1007/978-3-662-46089-4_2. arXiv: arXiv:1011.1669v3. (Cited on page 8)

Gupta, M. (2017). *3D Printing of Metals* (1st edition) (M. Gupta, Editor). Basel, Switzerland: MDPI. Retrieved from http://www.mdpi.com/books/pdfview/book/384. (Cited on page 9)

Hasançebi, O., Çarbaş, S., Doğan, E., Erdal, F., & Saka, M. P. (2009). Performance evaluation of metaheuristic search techniques in the optimum design of real size pin jointed structures. *Computers and Structures*, *87*(5-6), 284–302. doi:10.1016/j.compstruc.2009.01.002. (Cited on page 10)

infra, B. (2017). Rondweg Gemert Noord-Om - Van 3D geprinte brug tot ingeschoven rotonde. Retrieved February 13, 2018, from https://www.baminfra.nl/projecten/rondweg-gemert-noord-om-van-3d-geprinte-brug-tot-ingeschoven-rotonde?position=3%7B%5C&%7Dlist=x5OsDiWF7aNwjkAvPyn67NyLsKkaMsdr02jHI1CYOps. (Cited on page 9)

Kassimali, A. (1993). Pratt truss, 1. Retrieved from http://www.areforum.org/up/GeneralStructures/must%20read/CommonTrusses.pdf. (Cited on page 5)

Kianian, B., Tavassoli, S., Larsson, T. C., & Diegel, O. (2016). The Adoption of Additive Manufacturing Technology in Sweden. *Procedia CIRP*, *40*, 7–12. doi:10.1016/j.procir.2016.01.036. (Cited on page 9)

Krauss, G. (2005). Introduction: Purpose of Text, Steel Definitions, and Specifications. In G. Krauss (Editor), *Steels - processing, structure, and performance* (Chapter 1, Pages 1–5). ASM International. (Cited on page 6).

Larsson, R. (2016). MÖJLIGHETER & HINDER MED 3D-PRINT AV BETONG. (Cited on page 9).

LKAB. (2018). SSAB, LKAB och Vattenfall planerar bygga världsunik pilotanläggning för fossilfritt stål. Retrieved February 14, 2018, from https://www.lkab.com. (Cited on page 8)

Mandal, S. K. (2015). *Steel Metallurgy: Properties, Specifications and Applications*. New York, Chicago, San Francisco, Athens, London, Madrid, Mexico City, Milan, New Delhi, Singapore, Sydney, Toronto: McGraw-Hill Education. Retrieved from http://accessengineeringlibrary.com.proxy.lib.chalmers.se/browse/steel-metallurgy-properties-specifications-and-applications%7B%5C#%7DfullDetails. (Cited on page 6)

Martini, K. (2015). Multiobjective Optimization of Structure and Visual Qualities. *Proceedings of the Symposium on Simulation for Architecture & Urban Design*, 182–188. Retrieved from http://dl.acm.org/citation.cfm?id=2873021.2873046. (Cited on pages 1, 12, 14, 65, 66)

McGuire, M. F. (2008). *Stainless Steels for Design Engineers*. A S M International. Retrieved from https://ebookcentral.proquest.com/lib/chalmers/detail.action?docID=3002326v. (Cited on page 6)

McNeel, R. (2018). What are NURBS? Retrieved February 7, 2018, from https://www.rhino3d.com/nurbs. (Cited on page 16)

Mehrjoo, M., Khaji, N., Moharrami, H., & Bahreininejad, A. (2008). Damage detection of truss bridge joints using Artificial Neural Networks. *Expert Systems with Applications*, *35*(3), 1122–1131. doi:10.1016/j.eswa.2007.08.008. (Cited on page 5)

Miljönytta. (2018). Stålindustrin: Stål formar en bättre framtid. Retrieved February 7, 2018, from http://miljonytta.se/branscher/stalindustrin/. (Cited on pages 6, 8)

Mitropoulou, C. C., Fourkiotis, Y., Lagaros, N. D., & Karlaftis, M. G. (2013). *Evolution Strategies-Based Metaheuristics in Structural Design Optimization* (First Edit). Elsevier Inc. doi:10.1016/B978-0-12-398364-0.00004-8. (Cited on pages 13, 14)

Nanakorn, P. & Nimtawat, A. (2013). *Layout Design of Beam-Slab Floors by a Genetic Algorithm* (First Edit). Elsevier Inc. doi:10.1016/B978-0-12-398364-0.00007-3. (Cited on pages 1, 10)

Potschka, A. (2014). *A Direct Method for Parabolic PDE Constrained Optimization Problems*. doi:10.1007/978-3-658-04476-3. arXiv: arXiv:1011.1669v3. (Cited on page 12)

Preisinger, C. (2016). PARAMETRIC STRUCTURAL MODELING User Manual for Karamba Version 1.2.2. *Karamba3D*, 142. Retrieved from https://www.karamba3d.com/news/new-manual/. (Cited on page 17)

Preisinger, C. & Bollinger-Grohmann-Schneider. (2018). Karamba 3D - Parametric engineering. Retrieved February 26, 2018, from https://www.karamba3d.com/. (Cited on page 17)

Rennie, R. (2016). *A Dictionary of Chemistry* (7th edition). Oxford University Press. Retrieved from http://www.oxfordreference.com.proxy.lib.chalmers.se/view/10.1093/acref/9780198722823.001.0001/acref-9780198722823-e-1468. (Cited on page 7)

Ronnenbrant, R. & Glans, L.-Å. (1996). *Broprojektering - En handbok* (First edit). Borlänge: Enheten för statlig väghållning. (Cited on page 6).

Rothwell, A. (2017). *Optimization Methods in Structural Design*. doi:10.1061/(ASCE)0733-9445(1983)109:10(2420). (Cited on pages 1, 10, 12, 65–68)

Ruiz-Geli, E. (2017). What is Rhino?: Rhinoceros 5 – Modeling Tools for Designers and Architects. Retrieved from http://www.visualarq.com/info/what-is-rhino/. (Cited on page 16)

Rutgersson, B. (2008). Kodförteckning och beskrivning av Brotyper: BaTMan Bro och Tunnel Managment. Borlänge: Trafikverket. doi:10.1007/s11947-009-0181-3. arXiv: arXiv:1011.1669v3. (Cited on page 4)

Sahab, M. G., Toropov, V. V., & Gandomi, A. H. (2013). *A Review on Traditional and Modern Structural Optimization: Problems and Techniques* (First Edit). Elsevier Inc. doi:10.1016/B978-0-12-398364-0.00002-4. (Cited on pages 10–13)

Sharafi, P., Hadi, M. N., & Teh, L. H. (2013). *Cost Optimization of Column Layout Design of Reinforced Concrete Buildings* (First Edit). Elsevier Inc. doi:10.1016/B978-0-12-398364-0.00006-1. (Cited on page 1)

Simon, D. (2013). Evolutionary Algorithm Variations. In *Evolutionary optimization algorithms*. (Cited on pages 13, 14).

Smith, A. E. & Coit, D. W. (1995). Penalty functions. *Handbook of Evolutionary Computation*, *97*(1), C5. (Cited on page 13).

StruSoft. (2018). FEM-Design FEM-Design applications. *StruSoft*. (Cited on page 20).

Tapabrata, R. (2018). CHAPTER 2 APPLICATIONS OF MULTI-OBJECTIVE EVOLUTIONARY ALGORITHMS IN ENGINEERING DESIGN. In *Applications of multi-objective evolutionary algorithms* (Chapter 2, Pages 29–52). Singapore: World Scientific Publishing Co Pte Ltd. (Cited on pages 14, 15).

TIBNOR. (2011). Konstruktionstabeller. *Tibnor*. (Cited on pages 21, 70).

Troitsky, M. S. (1994). *PLANNING and DESIGN of BRIDGES*. Montreal: John Wiley & Sons, Inc. (Cited on pages 4, 5).

United Nations. (2018). Sustainable development goals: Goal 11: Make cities inclusive, safe, resilient and sustainable. Retrieved from http://www.un.org/sustainabledevelopment/cities/page/2/. (Cited on pages 1, 7)

Wagner, D. B. (1996). *Iron and Steel in Ancient China* (second). Leiden: E.J Brill. (Cited on page 6).

Wahlström, B. (1971). *Bygg handbok för hus-, väg och vattenbyggnad Huvuddel. 1A, Allmänna grunder; avd. 11-15* (Tredje upp). Stockholm: Stockholm. (Cited on pages 36, 97).

World Steel Association. (2017). World Steel in Figures 2017. *World Steel Association*, 3–30. doi:https://www.worldsteel.org/en/dam/jcr:0474d208-9108-4927-ace8-4ac5445c5df8/World+Steel+in+Figures+2017.pdf. (Cited on page 8)

World Steel Association. (2018a). About steel. Retrieved February 8, 2018, from https://www.worldsteel.org/faq/about-steel---to-delete-if-ok.html. (Cited on page 7)

World Steel Association. (2018b). Sustainability indicators. Retrieved February 7, 2018, from https://www.worldsteel.org/steel-by-topic/sustainability/sustainability-indicators0.html. (Cited on page 7)

World Steel Association (WSA). (2015). Energy use in the steel industry. (51), 1–3. Retrieved from https://www.worldsteel.org/en/dam/jcr:f07b864c-908e-4229-9f92-669f1c3abf4c/fact%7B%5C_%7Denergy%7B%5C_%7D2016.pdf. (Cited on page 7)

Xylia, M., Silveira, S., Duerinck, J., & Meinke-Hubeny, F. (2017). Weighing regional scrap availability in global pathways for steel production processes. *Energy Efficiency*, 1–25. doi:10.1007/s12053-017-9583-7. (Cited on pages 7, 8)

Yang, X. S. (2010). *Engineering Optimization: An Introduction with Metaheuristic Applications*. doi:10.1002/9780470640425. (Cited on pages 1, 12)

Yang, X.-S. (2010). *Nature-inspired Metaheuristic Algorithms* (Second Edi). Cambridge, United Kingdom: Luniver Press. Retrieved from https://www.researchgate.net/publication/235979455%7B%5C_%7DNature-Inspired%7B%5C_%7DMetaheuristic%7B%5C_%7DAlgorithms. (Cited on pages 10–13)

Zietala, M., Durejko, T., Polański, M., Kunce, I., Płociński, T., Zieliński, W., … Bojar, Z. (2016). The microstructure, mechanical properties and corrosion resistance of 316 L stainless steel fabricated using laser engineered net shaping. doi:10.1016/j.msea.2016.09.028. (Cited on page 8)

A Gradient-free and gradient-based methods

Depending on the Taylor polynomial used to achieve an approximation of the solution of the objective functions, see Equations (3.1) to (3.4), the methods are called gradient-free, first-order or second-order methods, which are explained more below (Martini, 2015).

A.1 Gradient-free method

The gradient-free method, also called zero-order or derivative-free method, has as the name already indicates no need of Taylor's expansion to approximate the solution (Martini, 2015). The Hook and Jeeves method is an example of the gradient-free method and uses an initial point as the start of the search, shown as green in Figure A.1, for a maximum or minimum solution (Rothwell, 2017). From this point initial small steps (Δx) are taken in the directions of the design variable, which is represented in the vector shown in Equation (A.1) (Chinneck, 2001).

$$\mathbb{P}_0 = (\Delta x_1, \Delta x_2, \cdots, \Delta x_n) \tag{A.1}$$

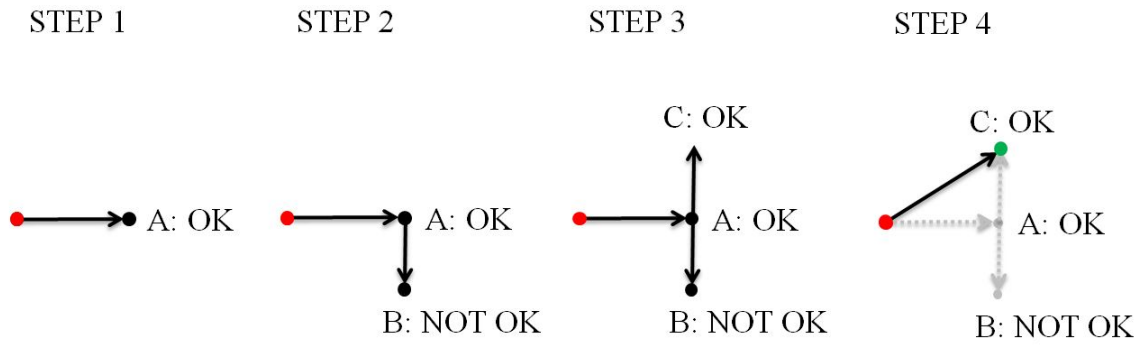

Figure A.1: Gradient-free method search process, based on (Chinneck, 2001).

After each "move", the new values of the objective functions are analyzed and compared with the value from just before, see Figure A.1 (Chinneck, 2001). In the case of a minimization problem, where a reduction of the objective function is sought-after, the function value is said to be improved if it decreases. If so, this becomes the new starting point for the next step. If the function value has increased, in the case of a minimization problem, the step is neglected and the next step is taken into another direction. In case of a maximization problem it is the other way around. To get close to the local minimum or maximum, the step size is reduced at each iteration. To accelerate the process the Hooke and Jeeves method uses the search direction from the starting point $x^{(0)}$ to first point $x^{(1)}$, which implies that the next point $x^{(2)}$ is calculated using movement form $x^{(0)}$ through $x^{(1)}$, as can be seen in Equation (A.2).

$$x^{(2)} = 2x^{(1)} - x^{(0)} \tag{A.2}$$

If the function values have been improved in this direction between $x^{(0)}$ and $x^{(1)}$, it can be assumed that the local optimum lies in that direction. These methods have the benefit to be simple and robust, but are impractical for more complex problems.

A.2 Gradient-based method

Gradient-based methods are dependent on the expansion of the Taylor series and need at least a first-order polynomial to achieve an approximation of the solution (Martini, 2015).

A.2.1 First-order methods

In the first-order method the solution, which is a linear approximation of the objective function, is found with the first-order Taylor polynomial (Martini, 2015). One example of the first-order method is the steepest decent method, which can be used to compute more advanced numerical problems, than with the gradient-free methods (Rothwell, 2017). The derivative function, being a linear approximation, can indicate in which direction the function decreases the quickest, hence the name "steepest descent method". The formulation of the derivative of the objective function can be seen in Equation (A.3) and can be elaborated into Equation (A.4). $\delta f(x)$ represents the reduction, which needs to be as large as possible to achieve the fastest search direction, which results in a quick convergence towards a solution. Equation (A.4) can be rewritten into Equation (A.5), with the substitution into the derivative functions f_1, f_2 and so forth and the defined search directions, which is described in Equation (A.6).

$$\frac{df(x)}{d\mathbb{x}} = \nabla f(x) = \left[\frac{df(x)}{dx_1}, \quad \frac{df(x)}{dx_2}, \quad \cdots, \quad \frac{df(x)}{dx_n}\right] \tag{A.3}$$

$$\delta f(x) = \frac{df(x)}{dx_1}\delta x_1 + \frac{df(x)}{dx_2}\delta x_2 + \cdots + \frac{df(x)}{dx_n}\delta x_n \tag{A.4}$$

$$= f_1\, s_1 + f_2\, s_2 + \cdots + f_n\, s_n = \sum_{i=1}^{n} f_i s_i \tag{A.5}$$

$$where\ s_1 = \delta x_1,\ s_2 = \delta x_2,\ \cdots,\ s_n = \delta x_n \tag{A.6}$$

As the maximum reduction of f(x) is sought, in the case of a minimization problem, s_i is to be solved and a negative derivative of the objective function defined. Equation (A.7) is the final equation, which describes the search direction of the steepest descent method, where $\mathbb{s}$ is a vector with all the search directions, see Equation (A.8).

$$\mathbb{s} = -\nabla \mathbb{f}(\mathbb{x}) \tag{A.7}$$

$$where\ \mathbb{s} = \left[s_1, s_2, ..., s_n\right] \tag{A.8}$$

Once a minimum point is found along the direction of the derivative line, see blue lines in Figure A.2, the derivative at the minimum point, in the case of a minimization problem, is analyzed and a new search direction found. This process is repeated until a minimum of the objective function is found, which represents point D in Figure A.2. The steepest decent method is an iterative method

and takes several iterations to get a converging result (linear convergence). Figure A.2 shows an example of the iterative process, with the starting point at A, continuing to B and finally ending up in D, which is the minimum of the objective function. The circular lines represent the objective functions.

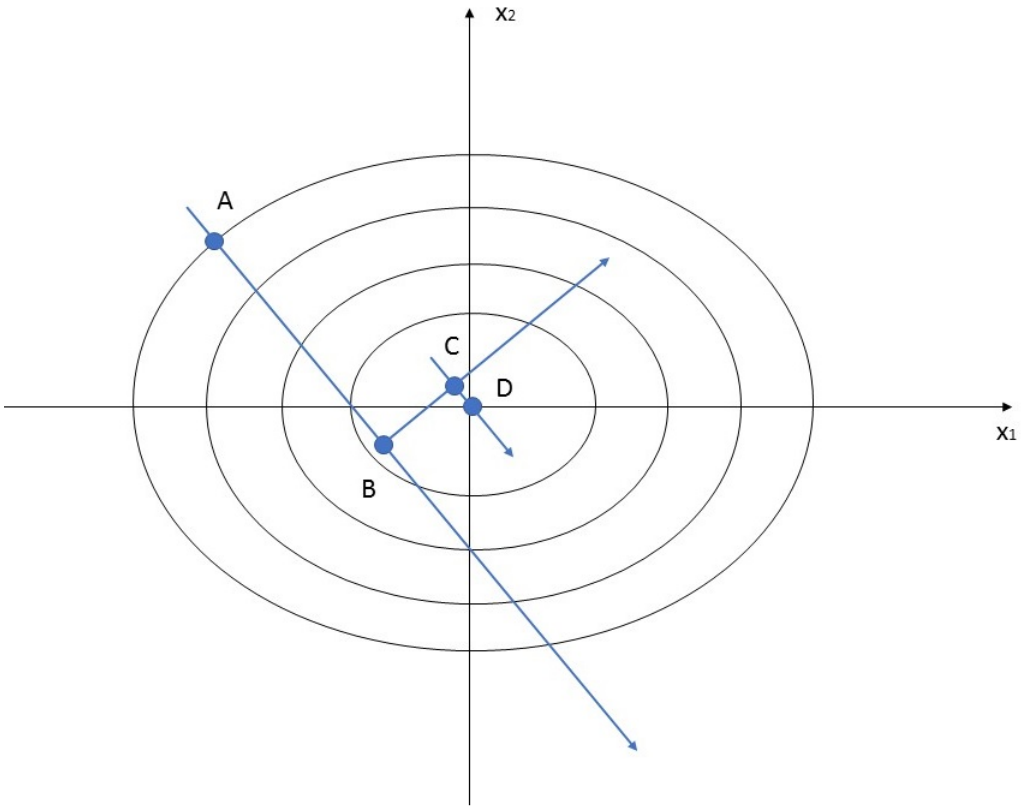

Figure A.2: Example of a search process used in the steepest decent method, based on (Rothwell, 2017).

A.2.2 Second-order methods

There are also second-order methods, which use the second-order derivatives to improve the search direction at each iteration (Rothwell, 2017). The Quasi-newton method is one example of such method and it also continuously uses the previous iterations to improve the search direction for the next iteration. The Quasi-Newton method gets faster convergence than the steepest descent method since the second-order derivatives, see Equation (A.9), are used (quadratic convergence).

$$H(x) = \begin{bmatrix} \frac{\partial^2 f}{\partial x_1^2} & \frac{\partial^2 f}{\partial x_1 \partial x_2} & \cdots & \frac{\partial^2 f}{\partial x_1 \partial x_n} \\ \frac{\partial^2 f}{\partial x_2^2} & \frac{\partial^2 f}{\partial x_2^2} & \cdots & \frac{\partial^2 f}{\partial x_2 \partial x_n} \\ \vdots & \vdots & \ddots & \vdots \\ \frac{\partial^2 f}{\partial x_n \partial x_1} & \frac{\partial d^2 f}{\partial x_n \partial x_2} & \cdots & \frac{\partial^2 f}{\partial x_n^2} \end{bmatrix} \tag{A.9}$$

In Equation (A.10) the position of a point $\mathbb{x}'$ can be calculated using the "Hessian" matrix $\mathbb{H}$ which contains the second-order derivatives of the objective function (Rothwell, 2017). When moving from a point $\mathbb{x}$ to another point $\mathbb{x}'$ the gradient will change and the Hessian-matrix will be evaluated at each point. Equation (A.10) can be used to calculate the minimum point if the gradient, $\nabla f(\mathbb{x})$, is zero.

$$\mathbb{x}' = \mathbb{x} - \mathbb{H}(\mathbb{x})^{-1}\nabla f(\mathbb{x}) \tag{A.10}$$

$$\mathbb{s} = -\mathbb{B}\nabla f(\mathbb{x}) \tag{A.11}$$

$$\mathbb{H}_{k+1} = \mathbb{B}_{k+1}^{-1} \tag{A.12}$$

The new search direction is stated in Equation (A.11) and is continuously updated with the result obtained from the previous iteration (Rothwell, 2017). The subscripts (k+1) and (k) are referencing to the next iteration and the current iteration. One way to update the $\mathbb{B}$ matrix is the Broyden-Fletcher-Goldfarb-Shannon (BFGS)-method, see Equation (A.13). Where the new $\mathbb{B}$-matrix is updated using the results from the previous iterations. For the first iteration $\mathbb{B} = \mathbb{I}$ which is the unit-matrix.

$$\mathbb{B}^{k+1} = \mathbb{B}^{k} + \left(1 + \frac{\mathbb{y}^T\mathbb{B}^{(\mathbb{k})}\mathbb{y}}{\mathbb{p}^T\mathbb{y}}\right)\frac{\mathbb{p}\mathbb{p}^{\mathbb{T}}}{\mathbb{p}^T\mathbb{y}} - \frac{\mathbb{p}\mathbb{y}^{\mathbb{T}}\mathbb{B}^{(K)}}{\mathbb{p}^T\mathbb{y}} - \frac{\mathbb{B}^{(k)}\mathbb{y}\mathbb{p}^T}{\mathbb{p}^T\mathbb{y}} \tag{A.13}$$

Equation (A.14) are the gradient differences which are used to estimate the new $\mathbb{B}$-matrix and Equation (A.15) is the position difference (Rothwell, 2017).

$$\mathbb{y} = \nabla f(\mathbb{x})^{(k+1)} - \nabla f(\mathbb{x})^{(k)} \tag{A.14}$$

$$\mathbb{p} = \mathbb{x}^{(k+1)} - \mathbb{x}^{(k)} \tag{A.15}$$

B Plans of the case study over Genevadsån

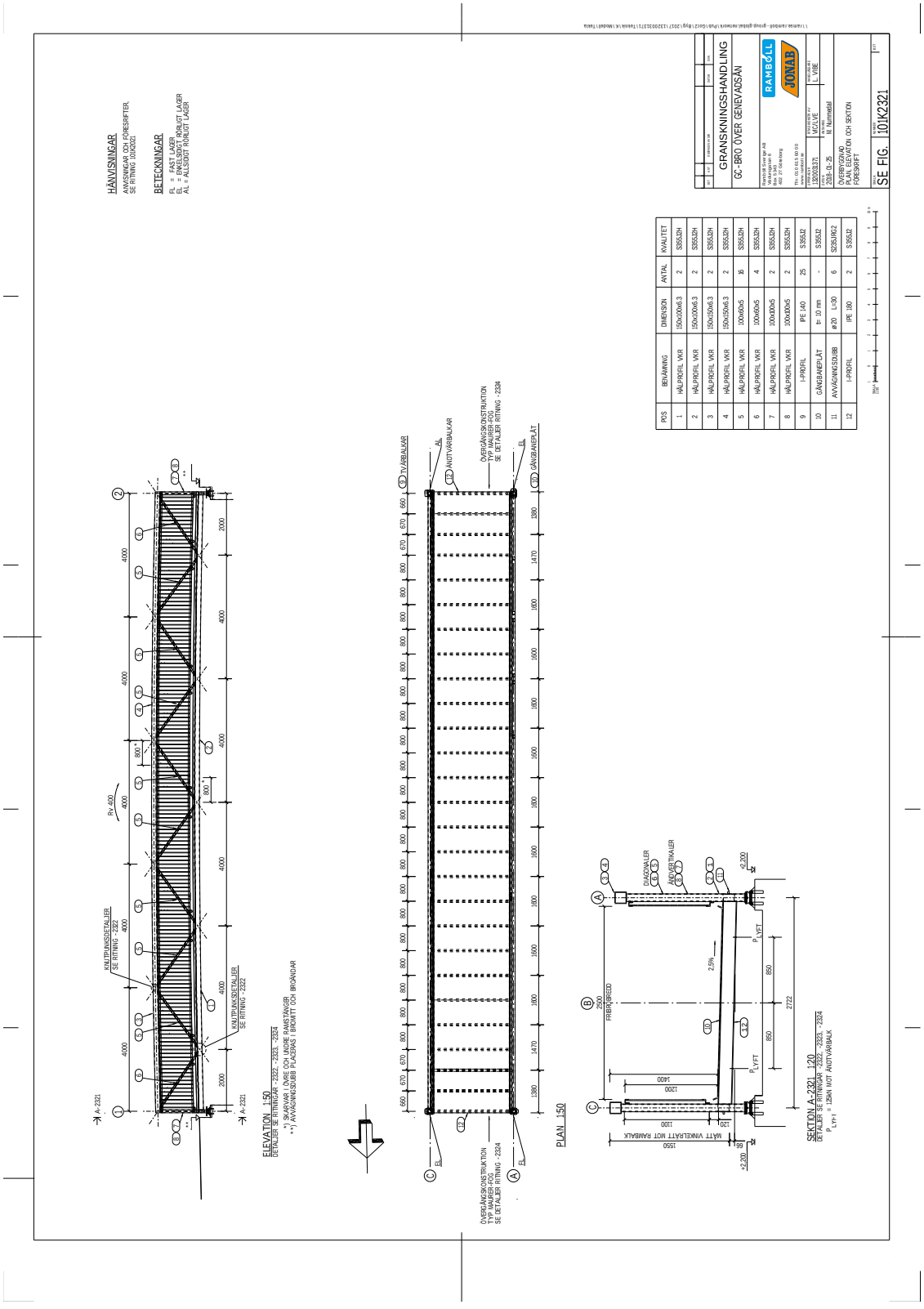

Figure B.1: Used plans from the case study over Genevadsån.

C Cross-sections inserted in Karamba 3D

In this appendix first the VKR, then the KCKR and at last the IPE profiles, which were implemented into Karamba 3D, are presented. The values are taken from a construction table based on SS-EN10210 (TIBNOR, 2011) and the imperfection values are calculated according to EN 1993-1-1 chapter 6.3.1.

VKR-profiles

Contry	Family	Name	Shape	Depth of section h mm	Thickness of web t_web mm	Upper width of section b_upper mm	Thickness of upper flange t_upper mm	Position of centroid zs cm	Area of section A cm2	Effective shear area Vy Ay cm2	Effective shear area Vz Az cm2	Second moment of area (strong axis Iy cm4	Elastic modulus upper (strong axis) Wy cm3	Plastic modulus (Strong axis) Wply cm3	Radius of gyration (strong axis) i_y cm	Second moment of area (weak axis) Iz cm4	Elastic modulus (weak axis) Wz cm3	Plastic modulus (weak axis) Wplz cm3	Radius of gyration (weak axis) i_z cm	Torsional constant inertia It cm4	Elastic modulus torsion Wt cm3	Warping factor Cw cm6	Imperfection value for buckling (strong axis) alpha_y -	Imperfection value for buckling (weak axis) alpha_z -	Imperfection value for lateral torsional buckling alpha_LT -	Type of product (*) Product -
Sweden	VKR	VKR100x100x4	[]	100	4	100	4	5	15,2	7,6	7,6	232	46,4	54,4	3,91	232	46,4	54,4	3,91	361	68,2	0	0,21	0,21	0,76	3
Sweden	VKR	VKR100x100x5	[]	100	5	100	5	5	18,7	9,35	9,35	279	55,9	66,4	3,86	279	55,9	66,4	3,86	439	81,8	0	0,21	0,21	0,76	3
Sweden	VKR	VKR100x100x6,3	[]	100	6,3	100	6,3	5	23,2	11,6	11,6	336	67,1	80,9	3,8	336	67,1	80,9	3,8	534	97,8	0	0,21	0,21	0,76	3
Sweden	VKR	VKR100x100x8	[]	100	8	100	8	5	28,8	14,4	14,4	400	79,9	99,2	3,73	400	79,9	99,2	3,73	646	116	0	0,21	0,21	0,76	3
Sweden	VKR	VKR100x100x10	[]	100	10	100	10	5	34,9	17,45	17,45	462	92,4	116	3,64	462	92,4	116	3,64	761	133	0	0,21	0,21	0,76	3
Sweden	VKR	VKR120x120x4,5	[]	120	4,5	120	4,5	6	20,5	10,25	10,25	452	75,3	88,2	4,7	452	75,3	88,2	4,7	707	112	0	0,21	0,21	0,76	3
Sweden	VKR	VKR120x120x5	[]	120	5	120	5	6	22,9	11,45	11,45	503	83,8	98,4	4,68	503	83,8	98,4	4,68	777	122	0	0,21	0,21	0,76	3
Sweden	VKR	VKR120x120x6,3	[]	120	6,3	120	6,3	6	28,5	14,25	14,25	610	102	121	4,62	610	102	121	4,62	950	147	0	0,21	0,21	0,76	3
Sweden	VKR	VKR120x120x8	[]	120	8	120	8	6	35,5	17,75	17,75	738	123	149	4,55	738	123	149	4,55	1160	176	0	0,21	0,21	0,76	3
Sweden	VKR	VKR120x120x10	[]	120	10	120	10	6	43,5	21,75	21,75	870	145	178	4,46	870	145	178	4,46	1382	206	0	0,21	0,21	0,76	3
Sweden	VKR	VKR140x140x5	[]	140	5	140	5	7	26,9	13,45	13,45	814	116	136	5,5	814	116	136	5,5	1253	170	0	0,21	0,21	0,76	3
Sweden	VKR	VKR140x140x6,3	[]	140	6,3	140	6,3	7	33,5	16,75	16,75	994	142	168	5,44	994	142	168	5,44	1540	206	0	0,21	0,21	0,76	3
Sweden	VKR	VKR140x140x8	[]	140	8	140	8	7	41,9	20,95	20,95	1212	173	207	5,36	1212	173	207	5,36	1892	249	0	0,21	0,21	0,76	3
Sweden	VKR	VKR140x140x10	[]	140	10	140	10	7	51,5	25,75	25,75	1441	206	250	5,27	1441	206	250	5,27	2272	294	0	0,21	0,21	0,76	3
Sweden	VKR	VKR150x150x5	[]	150	5	150	5	7,5	28,9	14,45	14,45	1009	135	157	5,9	1009	135	157	5,9	1550	197	0	0,21	0,21	0,76	3
Sweden	VKR	VKR150x150x6,3	[]	150	6,3	150	6,3	7,5	36	18	18	1236	165	194	5,85	1236	165	194	5,85	1909	240	0	0,21	0,21	0,76	3
Sweden	VKR	VKR150x150x8	[]	150	8	150	8	7,5	45,1	22,55	22,55	1510	201	240	5,77	1510	201	240	5,77	2351	291	0	0,21	0,21	0,76	3
Sweden	VKR	VKR150x150x10	[]	150	10	150	10	7,5	55,5	27,75	27,75	1803	240	290	5,68	1803	240	290	5,68	2832	344	0	0,21	0,21	0,76	3
Sweden	VKR	VKR160x160x5,6	[]	160	5,6	160	5,6	8	33,8	16,9	16,9	1330	166	194	6,26	1330	166	194	6,26	2333	275	0	0,21	0,21	0,76	3
Sweden	VKR	VKR160x160x6,3	[]	160	6,3	160	6,3	8	38,3	19,15	19,15	1499	187	220	6,18	1499	187	220	6,18	2880	335	0	0,21	0,21	0,76	3
Sweden	VKR	VKR160x160x8	[]	160	8	160	8	8	48	24	24	1831	229	272	6,09	1831	229	272	6,09	3478	398	0	0,21	0,21	0,76	3
Sweden	VKR	VKR160x160x10	[]	160	10	160	10	8	58,9	29,45	29,45	2186	273	329	7,07	2186	273	329	7,07	3361	355	0	0,21	0,21	0,76	3
Sweden	VKR	VKR180x180x6,3	[]	180	6,3	180	6,3	9	43,6	21,8	21,8	2186	243	283	7	2186	243	283	7	4162	434	0	0,21	0,21	0,76	3
Sweden	VKR	VKR180x180x8	[]	180	8	180	8	9	54,7	27,35	27,35	2689	299	352	6,91	2689	299	352	6,91	5048	518	0	0,21	0,21	0,76	3
Sweden	VKR	VKR180x180x10	[]	180	10	180	10	9	67,5	33,75	33,75	3237	360	429	7,89	3237	360	429	7,89	4653	444	0	0,21	0,21	0,76	3
Sweden	VKR	VKR200x200x6,3	[]	200	6,3	200	6,3	10	48,6	24,3	24,3	3033	303	353	7,81	3033	303	353	7,81	5778	545	0	0,21	0,21	0,76	3
Sweden	VKR	VKR200x200x8	[]	200	8	200	8	10	61,1	30,55	30,55	3744	374	439	7,72	3744	374	439	7,72	7031	655	0	0,21	0,21	0,76	3
Sweden	VKR	VKR200x200x10	[]	200	10	200	10	10	75,5	37,75	37,75	4525	452	536	7,61	4525	452	536	7,61	8491	778	0	0,21	0,21	0,76	3
Sweden	VKR	VKR200x200x12,5	[]	200	12,5	200	12,5	10	93	46,5	46,5	5419	542	651	7,46	5419	542	651	7,46	10340	927	0	0,21	0,21	0,76	3
Sweden	VKR	VKR200x200x16	[]	200	16	200	16	10	117	58,5	58,5	6524	652	799	8,71	6524	652	799	8,71	6240	544	0	0,21	0,21	0,76	3
Sweden	VKR	VKR220x220x6,3	[]	220	6,3	220	6,3	11	52,8	26,4	26,4	3980	362	421	8,54	3980	362	421	8,54	9473	807	0	0,21	0,21	0,76	3
Sweden	VKR	VKR220x220x10	[]	220	10	220	10	11	81,4	40,7	40,7	5890	535	634	9,93	5890	535	634	9,93	9238	712	0	0,21	0,21	0,76	3
Sweden	VKR	VKR250x250x6,3	[]	250	6,3	250	6,3	12,5	61,2	30,6	30,6	6049	484	559	9,86	6049	484	559	9,86	11525	880	0	0,21	0,21	0,76	3
Sweden	VKR	VKR250x250x8	[]	250	8	250	8	12,5	77,1	38,55	38,55	7510	601	699	9,77	7510	601	699	9,77	14106	1065	0	0,21	0,21	0,76	3
Sweden	VKR	VKR250x250x10	[]	250	10	250	10	12,5	95,5	47,75	47,75	9141	731	858	9,66	9141	731	858	9,66	17164	1279	0	0,21	0,21	0,76	3
Sweden	VKR	VKR250x250x12,5	[]	250	12,5	250	12,5	12,5	118	59	59	11050	884	1048	9,5	11050	884	1048	9,5	21138	1546	0	0,21	0,21	0,76	3
Sweden	VKR	VKR250x250x16	[]	250	16	250	16	12,5	149	74,5	74,5	13480	1078	1298	11,8	13480	1078	1298	11,8	24807	1575	0	0,21	0,21	0,76	3
Sweden	VKR	VKR300x300x10	[]	300	10	300	10	15	116	58	58	16150	1077	1254	11,7	16150	1077	1254	11,7	30333	1904	0	0,21	0,21	0,76	3
Sweden	VKR	VKR300x300x12,5	[]	300	12,5	300	12,5	15	143	71,5	71,5	19630	1309	1538	11,5	19630	1309	1538	11,5	37622	2325	0	0,21	0,21	0,76	3
Sweden	VKR	VKR300x300x16	[]	300	16	300	16	15	181	90,5	90,5	24160	1610	1916	13,9	24160	1610	1916	13,9	39886	2185	0	0,21	0,21	0,76	3
Sweden	VKR	VKR350x350x10	[]	350	10	350	10	17,5	136	68	68	26050	1489	1725	13,7	26050	1489	1725	13,7	48934	2654	0	0,21	0,21	0,76	3
Sweden	VKR	VKR350x350x12,5	[]	350	12,5	350	12,5	17,5	168	84	84	31810	1817	2122	13,6	31810	1817	2122	13,6	60990	3264	0	0,21	0,21	0,76	3
Sweden	VKR	VKR400x400x10	[]	400	10	400	10	20	156	78	78	39350	1968	2272	15,9	39350	1968	2272	15,9	60092	2895	0	0,21	0,21	0,76	3
Sweden	VKR	VKR400x400x12,5	[]	400	12,5	400	12,5	20	193	96,5	96,5	48190	2409	2800	15,8	48190	2409	2800	15,8	73906	3530	0	0,21	0,21	0,76	3
Sweden	VKR	VKR400x400x16	[]	400	16	400	16	20	245	122,5	122,5	59905	2995	3514	15,6	59905	2995	3514	15,6	92442	4362	0	0,21	0,21	0,76	3
Sweden	VKR	VKR100x60x3,6	[]	100	3,6	60	3,6	5	10,9	4,1	6,8	145	28,9	35,6	3,58	64,4	21,6	24,9	2,44	142	35,6	0	0,21	0,21	0,76	3
Sweden	VKR	VKR100x60x4	[]	100	4	60	4	5	12	4,5	7,5	158	31,6	39,1	3,53	70,5	23,5	27,3	2,43	156	38,7	0	0,21	0,21	0,76	3
Sweden	VKR	VKR100x60x5	[]	100	5	60	5	5	14,7	5,5	9,2	189	37,8	47,4	3,48	83,6	27,9	32,9	2,38	188	45,9	0	0,21	0,21	0,76	3
Sweden	VKR	VKR100x60x5,6	[]	100	5,6	60	5,6	5	16,3	6,1	10,2	206	41,2	52	3,45	90,6	30,2	36,1	2,36	205	49,7	0	0,21	0,21	0,76	3
Sweden	VKR	VKR100x60x6,3	[]	100	6,3	60	6,3	5	18,1	6,8	11,3	225	45	57,3	3,42	98,1	32,7	39,5	2,33	224	53,8	0	0,21	0,21	0,76	3
Sweden	VKR	VKR120x60x3,6	[]	120	3,6	60	3,6	6	12,3	4,1	8,2	227	37,9	47,2	3,33	76,3	25,4	28,9	2,49	183	43,3	0	0,21	0,21	0,76	3
Sweden	VKR	VKR120x60x4	[]	120	4	60	4	6	13,6	4,5	9,1	249	41,5	51,9	3,65	83,1	27,7	31,7	2,47	201	47,1	0	0,21	0,21	0,76	3
Sweden	VKR	VKR120x60x5	[]	120	5	60	5	6	16,7	5,6	11,1	299	49,9	63,1	3,63	98,9	32,9	38,4	2,43	242	56	0	0,21	0,21	0,76	3
Sweden	VKR	VKR120x60x6,3	[]	120	6,3	60	6,3	6	20,7	6,9	13,8	358	59,7	76,7	3,58	116	38,8	46,3	2,37	290	65,9	0	0,21	0,21	0,76	3
Sweden	VKR	VKR120x80x4	[]	120	4	80	4	6	15,2	6,08	9,1	303	50,4	61,2	3,55	161	40,2	46,1	3,25	330	65	0	0,21	0,21	0,76	3
Sweden	VKR	VKR120x80x5	[]	120	5	80	5	6	18,7	7,48	11,2	365	60,9	74,6	3,52	193	48,2	56,1	3,21	401	77,9	0	0,21	0,21	0,76	3
Sweden	VKR	VKR120x80x6,3	[]	120	6,3	80	6,3	6	23,2	9,28	13,9	440	73,3	91	4,3	230	57,6	68,2	3,15	487	92,9	0	0,21	0,21	0,76	3
Sweden	VKR	VKR120x80x8	[]	120	8	80	8	6	28,8	11,52	17,3	525	87,5	111	4,28	273	68,1	82,6	3,08	587	110	0	0,21	0,21	0,76	3
Sweden	VKR	VKR140x70x4	[]	140	4	70	4	7	16	5,3	10,7	404	57,7	71,7	4,23	136	38,8	44	2,91	325	66	0	0,21	0,21	0,76	3
Sweden	VKR	VKR140x70x5	[]	140	5	70	5	7	19,7	6,6	13,1	488	69,8	87,6	4,16	163	46,5	53,5	2,87	394	79	0	0,21	0,21	0,76	3
Sweden	VKR	VKR140x70x6,3	[]	140	6,3	70	6,3	7	24,4	8,1	16,3	589	84,2	107	4,46	194	55,3	65	2,81	477	94	0	0,21	0,21	0,76	3
Sweden	VKR	VKR140x80x4	[]	140	4	80	4	7	16,8	6,1	10,7	441	62,9	77,1	4,42	184	46	52,2	3,31	411	76,5	0	0,21	0,21	0,76	3
Sweden	VKR	VKR140x80x6,3	[]	140	6,3	80	6,3	7	25,7	9,3	16,4	646	92,3	115	4,36	265	66,2	77,5	3,21	607	110	0	0,21	0,21	0,76	3
Sweden	VKR	VKR150x100x5	[]	150	5	100	5	7,5	23,7	9,48	14,2	739	98,5	119	4,27	392	78,5	90,1	4,07	807	127	0	0,21	0,21	0,76	3
Sweden	VKR	VKR150x100x6,3	[]	150	6,3	100	6,3	7,5	29,5	11,8	17,7	898	120	147	5,5	474	94,8	110	4,01	986	153	0	0,21	0,21	0,76	3
Sweden	VKR	VKR150x100x8	[]	150	8	100	8	7,5	36,8	14,72	22,1	1087	145	180	4,98	569	114	135	3,94	1203	183	0	0,21	0,21	0,76	3
Sweden	VKR	VKR150x100x10	[]	150	10	100	10	7,5	44,9	17,96	26,9	1282	171	216	4,91	665	133	161	3,85	1432	214	0	0,21	0,21	0,76	3
Sweden	VKR	VKR160x80x4	[]	160	4	80	4	8	18,4	6,1	12,3	612	76,5	94,7	5,77	207	51,7	58,3	3,35	493	88,1	0	0,21	0,21	0,76	3

(*) 0:cold formed; 1: hot finished; 2: welded; 3: rolled;

VKR-profiles

Contry	Family	Name	Shape	Depth of section h	Thickness of web t_web	Upper width of section b_upper	Thickness of upper flange t_upper	Position of centroid zs	Area of section A	Effective shear area Vy Ay	Effective shear area Vz Az	Second moment of area (strong axis Iy	Elastic modulus upper (strong axis) Wy	Plastic modulus (Strong axis) Wply	Radius of gyration (strong axis) i_y	Second moment of area (weak axis) Iz	Elastic modulus (weak axis) Wz	Plastic modulus (weak axis) Wplz	Radius of gyration (weak axis) i_z	Torsional constant inertia It	Elastic modulus torsion Wt	Warping factor Cw	Imperfection value for buckling (strong axis) alpha_y	Imperfection value for buckling (weak axis) alpha_z	Imperfection value for lateral torsional buckling alpha_LT	Type of product (*) Product
				mm	mm	mm	mm	cm	cm2	cm2	cm2	cm4	cm3	cm3	cm	cm4	cm3	cm3	cm	cm4	cm3	cm6	-	-	-	-
Sweden	VKR	VKR160x80x5	[]	160	5	80	5	8	22,7	7,6	15,1	744	93	116	5,72	249	62,3	71,1	3,31	600	106	0	0,21	0,21	0,76	3
Sweden	VKR	VKR160x80x6,3	[]	160	6,3	80	6,3	8	28,2	9,4	18,8	903	113	142	5,66	299	74,8	86,8	3,26	730	127	0	0,21	0,21	0,76	3
Sweden	VKR	VKR160x80x8	[]	160	8	80	8	8	35,2	11,7	23,5	1091	136	175	5,57	356	89	106	3,18	883	151	0	0,21	0,21	0,76	3
Sweden	VKR	VKR160x80x10	[]	160	10	80	10	8	42,9	14,3	28,6	1284	161	209	5,47	411	103	125	3,1	1041	175	0	0,21	0,21	0,76	3
Sweden	VKR	VKR160x90x5	[]	160	5	90	5	8	23,7	8,532	15,2	804	101	124	5,82	326	72,5	82,7	3,71	738	121	0	0,21	0,21	0,76	3
Sweden	VKR	VKR160x90x7,1	[]	160	7,1	90	7,1	8	32,9	11,844	21,1	1080	135	169	5,72	431	95,7	112	3,62	995	160	0	0,21	0,21	0,76	3
Sweden	VKR	VKR160x90x8	[]	160	8	90	8	8	36,8	13,248	23,6	1180	148	187	5,68	470	105	124	3,58	1100	174	0	0,21	0,21	0,76	3
Sweden	VKR	VKR180x100x5,6	[]	180	5,6	100	5,6	9	29,8	10,6	19,2	1270	141	174	6,54	506	101	115	4,12	1150	169	0	0,21	0,21	0,76	3
Sweden	VKR	VKR180x100x6,3	[]	180	6,3	100	6,3	9	33,3	11,9	21,4	1407	156	194	6,5	557	111	128	4,09	1277	186	0	0,21	0,21	0,76	3
Sweden	VKR	VKR180x100x8	[]	180	8	100	8	9	41,6	14,9	26,7	1713	190	239	6,42	671	134	157	4,02	1560	224	0	0,21	0,21	0,76	3
Sweden	VKR	VKR180x100x10	[]	180	10	100	10	9	50,9	18,2	32,7	2036	226	288	6,32	787	157	188	3,93	1862	263	0	0,21	0,21	0,76	3
Sweden	VKR	VKR200x100x5	[]	200	5	100	5	10	28,7	9,6	19,1	1495	149	185	7,21	505	101	114	4,19	1204	172	0	0,21	0,21	0,76	3
Sweden	VKR	VKR200x100x6,3	[]	200	6,3	100	6,3	10	35,8	11,9	23,9	1829	183	228	7,15	613	123	140	4,14	1475	208	0	0,21	0,21	0,76	3
Sweden	VKR	VKR200x100x8	[]	200	8	100	8	10	44,8	14,9	29,9	2234	223	282	7,06	739	148	172	4,06	1804	251	0	0,21	0,21	0,76	3
Sweden	VKR	VKR200x100x10	[]	200	10	100	10	10	54,9	18,3	36,6	2664	266	341	6,96	869	174	206	3,98	2156	295	0	0,21	0,21	0,76	3
Sweden	VKR	VKR200x100x12,5	[]	200	12,5	100	12,5	10	67,1	22,4	44,7	3136	314	408	6,84	1004	201	245	3,87	2541	341	0	0,21	0,21	0,76	3
Sweden	VKR	VKR200x120x6,3	[]	200	6,3	100	6,3	10	38,3	12,8	25,5	2065	207	253	7,34	929	155	177	4,92	2028	255	0	0,21	0,21	0,76	3
Sweden	VKR	VKR200x120x8	[]	200	8	120	8	10	48	18	30	2529	253	313	7,26	1128	188	218	4,85	2495	310	0	0,21	0,21	0,76	3
Sweden	VKR	VKR200x120x10	[]	200	10	120	10	10	58,9	22,1	36,8	3026	303	379	7,17	1337	223	263	4,76	3001	367	0	0,21	0,21	0,76	3
Sweden	VKR	VKR220x120x6,3	[]	220	6,3	120	6,3	11	40,8	14,4	26,4	2610	237	292	8	1010	168	191	4,98	2320	283	0	0,21	0,21	0,76	3
Sweden	VKR	VKR220x120x8	[]	220	8	120	8	11	51,2	18,1	33,1	3200	291	362	7,91	1230	205	236	4,9	2850	343	0	0,21	0,21	0,76	3
Sweden	VKR	VKR220x120x10	[]	220	10	120	10	11	62,9	22,2	40,7	3840	349	440	7,82	1460	243	285	4,81	3430	407	0	0,21	0,21	0,76	3
Sweden	VKR	VKR250x150x6,3	[]	250	6,3	150	6,3	12,5	48,4	18,15	30,3	4143	331	402	9,25	1874	250	283	6,22	4054	413	0	0,21	0,21	0,76	3
Sweden	VKR	VKR250x150x8	[]	250	8	150	8	12,5	60,8	22,8	38	5111	409	501	9,17	2298	306	350	6,15	5021	506	0	0,21	0,21	0,76	3
Sweden	VKR	VKR250x150x10	[]	250	10	150	10	12,5	74,9	28,1	46,8	6174	494	611	9,08	2755	367	426	6,06	6090	605	0	0,21	0,21	0,76	3
Sweden	VKR	VKR250x150x12,5	[]	250	12,5	150	12,5	12,5	92,1	34,5	57,6	7387	591	740	8,96	3265	435	514	5,96	7326	717	0	0,21	0,21	0,76	3
Sweden	VKR	VKR260x140x6,3	[]	260	6,3	140	6,3	13	48,4	16,94	31,5	4350	335	411	9,49	1660	237	267	5,86	3800	399	0	0,21	0,21	0,76	3
Sweden	VKR	VKR260x140x8	[]	260	8	140	8	13	60,8	21,28	39,5	5370	413	511	9,4	2030	290	331	5,78	4700	488	0	0,21	0,21	0,76	3
Sweden	VKR	VKR300x200x6,3	[]	300	6,3	200	6,3	15	61	24,4	36,6	7829	522	624	11,3	4193	419	472	8,29	8476	681	0	0,21	0,21	0,76	3
Sweden	VKR	VKR300x200x8	[]	300	8	200	8	15	76,8	30,72	46,1	9717	648	779	11,3	5184	518	589	8,22	10562	840	0	0,21	0,21	0,76	3
Sweden	VKR	VKR300x200x10	[]	300	10	200	10	15	94,9	37,96	56,9	11819	788	956	11,2	6278	628	721	8,13	12908	1015	0	0,21	0,21	0,76	3
Sweden	VKR	VKR300x200x12,5	[]	300	12,5	200	12,5	15	117	46,8	70,2	14273	952	1165	11	7537	754	877	8,02	15677	1217	0	0,21	0,21	0,76	3
Sweden	VKR	VKR300x200x16	[]	300	16	200	16	15	147	58,8	88,2	17390	1159	1441	10,9	9109	911	1080	7,87	19252	1468	0	0,21	0,21	0,76	3
Sweden	VKR	VKR400x200x10	[]	400	10	200	10	20	115	38,3	76,7	23914	1196	1480	14,4	8084	808	911	8,38	19259	1376	0	0,21	0,21	0,76	3
Sweden	VKR	VKR400x200x12,5	[]	400	12,5	200	12,5	20	142	47,3	94,7	29063	1453	1813	14,3	9738	974	1111	8,28	23438	1656	0	0,21	0,21	0,76	3
Sweden	VKR	VKR400x200x16	[]	400	16	200	16	20	179	59,7	119,3	35738	1787	2256	14,1	11824	1182	1374	8,13	28871	2010	0	0,21	0,21	0,76	3
Sweden	VKR	VKR450x250x10	[]	450	10	250	10	22,5	135	48,2	86,8	36895	1640	2000	16,5	14819	1185	1331	10,5	33284	1986	0	0,21	0,21	0,76	3
Sweden	VKR	VKR450x250x12,5	[]	450	12,5	250	12,5	22,5	167	59,6	107,4	45026	2001	2458	16,4	17973	1438	1631	10,4	40719	2406	0	0,21	0,21	0,76	3
Sweden	VKR	VKR450x250x16	[]	450	16	250	16	22,5	211	75,35	135,6	55705	2476	3070	16,2	22041	1763	2029	10,2	50545	2947	0	0,21	0,21	0,76	3

(*) 0:cold formed; 1: hot finished; 2: welded; 3: rolled;

Circular cross sections (KCKR)

Contry	Family	Name	Shape	Depth of section h mm	Thickness of web t_web mm	Position of centroid zs cm	Area of section A cm2	Effective shear area Vy Ay cm2	Effective shear area Vz Az cm2	Second moment of area (strong axis Iy cm4	Elastic modulus upper (strong axis) Wy cm3	Plastic modulus (Strong axis) Wply cm3	Radius of gyration (strong axis) i_y cm	Second moment of area (weak axis) Iz cm4	Elastic modulus (weak axis) Wz cm3	Plastic modulus (weak axis) Wplz cm3	Radius of gyration (weak axis) i_z cm	Torsional constant inertia It cm4	Elastic modulus torsion Wt cm3	Warping factor Cw cm6	Imperfection value for buckling (strong axis) alpha_y -	Imperfection value for buckling (weak axis) alpha_z -	Imperfection value for lateral torsional buckling alpha_LT -	Type of product (*) Product -
Sweden	KCKR	KCKR40,4/3	O	42.4	3	2.12	3.71	2.36	2.36	7.25	3.42	4.67	1.4	7.25	3.42	4.67	1.4	14.5	6.84	0	0.49	0.49	0.76	0
Sweden	KCKR	KCKR40,4/4	O	42.4	4	2.12	4.83	3.07	3.07	8.99	4.24	5.92	1.36	8.99	4.24	5.92	1.36	18	8.48	0	0.49	0.49	0.76	0
Sweden	KCKR	KCKR48,3/3	O	48.3	3	2.415	4.27	2.72	2.72	11	4.55	6.17	1.61	11	4.55	6.17	1.61	22	9.11	0	0.49	0.49	0.76	0
Sweden	KCKR	KCKR48,3/4	O	48.3	4	2.415	5.57	3.55	3.55	13.8	5.7	7.87	1.57	13.8	5.7	7.87	1.57	27.5	11.4	0	0.49	0.49	0.76	0
Sweden	KCKR	KCKR60,3/3	O	60.3	3	3.015	5.4	3.44	3.44	22.2	7.37	9.86	2.03	22.2	7.37	9.86	2.03	44.4	14.7	0	0.49	0.49	0.76	0
Sweden	KCKR	KCKR60,3/4	O	60.3	4	3.015	7.07	4.50	4.50	28.2	9.34	12.7	2	28.2	9.34	12.7	2	56.3	18.7	0	0.49	0.49	0.76	0
Sweden	KCKR	KCKR76,1/4	O	76.1	4	3.805	9.06	5.77	5.77	59.1	5.15	20.8	2.55	59.1	5.15	20.8	2.55	118	31	0	0.49	0.49	0.76	0
Sweden	KCKR	KCKR76,1/5	O	76.1	5	3.805	11.2	7.13	7.13	70.9	18.6	25.3	2.52	70.9	18.6	25.3	2.52	142	37.3	0	0.49	0.49	0.76	0
Sweden	KCKR	KCKR88,9/4	O	88.9	4	4.445	10.7	6.81	6.81	96.3	21.7	28.9	3	96.3	21.7	28.9	3	193	43.3	0	0.49	0.49	0.76	0
Sweden	KCKR	KCKR88,9/5	O	88.9	5	4.445	13.2	8.40	8.40	116	26.2	35.2	2.97	116	26.2	35.2	2.97	233	52.4	0	0.49	0.49	0.76	0
Sweden	KCKR	KCKR101,6/4	O	101.6	4	5.08	12.3	7.83	7.83	146	28.8	38.1	3.45	146	28.8	38.1	3.45	293	57.6	0	0.49	0.49	0.76	0
Sweden	KCKR	KCKR101,6/5	O	101.6	5	5.08	15.2	9.68	9.68	177	34.9	46.7	3.42	177	34.9	46.7	3.42	355	69.9	0	0.49	0.49	0.76	0
Sweden	KCKR	KCKR101,6/6	O	101.6	6	5.08	18	11.46	11.46	207	40.7	54.9	3.39	207	40.7	54.9	3.39	413	81.4	0	0.49	0.49	0.76	0
Sweden	KCKR	KCKR114,3/4	O	114.3	4	5.715	13.9	8.85	8.85	211	36.9	48.7	3.9	211	36.9	48.7	3.9	422	73.9	0	0.49	0.49	0.76	0
Sweden	KCKR	KCKR114,3/5	O	114.3	5	5.715	17.2	10.95	10.95	257	45	59.8	3.87	257	45	59.8	3.87	514	89.9	0	0.49	0.49	0.76	0
Sweden	KCKR	KCKR139,7/4	O	139.7	4	6.985	17.1	10.89	10.89	393	56.2	73.7	4.8	393	56.2	73.7	4.8	786	112	0	0.49	0.49	0.76	0
Sweden	KCKR	KCKR139,7/6	O	139.7	6	6.985	25.2	16.04	16.04	564	80.8	107	4.73	564	80.8	107	4.73	1129	162	0	0.49	0.49	0.76	0
Sweden	KCKR	KCKR139,7/8	O	139.7	8	6.985	33.1	21.07	21.07	720	103	139	4.66	720	103	139	4.66	1441	206	0	0.49	0.49	0.76	0
Sweden	KCKR	KCKR168,3/4	O	168.3	4	8.415	20.6	13.11	13.11	697	82.8	108	5.81	697	82.8	108	5.81	1394	166	0	0.49	0.49	0.76	0
Sweden	KCKR	KCKR168,3/6	O	168.3	6	8.415	30.6	19.48	19.48	1009	120	158	5.74	1009	120	158	5.74	1217	240	0	0.49	0.49	0.76	0
Sweden	KCKR	KCKR168,3/8	O	168.3	8	8.415	40.3	25.66	25.66	1297	154	206	5.67	1297	154	206	5.67	2595	308	0	0.49	0.49	0.76	0
Sweden	KCKR	KCKR193,7/6	O	193.7	6	9.685	35.4	22.54	22.54	1560	161	211	6.64	1560	161	211	6.64	3119	322	0	0.49	0.49	0.76	0
Sweden	KCKR	KCKR193,7/8	O	193.7	8	9.685	46.7	29.73	29.73	2016	208	276	6.57	2016	208	276	6.57	4031	416	0	0.49	0.49	0.76	0
Sweden	KCKR	KCKR193,7/10	O	193.7	10	9.685	57.7	36.73	36.73	2442	252	338	6.5	2442	252	338	6.5	4883	504	0	0.49	0.49	0.76	0
Sweden	KCKR	KCKR193,7/12,5	O	193.7	12.5	9.685	71.2	45.33	45.33	2934	303	411	6.42	2934	303	411	6.42	5869	606	0	0.49	0.49	0.76	0
Sweden	KCKR	KCKR219,1/6	O	219.1	6	10.955	40.2	25.59	25.59	2282	208	273	7.54	2282	208	273	7.54	4564	417	0	0.49	0.49	0.76	0
Sweden	KCKR	KCKR219,1/8	O	219.1	8	10.955	53.1	33.80	33.80	2960	270	357	7.47	2960	270	357	7.47	5919	540	0	0.49	0.49	0.76	0
Sweden	KCKR	KCKR219,1/10	O	219.1	10	10.955	65.7	41.83	41.83	3598	328	438	7.4	3598	328	438	7.4	7197	657	0	0.49	0.49	0.76	0
Sweden	KCKR	KCKR219,1/12,5	O	219.1	12.5	10.955	18.1	11.52	11.52	4345	397	534	7.32	4345	397	534	7.32	8689	793	0	0.49	0.49	0.76	0
Sweden	KCKR	KCKR244,5/6	O	244.5	6	12.225	45	28.65	28.65	3199	262	341	8.43	3199	262	341	8.43	6397	523	0	0.49	0.49	0.76	0
Sweden	KCKR	KCKR244,5/8	O	244.5	8	12.225	59.4	37.82	37.82	4160	340	448	8.37	4160	340	448	8.37	8321	681	0	0.49	0.49	0.76	0
Sweden	KCKR	KCKR244,5/10	O	244.5	10	12.225	73.7	46.92	46.92	5073	415	555	8.3	5073	415	555	8.3	10146	830	0	0.49	0.49	0.76	0
Sweden	KCKR	KCKR244,5/12,5	O	244.5	12.5	12.225	91.1	58.00	58.00	6147	503	673	8.21	6147	503	673	8.21	12295	1006	0	0.49	0.49	0.76	0
Sweden	KCKR	KCKR273/8	O	273	8	13.65	66.6	42.40	42.40	5852	429	562	9.37	5852	429	562	9.37	11703	857	0	0.49	0.49	0.76	0
Sweden	KCKR	KCKR273/10	O	273	10	13.65	82.6	52.58	52.58	7174	524	692	9.31	7174	524	692	9.31	14308	1048	0	0.49	0.49	0.76	0
Sweden	KCKR	KCKR273/12,5	O	273	12.5	13.65	102	64.94	64.94	8697	637	849	9.22	8697	637	849	9.22	17395	1274	0	0.49	0.49	0.76	0
Sweden	KCKR	KCKR323,9/10	O	323.9	10	16.195	98.6	62.77	62.77	12158	751	986	11.1	12158	751	986	11.1	24317	1501	0	0.49	0.49	0.76	0
Sweden	KCKR	KCKR323,9/12,5	O	323.9	12.5	16.195	122	77.67	77.67	14847	917	1213	11	14847	917	1213	11	29693	1833	0	0.49	0.49	0.76	0

(*) 0:cold formed; 1: hot finished; 2: welded; 3: rolled

European I beams

Contry	Family	Name	Shape	Depth of section h mm	Thickness of web t_web mm	Upper width of section b_upper mm	Thickness of upper flange t_upper mm	Root radius r mm	Position of centroid zs cm	Area of section A cm2	Effective shear area Vy Ay cm2	Effective shear area Vz Az cm2	Second moment of area (strong axis Iy cm4	Elastic modulus upper (strong axis) Wy cm3	Plastic modulus (Strong axis) Wply cm3	Radius of gyration (strong axis) i_y cm	Second moment of area (weak axis) Iz cm4	Elastic modulus (weak axis) Wz cm3	Plastic modulus (weak axis) Wplz cm3	Radius of gyration (weak axis) i_z cm	Torsional constant inertia It cm4	Elastic modulus torsion Wt cm3	Warping factor Cw cm6	Imperfection value for buckling (strong axis) alpha_y -	Imperfection value for buckling (weak axis) alpha_z -	Imperfection value for lateral torsional buckling alpha_LT -	Type of product (*) Product -
EU	IPE	IPE80	I	80	3.8	46	5.2	5	4	7.64	4.78	2.64	80	20.0	23.2	3.24	8.5	3.69	5.82	1.05	0.7	1.35	118	0.21	0.34	0.34	3
EU	IPE	IPE100	I	100	4.1	55	5.7	7	5	10.32	6.27	3.63	171	34.2	39.4	4.07	15.9	5.79	9.15	1.24	1.21	2.12	351	0.21	0.34	0.34	3
EU	IPE	IPE120	I	120	4.4	64	6.3	7	6	13.21	8.06	4.73	318	53	60.7	4.9	27.7	8.65	13.6	1.45	1.74	2.76	890	0.21	0.34	0.34	3
EU	IPE	IPE140	I	140	4.7	73	6.9	7	7	16.43	10.07	5.93	541	77.3	88.3	5.74	45	12.3	19.2	1.65	2.45	3.55	1900	0.21	0.34	0.34	3
EU	IPE	IPE160	I	160	5	82	7.4	9	8	20.09	12.14	7.26	869	109	124	6.58	68	16.7	26.1	1.84	3.62	4.89	3960	0.21	0.34	0.34	3
EU	IPE	IPE180	I	180	5.3	91	8	9	9	23.95	14.56	8.69	1317	146	166	7.42	101	22.2	34.6	2.05	4.8	6	7430	0.21	0.34	0.34	3
EU	IPE	IPE200	I	200	5.6	100	8.5	12	10	28.48	17.00	10.25	1943	194	221	8.26	142	28.5	44.6	2.24	7.02	8.26	13000	0.21	0.34	0.34	3
EU	IPE	IPE220	I	220	5.9	110	9.2	12	11	33.37	20.24	11.89	2772	252	285	9.11	205	37.3	58.1	2.48	9.1	9.89	22700	0.21	0.34	0.34	3
EU	IPE	IPE240	I	240	6.2	120	9.8	15	12	39.12	23.52	13.66	3892	324	367	9.97	284	47.3	73.9	2.69	12.9	13.2	37400	0.21	0.34	0.34	3
EU	IPE	IPE270	I	270	6.6	135	10.2	15	13.5	45.94	27.54	16.47	5790	429	484	11.2	420	62.2	97	3.02	16	15.7	70600	0.21	0.34	0.34	3
EU	IPE	IPE300	I	300	7.1	150	10.7	15	15	53.81	32.10	19.78	8356	557	628	12.5	604	80.5	125	3.35	20.2	18.9	126000	0.21	0.34	0.34	3
EU	IPE	IPE330	I	330	7.5	160	11.5	18	16.5	62.61	36.80	23.03	11770	713	804	13.7	788	98.5	154	3.55	28.3	24.6	199000	0.21	0.34	0.49	3
EU	IPE	IPE360	I	360	8	170	12.7	18	18	72.73	43.18	26.77	16270	904	1020	15.0	1043	123	191	3.79	37.5	29.5	314000	0.21	0.34	0.49	3
EU	IPE	IPE400	I	400	8.6	180	13.5	21	20	84.46	48.60	32.08	23130	1160	1310	16.5	1318	146	229	3.95	51.4	38.1	490000	0.21	0.34	0.49	3
EU	IPE	IPE450	I	450	9.4	190	14.6	21	22.5	98.82	55.48	39.56	33740	1500	1700	18.5	1676	176	276	4.12	67.1	46	791000	0.21	0.34	0.49	3
EU	IPE	IPE500	I	500	10.2	200	16	21	25	115.5	64.00	47.74	48200	1930	2190	20.4	2142	214	336	4.31	89.7	56.1	1250000	0.21	0.34	0.49	3
EU	IPE	IPE550	I	550	11.1	210	17.2	24	27.5	134.4	72.24	57.23	67120	2440	2790	22.3	2668	254	401	4.45	124	72.1	1880000	0.21	0.34	0.49	3
EU	IPE	IPE600	I	600	12	220	19	24	30	156	83.60	67.44	92080	3070	3510	24.3	3387	308	486	4.66	166	87.4	2850000	0.21	0.34	0.49	3

(*) 0:cold formed; 1: hot finished; 2: welded; 3: rolled;

D Verification of the Warren sub model in Karamba 3D with FEM-Design

This chapter presents the results from the Warren truss sub model in Karamba 3D and FEM-Design considering the sectional forces, the reaction forces and the maximum displacement of the bridge. The chapter is concluding with an extensive study of the maximum utilization ratio of the cross beams of the Warren truss sub model.

D.1 Verification of the sectional forces and the maximum displacement

In this section the verification results are presented, comparing the Warren truss sub model in Karamba 3D with FEM-Design. First, Table D.1 shows all the factors used in the different load combinations with given names, which are referred to later in this appendix. The load combination used for the verification is $6.10b_1$, including the permanent load and the crowd load.

Table D.1: All load combinations used in the created model in Karamba 3D.

Load combination	Type	Name	Self-weight	Crowd load
6.10a	ULS	$6.10a_1$	1.35	0.6
		$6.10a_2$	1	0.6
6.10b	ULS	$6.10b_1$	1.2	1.5
		$6.10b_2$	1.2	0.6
		$6.10b_3$	1	1.5
		$6.10b_4$	1	0.6
6.10a-b	SLS	$6.10ab_1$	1	0.4
		$6.10ab_2$	1	0

Secondly, the positions (a to f) considering the x-direction only, which are used in both models and are presented in Figure D.1 from a side view to facilitate the understanding of the results later.

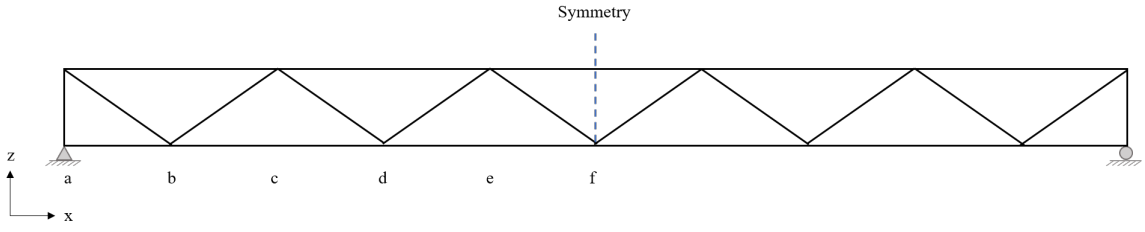

Figure D.1: Identification of the positions of the Warren sub model.

On the following pages first the convergence study of the weakening factor of the bridge deck and its influence on the normal force of the bottom chord is presented. Following, the results of sectional forces of the different members, i.e. the bottom chord, top chord, diagonals and the end posts, are presented. Also, the maximum displacements downwards and reaction forces of the bridge from the

two software are compared. The tables are followed by diagrams of the normal force (N), the shear forces in z-direction (Vz and Tz' in Karamba 3D and FEM-Design respectively) and the moment about the y-axis (My') of the top chord and bottom chord.

Load case	6.10b1

		Karamba 3D							
		Weakening factor	1	10	50	100	1000	5000	10 000	1 000 000
Normal force [kN] (absolute values)	Bottom chords	a	1,3	1,1	1,2	1,8	2,5	2,5	2,5	2,5
		b	31,4	21,8	4,7	1,2	2,2	2,5	2,5	2,5
			77,8	203,2	249,5	257,6	265,6	266,5	266,6	266,7
		d	32,4	169,1	239,7	252,5	265,2	266,4	266,5	266,7
			86,7	284,1	370,5	385,9	401,1	402,6	402,8	402,9
		f	71,6	272,0	367,1	384,1	401,0	402,6	402,8	402,9
	Top chord	b	162,2	162,0	161,9	161,9	161,9		161,9	
		d	369,4	368,9	368,7	368,6	368,5		368,5	
		f	436,4	435,8	435,5	435,4	435,4		435,4	
	Diagonals	a-b	194,7	194,3	194,2	194,2	194,2		194,2	
		b-c	128,1	127,7	137,4	127,4	127,3		127,3	
		c-d	124,4	124,4	124,4	124,4	124,4		124,4	
		d-e	42,8	42,4	42,2	42,2	42,2		42,2	
		e-f	39,3	39,5	39,6	39,7	39,7		39,7	
	End posts	All 4	112,8	122,7	112,7	112,7	112,7		112,7	

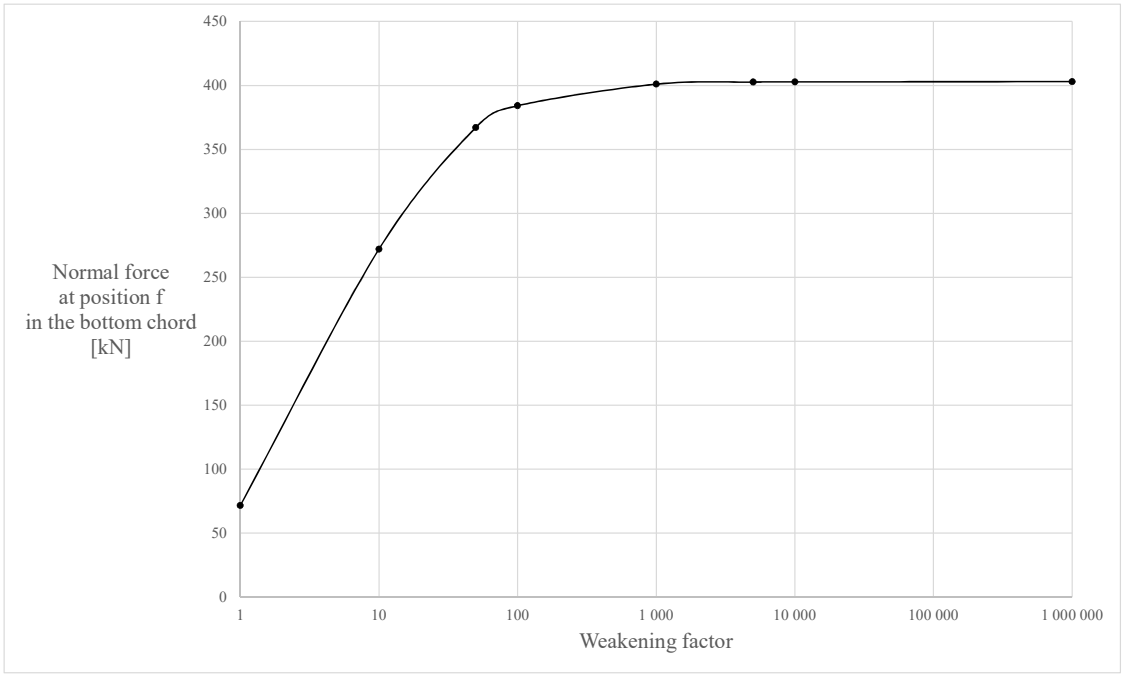

Load case	6.10b1

			Normal force [kN] (absolute values)			Normal force [kN] (absolute values)		
	Description	Member	Karamba 3D 10 000*	FEM-Design 10 000*	Difference	Karamba 3D 1*	FEM-Design 1*	Difference
Normal force N	Bottom chords	a	3,2	3,0	4,3%	1,0	1,8	-42%
		b (left)				31,1	91,3	-66%
		b (right)				77,6	141,5	-45%
		c	266,3	270,1	-1,4%			
		d (left)				32,0	0,5	6709%
		d (right)				86,7	122,7	-29%
		f	403,0	411,2	-2,0%	71,6	73,9	-3%
	Top chord	a-b	162,3	164,1	-1,1%	162,7	164,6	-1%
		b-d	368,6	376,0	-2,0%	396,6	377,2	5%
		d-f	435,5	444,5	-2,0%	436,6	445,9	-2%
	Diagonals	a-b	194,1	196,5	-1,2%	194,7	197,1	-1%
		b-c	126,8	129,6	-2,1%	127,5	130,3	-2%
		c-d	124,7	129,0	-3,3%	124,9	129,2	-3%
		d-e	42,2	43,3	-2,5%	42,6	43,7	-3%
		e-f	39,5	40,5	-2,5%	39,3	40,4	-3%
	End posts	All 4	113,2	114,5	-1,1%	113,3	114,7	-1%

Cross beams	a	0,13	0,12
	b	0,25	0,25
	d	0,02	0
	f	0,07	0,08

*1**	*Bridge deck is weakened with a factor of 1*
*10 000**	*Bridge deck is weakened with a factor of 10 000*

			Moment My [kNm] (absolute values)			Moment My [kNm] (absolute values)		
	Description	Member	Karamba 3D 10 000*	FEM-Design 10 000*	Difference	Karamba 3D 1*	FEM-Design 1*	Difference
Moment My	Bottom chord	a	2,5	2,3	5,6%	2,4	2,3	3%
		b	10,3	10,4	-1,3%	10,2	10,6	-4%
		c	10,2	10,5	-3,2%	9,7	10,0	-3%
		d	14,0	14,4	-3,2%	14,1	14,7	-4%
		e	9,1	9,3	-2,3%	8,3	8,5	-3%
		f	12,2	12,6	-2,9%	12,5	13,1	-5%
	Top chord	a	2,1	2,1				
		b	-	-				
		c	2,3	2,3				
		d	2,7	2,7				
		e	2,2	2,3				
		f	2,8	2,9				
	Diagonals	a-b	0,1	0,1				
			0,5	0,5				
		b-c	0,1	0,1				
			0,1	0,1				
		c-d	0,1	0,1				
			0,1	0,2				
		d-e	0,1	0,0				
			0,1	0,1				
		e-f	0,1	0,1				
			0,0	0,1				
	End posts	All 4	2,5	2,3				
			2,0	1,9				

Description	Member	Karamba 3D 10 000*	FEM-Design 10 000*
Cross beams	a	5,1	4,6
	b	5,3	5,4
	d	5,6	6,1
	f	5,7	6,2

*1**	*Bridge deck is weakened with a factor of 1*
*10 000**	*Bridge deck is weakened with a factor of 10 000*

			Shear Vz [kN] (absolute values)			Shear Vz [kN] (absolute values)		
	Description	Member	Karamba 3D 10 000*	FEM-Design 10 000*	Differemce	Karamba 3D 1*	FEM-Design 1*	Difference
Shear force Vz	Bottom chord	a	6,0	5,7	4,2%	5,6	5,4	2,9%
		b (left)	12,3	11,7	5,0%	11,9	11,5	4,0%
		b (right)	17,7	18,3	-3,0%	16,8	18,6	-9,6%
		d (left)	19,6	20,3	-3,6%	18,7	20,1	-6,8%
		d (right)	19,0	19,7	-3,5%	18,1	19,4	-6,9%
		f	18,2	18,9	-3,3%	17,4	18,6	-6,7%
	Top chord	a	1,8	1,8				
		c	0,8	0,8				
		e (left)	0,6	0,5				
		e (right)	0,7	0,7				
		f	0,0	0,0				
	Diagonals	a-b	0,3	0,3				
		b-c	0,1	0,1				
		c-d	0,0	0,0				
		d-e	0,0	0,0				
		e-f	0,0	0,0				
	End posts	All 4	3,2	3,0				
	Cross beams	a	4,3	2,9				
		b	8,3	7,8				
		d	8,3	8,5				
		f	8,3	8,5				
	*1**	*Bridge deck is weakened with a factor of 1*						
	*10'000**	*Bridge deck is weakened with a factor of 10'000*						

			Reaction force of one support [kN]		
Reaction forces	Load	Member	Karamba 3D 10 000*	FEM-Design 10 000*	Difference
	Self-weight	All	24,8	24,4	1,6%
	Crowd load	All	62,5	62,5	0,0%

			Max. displacement ULS [m]		
Displacement	Description	Member	Karamba 3D 10 000*	FEM-Design 10 000*	Difference
	Max. displacement [mm]	All	52,2	53,2	-2,0%

*10 000** *Bridge deck is weakened with a factor of 10'000*

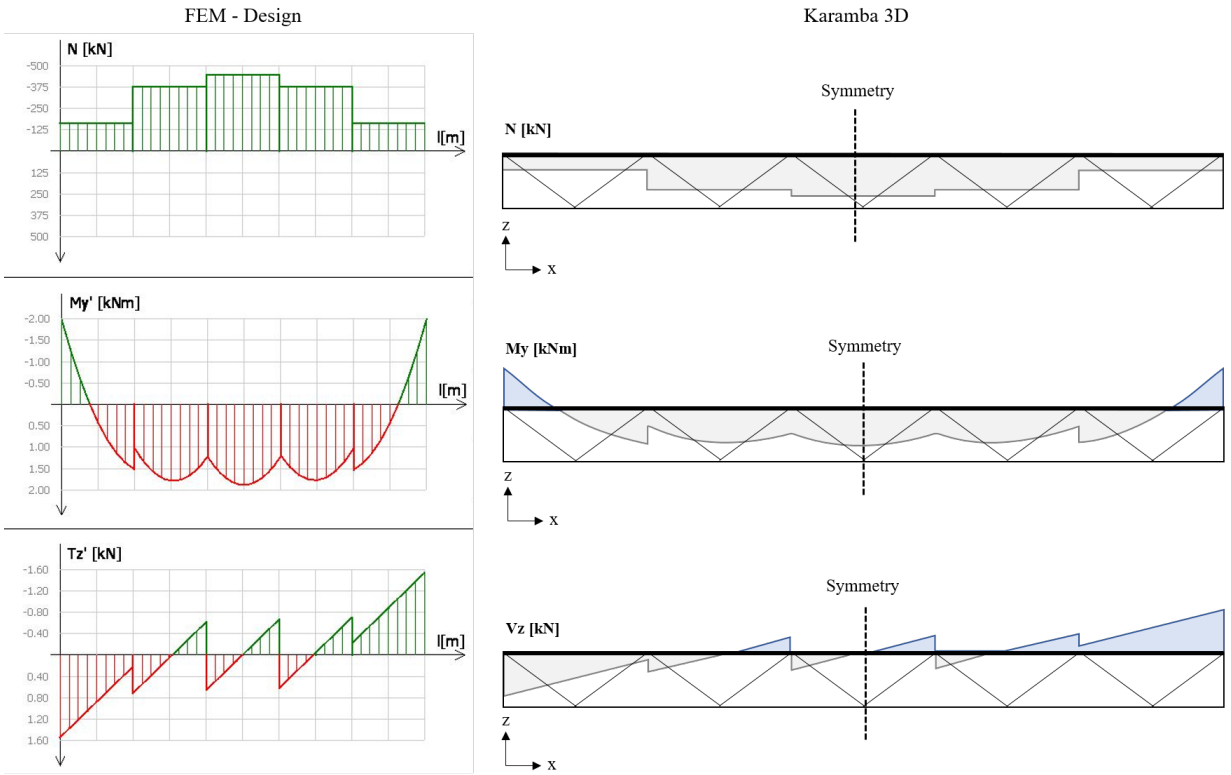

Figure D.2: Normal force, moment and shear force diagram of the top chord from FEM-Design (left) and Karamba 3D (right) with a bridge deck which is weakened with a factor 1.

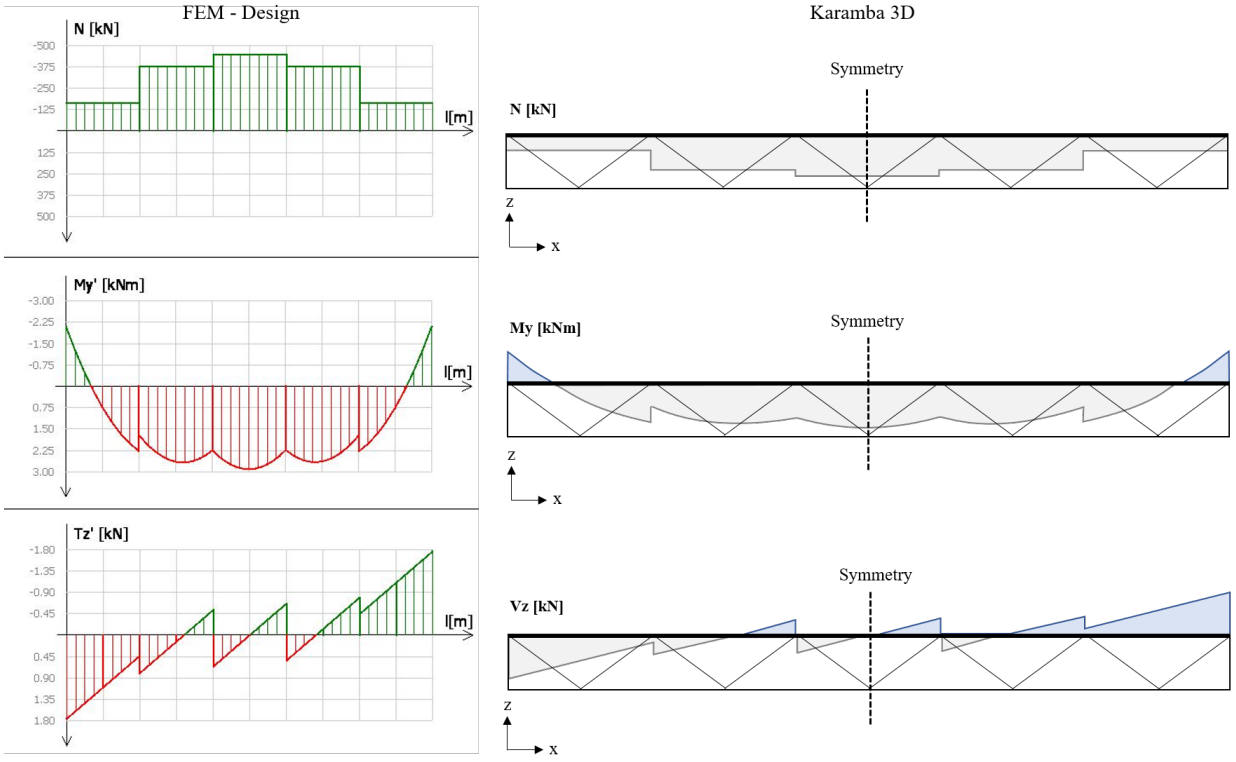

Figure D.3: Normal force, moment and shear force diagram of the top chord from FEM-Design (left) and Karamba 3D (right) with a bridge deck which is weakened with a factor 10 000.

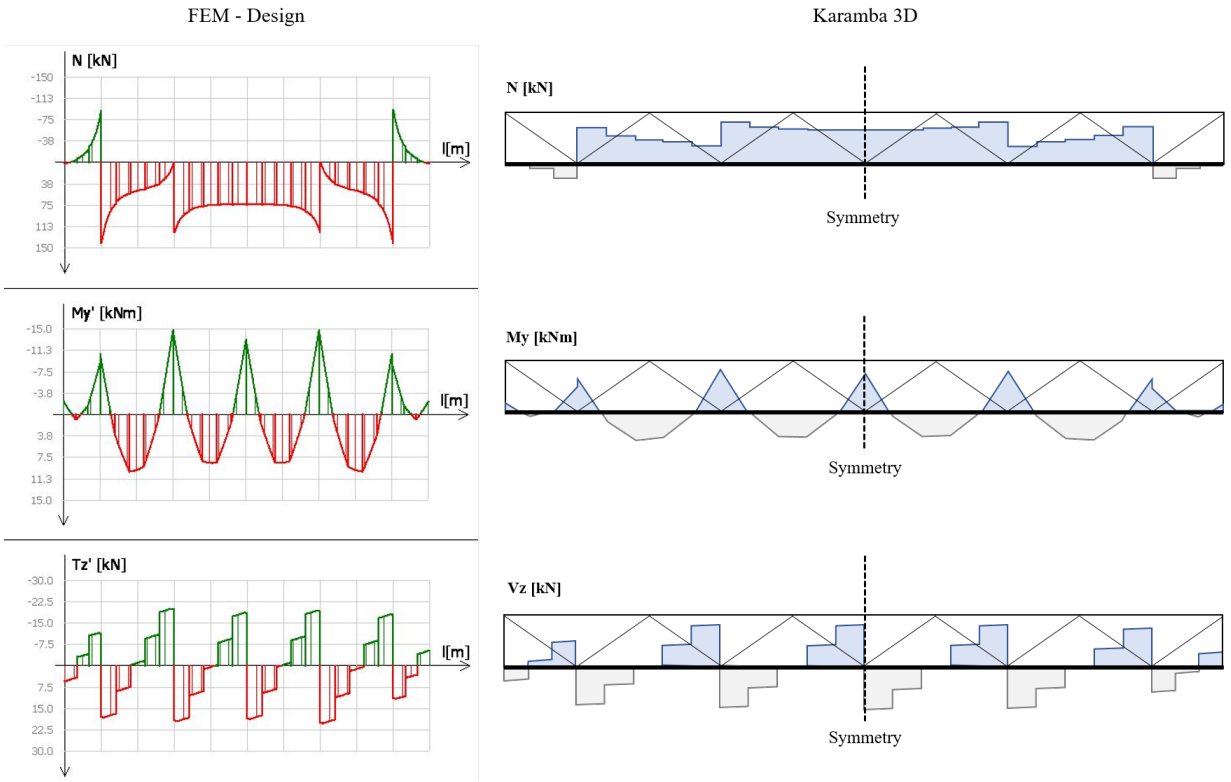

Figure D.4: Normal force, moment and shear force diagram of the bottom chord from FEM-Design (left) and Karamba 3D (right) with a bridge deck which is weakened with a factor 1.

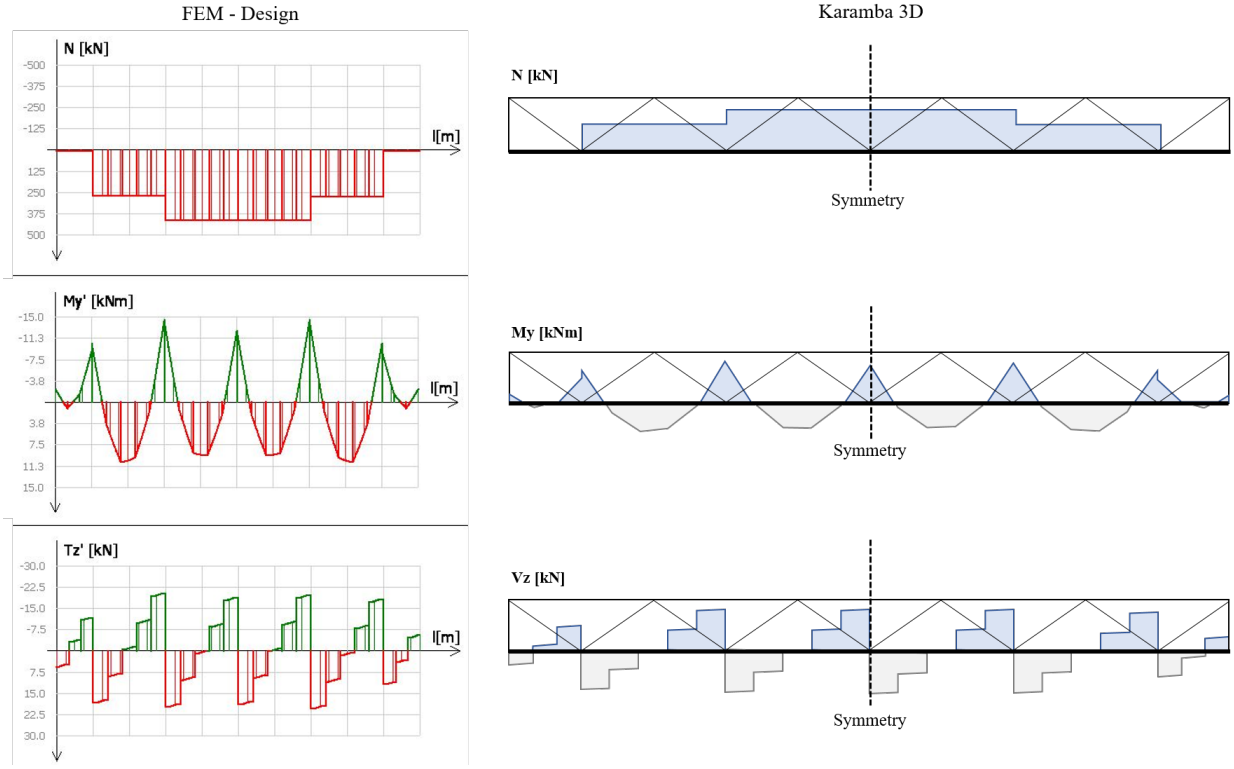

Figure D.5: Normal force, moment and shear force diagram of the bottom chord from FEM-Design (left) and Karamba 3D (right) with a bridge deck which is weakened with a factor 10 000.

D.2 Verification of the utilization ratios of the elements

In this section the comparison of the utilization ratios from Karamba 3D and FEM-Design of load case $6.10b_1$, see Table D.1, are presented. First, all the controls executed in both software are displayed, followed by the worst utilization ratios for each member in the Warren truss sub model for Karamba 3D and FEM-Design. After that, the cross beam at position f, see Figure D.1, is investigated further without and with adjustment of the buckling length of the cross beam. With adjustment of the buckling length indicates, that the buckling length now is 2.7 m in x- and z-direction, i.e. the length of the member. Following pages show the calculation results from FEM-Design for the cross beam at position f with load case $6.10b_1$.

Controls which are executed in FEM-Design and Karamba 3D

Control	Chapter in EN 1993-1-1
Shear resistance	6.2.6,6.2.8
Torsional resistance	6.2.7
Shear stress	6.2.6
Normal stress	6.2.1
Normal capacity	6,2
Flexural buckling	6.3.1
Torsional-flexural buckling	6.3.1
Lateral torsional buckling	6.3.2.2
Interaction between normal force and bending	6.3.3
Interaction between normal force and bending, 2nd order	6.3.3

Input values of the cross section 6.10b1 cross beam (IPE 140) at position f

	Karamba 3D	FEM-Design	Difference
A [mm2]	1643	1643	0,0%
Iy [mm4]	5410000	5412000	0,0%
Iz [mm4]	450000	449200	0,2%
Wply [mm3]	88300	88340	0,0%
Wplz [mm3]	19200	19260	-0,3%
iy [mm]	57,4	57	0,7%
iz [mm]	16,5	17	-2,9%
It [mm4]	24500	24010	2,0%
Iw [mm6]	1900000000	1951000000	-2,6%
fy [N/mm2]	355	355	0,0%
ε	0,81	0,81	0,0%

Preconditions: Load case 6.10b1, cross sections and geometry are the same as in the case study.
Comparison of the maximum utilization ratios of each element between Karamba 3D and FEM-Design.

	Without adjustments for buckling lengths			With adjustments for buckling lengths		
	Karamba 3D 10'000, maximum utilization ratio	FEM-Design 10'000, maximum utilization ratio	Difference	Karamba 3D 10'000, maximum utilization ratio	FEM-Design 10'000, maximum utilization ratio	Difference
Bottom chord	61,5%	67,0%	-5,5%	64,0%	67,0%	-3,0%
Top chord	51,2%	53,0%	-1,8%	51,2%	53,0%	-1,8%
Diagonals	65,3%	60,0%	5,3%	65,0%	60,0%	5,0%
Vertical end post	30,6%	30,0%	0,6%	30,6%	30,0%	0,6%
Cross beams	17,7%	47,0%	-29,3%	35,3%	47,0%	-11,7%
End cross beams	8,5%	15,0%	-6,5%	14,9%	15,0%	-0,2%

	Maximum utilization of the cross beams at position f - without adjustment of the buckling length			Maximum utilization of the cross beams at position f - with adjustment of the buckling length		
Description	Karamba 3D	FEM-Design	Difference	Karamba 3D	FEM-Design	Difference
Shear resistance Vy	0%	0%	0%	0%	0%	0%
Shear resistance Vz	6,8%	5,0%	1,8%	5,6%	5,0%	0,6%
Moment resistance My	17,7%	47,0%	-29,3%	35,2%	47,0%	-11,8%
Moment resistance Mz	0,6%	0,0%	0,6%	0,3%	0,0%	0,3%
Normal capacity N	0%	0%	0%	0,2%	0,0%	0,2%
Max utilization ratio	17,7%	47,0%	-29,3%	0,35	47,0%	-11,8%

Comparison of details about input and output data between Karamba 3D and FEM-Design, without and with adjustment of the buckling lengths

		Without adjustment of buckling lengths			With adjustment of buckling lengths			
		Karamba 3D, 1st order	FEM-Design	Difference	Karamba 3D, 1st order	FEM-Design	Difference	Comment
Cross beam at position f	CSC	1	1	0%	1	1	0%	OK
	NRd [kN]	591,5	583,1	1,4%	591,5	583,1	1,4%	OK
	Ncr [kN]	127,9	127,7	0,2%	127,9	127,7	0,2%	OK
	VyRd [kN]	209,4	215,1	-2,7%	209,4	215,1	-2,7%	Due to different shear areas
	VzRd [kN]	123,3	156,6	-21,3%	123,3	156,6	-21,3%	Due to different shear areas
	MyRd [kNm] (No X_LT reduction)	31,8	31,4	1,2%	31,8	31,4	1,2%	OK
	Mcr [kNm]	846,4	16,1	5147,5%	18,0	16,1	11,3%	Dependent on the k-factors below
	Cmy	0,9	1,0	-10,0%	1	1	0%	OK
	Cmz	0,9	1,0	-10,0%	1	1	0%	OK
	CmLT	0,9	1,0	-10,0%	1	1	0%	OK
	X_LT	1	0,42	138,1%	0,51	0,42	20,8%	Dependent on Mcr
	kyy*	0,90	1	-10,0%	1	1	0%	OK
	kzz*	0,90	1,03	-12,6%	1,00	1,03	-2,6%	OK
	kyz*	0,54	0,82	-34,1%	0,60	0,82	-26,6%	*
	kzy*	0,815	0,52	56,7%	1,00	0,52	92,2%	*

*

Karamba 3D	FEM-Design
Interaction values (kyy, kzz etc) from EN1991-1-1 appendix B, method 2	Interaction values (kyy, kzz etc) from EN1991-1-1 appendix A, method 1

B.37.1
Maximum of load combinations

S 355

$E = 210000\ N/mm^2$

$G = 80769\ N/mm^2$

$\gamma_{M0,ult} = 1.00$ $\quad \gamma_{M0,acc/seis} = 1.00$

$\gamma_{M1,ult} = 1.00$ $\quad \gamma_{M1,acc/seis} = 1.00$

$\gamma_{M2,ult} = 1.20$ $\quad \gamma_{M2,acc/seis} = 1.00$

IPE 140

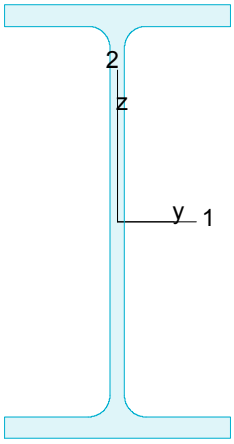

$A = 1643\ mm^2$ $\quad f_y = 355\ N/mm^2$

$I_y = 5.412e+06\ mm^4$ $\quad \varepsilon = 0.81$

$I_z = 4.492e+05\ mm^4$ $\quad \lambda_1 = 76.40$

$I_1 = 5.412e+06\ mm^4$

$I_2 = 4.492e+05\ mm^4$

$W_{pl,1} = 8.834e+04\ mm^3$

$W_{pl,2} = 1.926e+04\ mm^3$

$W_{el,min,1} = 7.732e+04\ mm^3$

$W_{el,min,2} = 1.231e+04\ mm^3$

$i_1 = 57\ mm$

$i_2 = 17\ mm$

$I_t = 2.401e+04\ mm^4$

$I_w = 1.951e+09\ mm^6$

Shear resistance, 1-1 - Part 1-1: 6.2.6, 6.2.8

LC: '6.10b_1', x = 2700 mm

$Class_N = 1$, $Class_{M1} = 1$, $Class_{M2} = 1$

$$V_{1,pl,Rd} = \frac{A_{1,v} \cdot f_y}{\sqrt{3} \cdot \gamma_{M0}} = \frac{1049 \cdot 355}{\sqrt{3} \cdot 1.00} = 215.10\ kN \quad (6.18)$$

$$V_{1,pl,T,Rd} = \sqrt{1 - \frac{\tau_{t,Ed}}{1.25\ (f_y / \sqrt{3}) / \gamma_{M0}}} \cdot V_{1,pl,Rd} =$$

$$= \sqrt{1 - \frac{0.00}{1.25\ (355 / \sqrt{3}) / 1.00}} \cdot 215.10 = 215.10\ kN \quad (6.26)$$

$$\frac{V_{1,Ed}}{V_{1,pl,T,Rd}} = \frac{0.00}{215.10} = 0.00 \le 1.00 \quad (6.25)\ \text{- OK}$$

Shear resistance, 2-2 - Part 1-1: 6.2.6, 6.2.8

LC: '6.10b_1', x = 2700 mm

$Class_N = 1$, $Class_{M1} = 1$, $Class_{M2} = 1$

$$V_{2,pl,Rd} = \frac{A_{2,v} \cdot f_y}{\sqrt{3} \cdot \gamma_{M0}} = \frac{764 \cdot 355}{\sqrt{3} \cdot 1.00} = 156.64\ kN \quad (6.18)$$

$$V_{2,pl,T,Rd} = \sqrt{1 - \frac{\tau_{t,Ed}}{1.25\ (f_y / \sqrt{3}) / \gamma_{M0}}} \cdot V_{2,pl,Rd} =$$

$$= \sqrt{1 - \frac{0.00}{1.25\ (355 / \sqrt{3}) / 1.00}} \cdot 156.64 = 156.64\ kN \quad (6.26)$$

$$\frac{V_{2,Ed}}{V_{2,pl,T,Rd}} = \frac{8.49}{156.64} = 0.05 \le 1.00 \quad (6.25)\ \text{- OK}$$

Torsional resistance - Part 1-1: 6.2.7
LC: '6.10a_1', x = 0 mm

$Class_N = 1$, $Class_{M1} = 1$, $Class_{M2} = 1$

$\tau_{max,unit} = 439.20 \frac{N/mm^2}{kNm}$ is calculated by FEM analysis.

$$T_{Rd} = \frac{f_y}{\sqrt{3} \cdot \tau_{max,unit}} = \frac{355}{\sqrt{3} \cdot 439.20} = 0.47 \text{ kNm}$$

$$\frac{T_{Ed}}{T_{Rd}} = \frac{0.00}{0.47} = 0.00 \leq 1.00 \quad (6.23) \text{ - OK}$$

Shear stress - Part 1-1: 6.2.6
Not relevant

Normal stress - Part 1-1: 6.2.1
Not relevant

Normal capacity - Part 1-1: 6.2
LC: '6.10b_1', x = 1350 mm

$Class_N = 1$, $Class_{M1} = 1$, $Class_{M2} = 1$

$V_{1,Ed} = 0.00 \text{ kN} \leq 0.5 \cdot V_{1,pl,T,Rd} = 107.55 \text{ kN} \rightarrow \rho_1 = 0.00$

$V_{2,Ed} = 0.00 \text{ kN} \leq 0.5 \cdot V_{2,pl,T,Rd} = 78.32 \text{ kN} \rightarrow \rho_1 = 0.00$

$$\frac{N_{Ed}}{N_{Rd}} + \frac{M_{1,Ed}}{M_{1,Rd}} + \frac{M_{2,Ed}}{M_{2,Rd}} = \frac{0.08}{583.12} + \frac{6.18}{31.36} + \frac{0.00}{6.84} = 0.20 \leq 1.00 \quad (6.2) \text{ - OK}$$

Flexural buckling, 1-1 - Part 1-1: 6.3.1
LC: '6.10b_1', x = 1800 mm

$Class_N = 1$, $Class_{M1} = 1$, $Class_{M2} = 1$

$$\bar{\lambda}_1 = \frac{L_{cr,1}}{i_1 \cdot \lambda_1} = \frac{2700}{57 \cdot 76.40} = 0.62 \quad (6.50)$$

$\alpha_1 = 0.21$ (Buckling curve: a)

$$\varphi_1 = 0.5 \left[1 + \alpha_1 \cdot \left(\bar{\lambda}_1 - 0.2\right) + \bar{\lambda}_1^2\right] = 0.5 \left[1 + 0.21 \cdot (0.62 - 0.2) + 0.62^2\right] = 0.73$$

$$\chi_1 = \min\left(\frac{1}{\varphi_1 + \sqrt{\varphi_1^2 - \bar{\lambda}_1^2}}, 1.0\right) = \min\left(\frac{1}{0.73 + \sqrt{0.73^2 - 0.62^2}}, 1.0\right) = 0.88 \quad (6.49)$$

$$N_{b,Rd,1} = \frac{\chi_1 \cdot A \cdot f_y}{\gamma_{M1}} = \frac{0.88 \cdot 1643 \cdot 355}{1.00} = 515.45 \text{ kN} \quad (6.47)$$

$$\frac{N_{Ed}}{N_{b,Rd,1}} = \frac{0.08}{515.45} = 0.00 \leq 1.00 \quad (6.46) \text{ - OK}$$

Flexural buckling, 2-2 - Part 1-1: 6.3.1
LC: '6.10b_1', x = 1800 mm

$Class_N = 1$, $Class_{M1} = 1$, $Class_{M2} = 1$

$$\bar{\lambda}_2 = \frac{L_{cr,2}}{i_2 \cdot \lambda_1} = \frac{2700}{17 \cdot 76.40} = 2.14 \quad (6.50)$$

$\alpha_2 = 0.34$ (Buckling curve: b)

$$\varphi_2 = 0.5 \left[1 + \alpha_2 \cdot (\bar{\lambda}_2 - 0.2) + \bar{\lambda}_2^{\,2}\right] = 0.5 \left[1 + 0.34 \cdot (2.14 - 0.2) + 2.14^2\right] = 3.11$$

$$\chi_2 = \min\left(\frac{1}{\varphi_2 + \sqrt{\varphi_2^{\,2} - \bar{\lambda}_2^{\,2}}}, 1.0\right) = \min\left(\frac{1}{3.11 + \sqrt{3.11^2 - 2.14^2}}, 1.0\right) = 0.19 \quad (6.49)$$

$$N_{b,Rd,2} = \frac{\chi_2 \cdot A \cdot f_y}{\gamma_{M1}} = \frac{0.19 \cdot 1643 \cdot 355}{1.00} = 108.46 \text{ kN} \quad (6.47)$$

$$\frac{N_{Ed}}{N_{b,Rd,2}} = \frac{0.08}{108.46} = 0.00 \le 1.00 \quad (6.46) \text{ - OK}$$

Torsional-flexural buckling - Part 1-1: 6.3.1
LC: '6.10b_1', x = 1800 mm

$Class_N = 1$, $Class_{M1} = 1$, $Class_{M2} = 1$

$$i_0 = \sqrt{i_1^{\,2} + i_2^{\,2} + y_0^{\,2} + z_0^{\,2}} = \sqrt{57^2 + 17^2 + 0^2 + 0^2} = 60 \text{ mm}$$

$$N_{cr,1} = \frac{\pi^2 \cdot E \cdot I_1}{L_{cr,1}^{\,2}} = \frac{\pi^2 \cdot 210000 \cdot 5412243}{2700^2} = 1538.75 \text{ kN}$$

$$N_{cr,2} = \frac{\pi^2 \cdot E \cdot I_2}{L_{cr,2}^{\,2}} = \frac{\pi^2 \cdot 210000 \cdot 449178}{2700^2} = 127.71 \text{ kN}$$

$$N_{cr,T} = \frac{1}{i_0^{\,2}}\left(G \cdot I_t + \frac{\pi^2 \cdot E \cdot I_w}{I_T^{\,2}}\right) =$$

$$= \frac{1}{60^2}\left(80769 \cdot 2.401e{+}04 + \frac{\pi^2 \cdot 210000 \cdot 1.951e{+}09}{2700^2}\right) = 698.91 \text{ kN}$$

$$i_0^{\,2} (N - N_{cr,1}) (N - N_{cr,2}) (N - N_{cr,T}) - N^2 y_0^{\,2} (N - N_{cr,2}) - N^2 z_0^{\,2} (N - N_{cr,1}) = 0$$

Smallest root of the above equation:

$N_{cr,TF} = 698.91$ kN

$N_{cr} = \min(N_{cr,T}, N_{cr,TF}) = \min(698.91, 698.91) = 698.91$ kN

$$\bar{\lambda}_T = \sqrt{\frac{A \cdot f_y}{N_{cr}}} = \sqrt{\frac{1643 \cdot 355}{698.91}} = 0.91 \quad (6.53)$$

$\alpha_T = 0.34$ (Buckling curve: b)

$$\varphi_T = 0.5 \left[1 + \alpha_T \cdot (\bar{\lambda}_T - 0.2) + \bar{\lambda}_T^{\,2}\right] = 0.5 \left[1 + 0.34 \cdot (0.91 - 0.2) + 0.91^2\right] = 1.04$$

$$\chi_T = \min\left(\frac{1}{\varphi_T + \sqrt{\varphi_T^{\,2} - \bar{\lambda}_T^{\,2}}}, 1.0\right) = \min\left(\frac{1}{1.04 + \sqrt{1.04^2 - 0.91^2}}, 1.0\right) = 0.65 \quad (6.49)$$

$$N_{b,Rd,T} = \frac{\chi_T \cdot A \cdot f_y}{\gamma_{M1}} = \frac{0.65 \cdot 1643 \cdot 355}{1.00} = 380.52 \text{ kN} \quad (6.47)$$

$$\frac{N_{Ed}}{N_{b,Rd,T}} = \frac{0.08}{380.52} = 0.00 \le 1.00 \text{ - OK}$$

Lateral torsional buckling - Part 1-1: 6.3.2.2
LC: '6.10b_1', x = 1350 mm

$Class_N = 1$, $Class_{M1} = 1$, $Class_{M2} = 1$

$$N_{cr,LT} = \frac{\pi^2 \cdot E \cdot I_z}{(k_z \cdot L_{cr})^2} = \frac{\pi^2 \cdot 2.100e+05 \cdot 4.492e+05}{(1.00 \cdot 2700)^2} = 127.71 \text{ kN}$$

Loaded on top edge.

$$Z = (C_2 \cdot z_g - C_3 \cdot z_j) = (0.45 \cdot 70 - 0.52 \cdot 0) = 31.50 \text{ mm}$$

$$M_{cr} = C_1 \cdot N_{cr,LT} \cdot \left\{ \left[\left(\frac{k_z}{k_w} \right)^2 \cdot \frac{I_w}{I_z} + \frac{G \cdot I_t}{N_{cr,LT}} + Z^2 \right]^{0.5} - Z \right\} =$$

$$= 1.13 \cdot 1.277e+05 \cdot \left\{ \left[\left(\frac{1.00}{1.00} \right)^2 \cdot \frac{1.951e+09}{4.492e+05} + \frac{8.077e+04 \cdot 2.401e+04}{1.277e+05} + 31.50^2 \right]^{0.5} - 31.50 \right\} =$$

$$= 16.13 \text{ kNm}$$

$$\bar{\lambda}_{LT} = \sqrt{\frac{W_y \cdot f_y}{M_{cr}}} = \sqrt{\frac{88344 \cdot 355}{1.613e+07}} = 1.39$$

$\alpha_{LT} = 0.21$ (Buckling curve: a)

$$\varphi_{LT} = 0.5 \left[1 + \alpha_{LT} \cdot (\bar{\lambda}_{LT} - 0.2) + \bar{\lambda}_{LT}^2 \right] =$$

$$= 0.5 \left[1 + 0.21 \cdot (1.39 - 0.2) + 1.39^2 \right] = 1.60$$

$$\chi_{LT} = \min\left(\frac{1}{\varphi_{LT} + \sqrt{\varphi_{LT}^2 - \bar{\lambda}_{LT}^2}}, 1.0 \right) = \min\left(\frac{1}{1.60 + \sqrt{1.60^2 - 1.39^2}}, 1.0 \right) = 0.42 \quad (6.56)$$

$$M_{y,b,Rd} = \chi_{LT} \cdot W_y \frac{f_y}{\gamma_{M1}} = 0.42 \cdot 88344 \frac{355}{1.00} = 13.19 \text{ kNm} \quad (6.55)$$

$$\frac{M_{1,Ed}}{M_{y,b,Rd}} = \frac{6.18}{13.19} = 0.47 \leq 1.00 \quad (6.54) \text{ - OK}$$

Interaction between normal force and bending 1. - Part 1-1: 6.3.3
LC: '6.10b_1', x = 1350 mm

$Class_N = 1$, $Class_{M1} = 1$, $Class_{M2} = 1$

k_{ij} factors are calculated according to Method 1

C_{my}	= 1.00	C_{yy}	= 1.00
C_{mz}	= 1.00	C_{yz}	= 0.84
C_{mLT}	= 1.00	C_{zy}	= 1.00
		C_{zz}	= 0.97

$$M_{2,Rk} = f_y \cdot W_{pl,2} = 355 \cdot 19260 = 6.84 \text{ kNm}$$

$$\frac{N_{Ed}^{comp}}{N_{b,Rd,1}} + k_{11} \cdot \frac{M_{1,Ed}}{M_{y,b,Rd}} + k_{12} \cdot \frac{M_{2,Ed}}{M_{2,Rk}} =$$

$$= \frac{0.08}{515.45} + 1.00 \cdot \frac{6.18}{13.19} + 0.82 \cdot \frac{0.00}{\frac{6.84}{1.00}} = 0.47 \leq 1.00 \quad (6.61) \text{ - OK}$$

Interaction between normal force and bending 2. - Part 1-1: 6.3.3
LC: '6.10b_1', x = 1350 mm

$Class_N = 1$, $Class_{M1} = 1$, $Class_{M2} = 1$

k_{ij} factors are calculated according to Method 1

C_{my}	= 1.00	C_{yy}	= 1.00
C_{mz}	= 1.00	C_{yz}	= 0.84
C_{mLT}	= 1.00	C_{zy}	= 1.00
		C_{zz}	= 0.97

$M_{2,Rk} = f_y \cdot W_{pl,2} = 355 \cdot 19260 = 6.84$ kNm

$$\frac{N_{Ed}^{comp}}{N_{b,Rd,2}} + k_{21} \cdot \frac{M_{1,Ed}}{M_{y,b,Rd}} + k_{22} \cdot \frac{M_{2,Ed}}{M_{2,Rk}} =$$

$$= \frac{0.08}{108.46} + 0.52 \cdot \frac{6.18}{13.19} + 1.03 \cdot \frac{\frac{0.00}{6.84}}{1.00} = 0.25 \leq 1.00 \quad (6.62) - \text{OK}$$

Interaction between normal force and bending, 2nd order - Part 1-1: 6.3.3
Not relevant

Shear buckling - Part 1-5: 5

$$\frac{h_w}{t} = \frac{126}{5} = 26.9 \leq \frac{72}{\eta} \cdot \varepsilon = \frac{72}{1.20} \cdot 0.81 = 48.8 \text{ --> Not relevant}$$

Summary

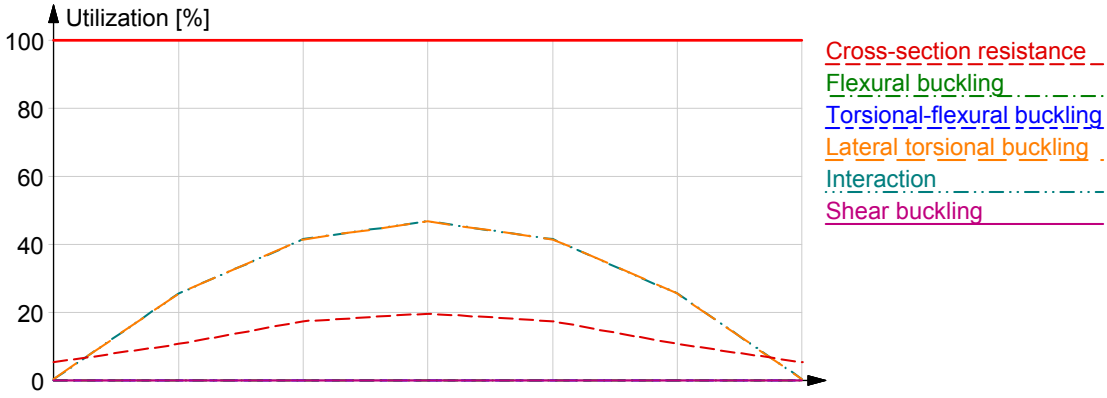

E Verification of the natural frequency (mode 1) of the Warren sub model

In this chapter, the first mode of the natural frequency of the Warren truss bridge is presented and compared with the results from FEM-Design and hand calculations. In Table E.1 the comparison of the results is presented, showing very similar results from Karamba 3D compared to FEM-Design and the hand calculations, having a weakening factor 1.

Table E.1: Natural frequency of mode 1 compared to FEM-Design and hand calculations.

	Natural frequency mode 1 [Hz]			Natural frequency mode 1 [Hz]		
Member	Karamba 3D 1*	FEM-Design	Difference	Karamba 3D 1*	Hand calculations	Difference
All	6.74	6.95	-3.2 %	6.74	6.71	0.4 %

*Weakening factor of the bridge deck is 1

The shapes of mode 1 in Karamba 3D and FEM-Design are presented below in Figure E.1 and Figure E.2 respectively and cohere well to each other. On the following pages, the hand calculations for the natural frequency of mode 1 for the Warren sub model is presented.

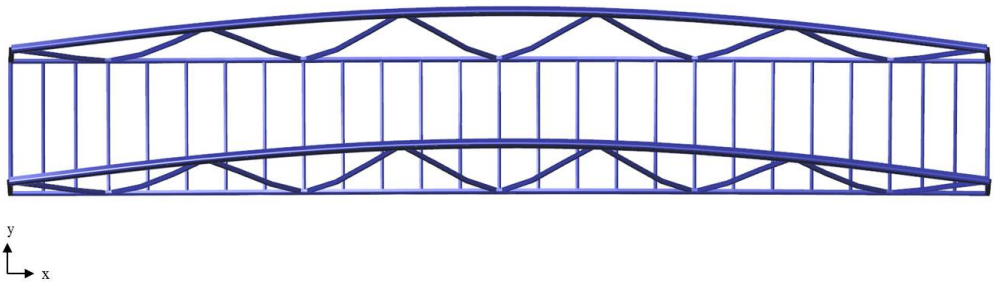

Figure E.1: Natural frequency (mode 1) for the Warren sub model in Karamba 3D.

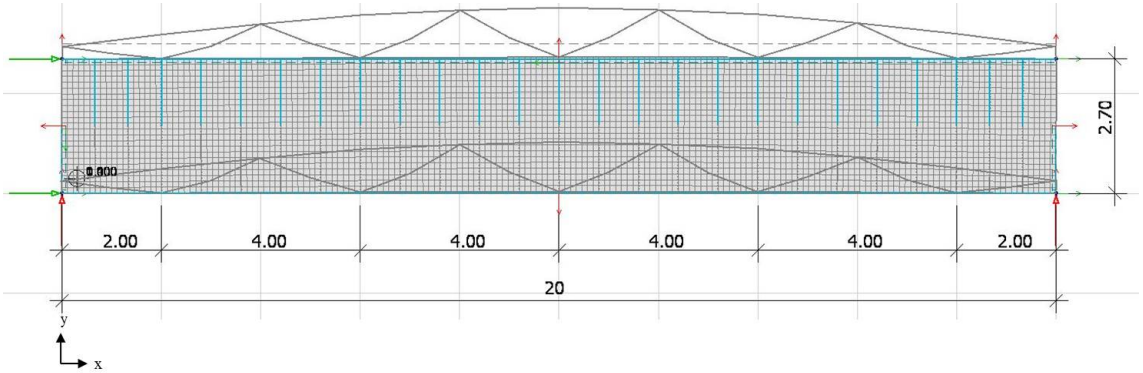

Figure E.2: Natural frequency (mode 1) for the Warren sub model in FEM-Design.

Calculation of natural frequency for Warren truss (mode 1)

Indata

$L_1 := 20 \cdot m$ Span length of the bridge

$m_1 := 8058.5 kg$ Mass of the Warren truss footbridge

$q := 5 \cdot \frac{kN}{m^2}$ Distributed load on the bridge (crowd load)

$b := 2.5 \cdot m$ Width of the bridge deck

$\delta_1 := 0.014236 m$ Displacement of the Warren truss footbridge with weakening factor 1

Stiffness calculation

$$K_1 := \frac{\left(\frac{q \cdot L_1 \cdot b}{2}\right) + m_1 \cdot g}{\delta_1} = 1.4 \times 10^7 \cdot \frac{N}{m}$$ Stiffness of the structure

$$\omega_1 := \sqrt{\frac{K_1}{m_1}} = 42.2 \cdot \frac{rad}{s}$$ Natural frequency in rad/s (equation from: Fundamentals of Structural Dynamics 2006)

$$f_1 := \frac{\omega_1}{2 \cdot \pi} = 6.7 \cdot Hz$$ Natural frequency of the Warren truss (mode 1)

F Verification of the Pratt sub model in Karamba 3D with FEM-Design

In this chapter the results from the verification of the Pratt truss sub model in Karamba 3D and FEM-Design are presented. In Figure F.1 the FEM-model for the Pratt truss bridge is presented, having the distances shown in meters.

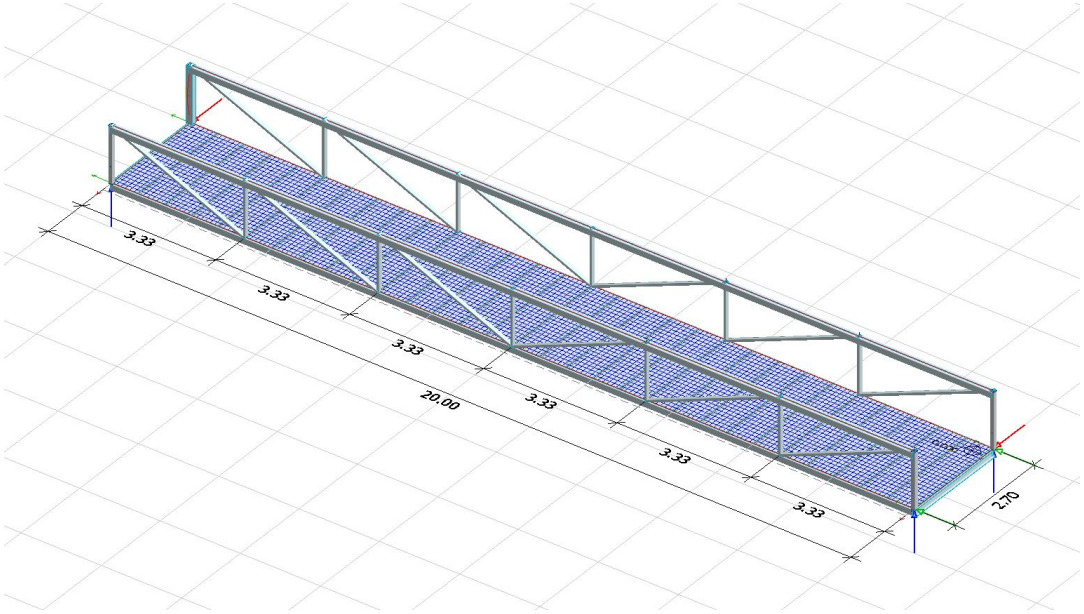

Figure F.1: The Pratt truss bridge modeled in FEM-Design. The distances are shown in meters.

In Figure F.2 the positions of the bridge are presented. The sectional forces, the reaction forces, the maximum displacement and the maximum utilization ratios are presented on the following pages, referring to the positions shown in Figure F.2. Also in this verification, load case 6.10b_1 is applied.

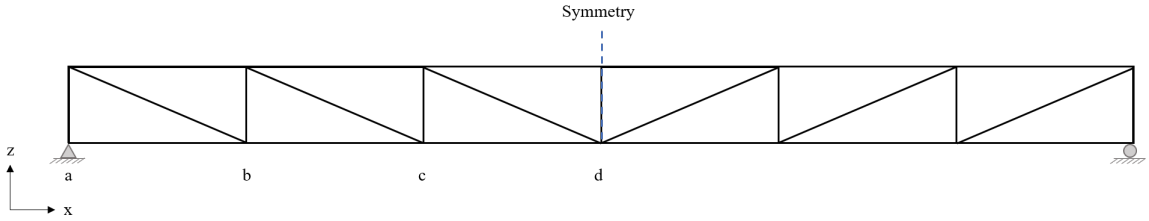

Figure F.2: Position identifications for the Pratt truss sub model.

Load case	6.10b1

			Normal force [kN] (absolute values)		
	Description	Member	Karamba 3D 10 000*	FEM-Design 10 000*	Difference
Normal force N	Bottom chord B.1/B.3	a-b	9,7	9,7	-0,9%
		b-c	251,1	252,1	-0,4%
		c-d	397,3	398,5	-0,3%
	Top chord B.2/B.4	a-b	249,2	250,1	-0,4%
		b-c	396,6	397,7	-0,3%
		c-d	446,3	447,3	-0,2%
	Diagonals	a-b	259,0	260,7	-0,7%
		b (verticals)	59,8	60,1	-0,5%
		b-c	157,5	158,1	-0,3%
		c (verticals)	21,9	22,0	-0,6%
		c-d	53,1	53,0	0,1%
	End posts	All 4	104,6	104,9	-0,3%
	Cross beams	b	0,2	0,2	
		d	0,1	0,0	

			Moment My [kNm] (absolute values)		
	Description	Member	Karamba 3D 10 000*	FEM-Design 10 000*	Difference
Moment My	Bottom chord	a/ k	8,1	8,2	-1,7%
		a-b	7,4	7,5	-1,7%
		b	10,2	10,3	-0,9%
		b-c	7,1	7,2	-0,4%
		c	8,3	8,4	-0,8%
		c-d	7,4	7,5	-1,3%
		d	8,4	8,5	-0,6%
	Top chord	a/ k	5,1	5,1	-0,4%
		b/ j	4,1	4,0	1,8%
		c/ i	2,9	3,0	-2,0%
		d/ h	2,8	2,8	0,4%
	Diagonals	a-b	0,2	0,2	
		b (verticals)	0,3	0,3	
		b-c	0,1	0,1	
		c (verticals)	0,1	0,1	
		c-d	0,0	0,0	
	End posts	All 4	8,1	8,2	-1,7%
			5,5	5,5	-0,4%
	Cross beams	b	4,8	4,7	1,9%
		d	4,9	4,9	0,2%

			Shear Vz [kN] (absolute values)		
	Description	Member	Karamba 3D 10 000*	FEM-Design 10 000*	Differemce
Shear force Vz	Bottom chord	a	15,8	16,8	-5,9%
		b	16,4	16,6	-1,5%
			16,9	17,1	-1,1%
		c	15,3	15,5	-1,5%
			16,1	16,1	-0,6%
		d	16,1	16,2	-0,9%
	Top chord	a-b	3,3	3,3	0,3%
	Diagonals	a-b	0,0	0,0	
		b (verticals)	0,2	0,2	
		b-c	0,0	0,0	
		c (verticals)	0,0	0,1	
		c-d	0,0	0,0	
	End posts	All 4	9,7	9,8	-1,1%
	Cross beams	b	7,24	7,17	1,0%
		d	7,22	7,17	0,7%

			Reaction force of one support [kN]		
Reaction forces	Load	Member	Karamba 3D 10 000*	FEM-Design 10 000*	Difference
	Self-weight	All	20,38	20,73	-1,7%

			Max. displacement ULS [m]		
Displacement	Description	Member	Karamba 3D 10 000*	FEM-Design 10 000*	Difference
	Max. displacement [mm]	All	57,89	57,85	0,1%

			Maximum utilization ratio		
Maximum utilization ratio	Description	Member	Karamba 3D 10 000*	FEM-Design 10 000*	Difference
	With adjustment of the buckling length of the cross beams	Bottom chord	51,7%	54,0%	-2,3%
		Top chord	47,2%	48,0%	-0,8%
		Vertical end post	51,6%	53,0%	-1,4%
		Diagonal (a-b)	52,1%	53,0%	-0,9%
		Cross beams (f)	30,6%	37,0%	-6,4%
		End cross beams	13,1%	14,0%	-0,9%

10 000 Bridge deck is weakened with a factor of 10 000*

G Verification of the Howe sub model in Karamba 3D with FEM-Design

In this section the results from the Howe truss sub model in Karamba 3D and the corresponding FEM-Design sub model, shown in Figure G.1, considering the sectional forces are presented and compared. The load cases used for verification are $6.10b_1$. In Figure G.2 the positions, where sectional forces are studied on the next page, are shown.

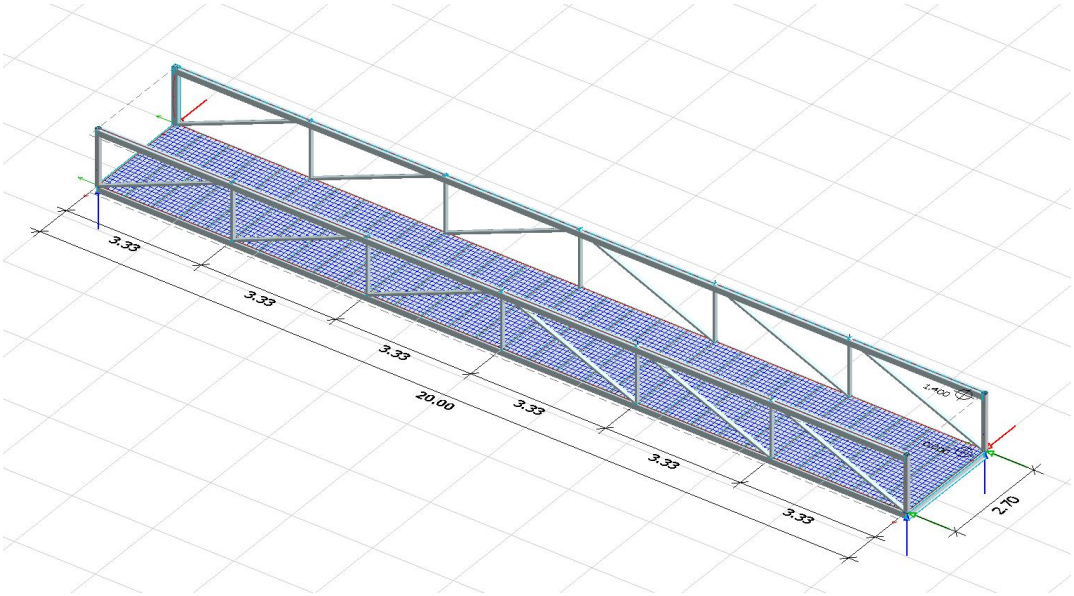

Figure G.1: The Howe truss bridge modeled in FEM-Design. The distances are shown in meters.

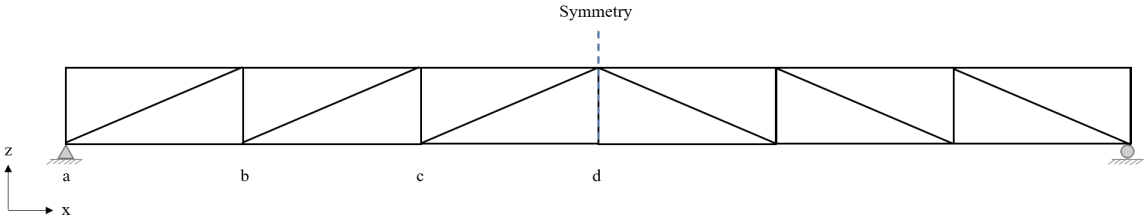

Figure G.2: Position identifications for the Howe truss sub model.

Load case	6.10b1

			Normal force [kN] (absolute values)		
	Description	Member	Karamba 3D 10'000*	FEM-Design 10'000*	Difference
Normal force N	Bottom chord	a-b	249,24	249,8	-0,2%
		b-c	396,4	397,0	-0,2%
		c-d	444,9	445,6	-0,2%
	Top chord	a-b	9,41	9,53	-1,3%
		b-c	251,6	252,1	-0,2%
		c-d	397,8	398,5	-0,2%
	Diagonals	a-b	260,3	260,7	-0,1%
		b (verticals)	101,6	102,0	-0,4%
		b-c	157,3	157,4	-0,1%
		c (verticals)	59,1	59,4	-0,5%
		c-d	51,4	51,5	-0,2%
		d	38,9	39,1	-0,5%
	End posts	All 4	3,6	3,6	0,8%
	Cross beams	b	0,19	0,25	
		d	0,06	0,02	

			Moment My [kNm] (absolute values)		
	Description	Member	Karamba 3D 10'000*	FEM-Design 10'000*	Difference
Moment My	Bottom chord	a/ k	8,2	8,06	1,9%
		a-b	7,3	7,49	-2,1%
		b	10,3	10,3	-0,5%
		b-c	7,1	7,01	1,1%
		c	8,6	8,62	0,0%
		c-d	7,7	7,67	0,3%
		d	7,7	7,75	-0,1%
	Top chord	a/ k	5,2	5,3	-0,4%
		b/ j	4,0	4,0	0,2%
		c/ i	2,9	3,0	-1,3%
		d/ h	3,8	3,7	0,3%
	Diagonals	a-b	0,2	0,2	
		b (verticals)	0,4	0,4	
		b-c	0,0	0,0	
		c (verticals)	0,1	0,1	
		c-d	0,0	0,0	
		d	0,1	0,1	
	End posts	All 4	7,9	8,2	-2,7%
			5,2	5,4	-2,8%
	Cross beams	b	4,8	4,79	-0,6%
		d	4,7	4,9	-3,9%

			Shear Vz [kN] (absolute values)		
	Description	Member	Karamba 3D 10 000*	FEM-Design 10 000*	Differemce
Shear force Vz	Bottom chord	a	15,9	16,11	-1,3%
		b	16,3	16,70	-2,7%
			16,8	17,10	-1,5%
		c	15,3	15,66	-2,3%
			16,3	16,62	-1,7%
		d	15,8	16,14	-2,0%
	Top chord	a-b	3,3	3,33	0,3%
	Diagonals	a-b	0,1	0,06	
		b (verticals)	0,2	0,28	
		b-c	0,0	0,01	
		c (verticals)	0,0	0,12	
		c-d	0,0	0,01	
		d	0,03	0,01	
	End posts	All 4	9,4	9,68	-2,8%
	Cross beams	b	7,24	6,78	6,8%
		d	7,2	6,75	6,7%

			Reaction force of one support [kN]		
Reaction forces	Load	Member	Karamba 3D 10 000*	FEM-Design 10 000*	Difference
	Self-weight	All	20,38	20,85	-2,2%

			Max. displacement ULS [m]		
Displacement	Description	Member	Karamba 3D 10 000*	FEM-Design 10 000*	Difference
	Max. displacement [mm]	All	61,0	60,7	0,5%

			Maximum utilization ratio		
Maximum utilization ratio	Description	Member	Karamba 3D 10 000*	FEM-Design 10 000*	Difference
	With adjustment of the buckling length of the cross beams	Bottom chord	56,6%	60,0%	-3,4%
		Top chord	43,3%	45,0%	-1,7%
		Vertical end post	35,9%	37,0%	-1,1%
		Diagonal (a-b)	229,2%	226,0%	3,2%
		Cross beams (f)	30,6%	37,0%	-6,4%
		End cross beams	13,2%	13,0%	0,2%

10 000 Bridge deck is weakened with a factor of 10 000*

H Calculation of the global lateral torsional buckling of the top chord

In this chapter the hand calculations of the global lateral torsional buckling of the top chord of the Warren sub model, according to SS-EN 1993-2 chapter 6.3.4.2 (2) and (Wahlström, 1971), are presented. In Figure H.1 it can be seen how the unit load of 1 000 kN is applied on the different sub models. The purpose is to calculated the displacement of the truss where the unit load is applied, which concludes in the results of the stiffness of the springs that the top chord lies on. Finally, the reduced normal capacity of the top chord, N_{bRd}, can be calculated, which corresponds to the maximum value that the maximum normal force in the top chord, N_{ED}, must not exceed.

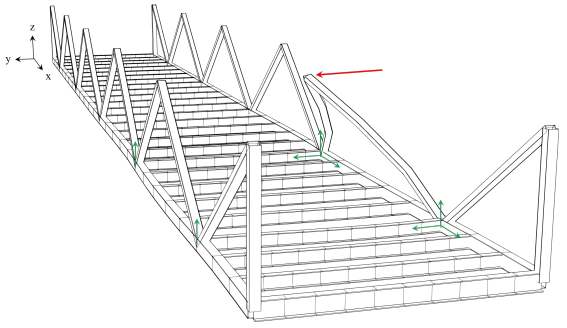

(a)

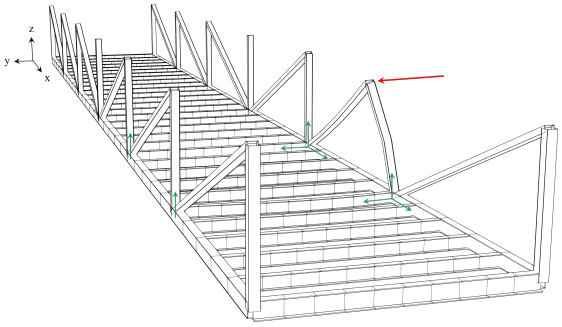

(b)

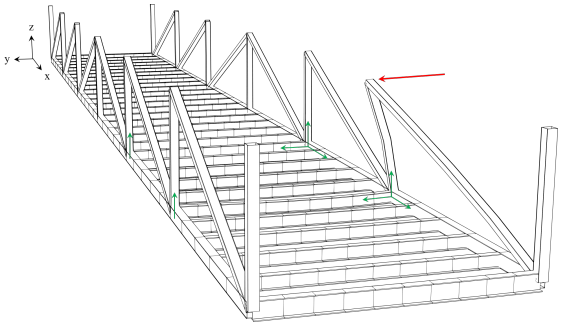

(c)

Figure H.1: The three sub model without the top chords. A unit load of 1 000 kN is applied to calculated the displacement in y-direction. (a) The Warren sub model (b) The Pratt sub model (c) The Howe sub model

Global control of buckling of the top chord

According to SS-EN 1993-2 chapter 6.3.4.2 (2) and
Bygg Handbok för hus-, väg- och vattenbyggnad (Allmänna grunder del 1A, main author: Civilengineer SVR Bengt Wahlström, publisher: AB Byggmästarens förlag, Stockholm 1971).

To check the utilization of the top chord globally when it comes to buckling sideways, the top chord is modelled as column with a normal compression force N.ED, getting some support from the truss system, the cross beams and the bottom chord, which are connected to each other and give some stiffness. This contribution of stiffness is simulated as a bed of springs with a certain spring stiffness.

Indata

$N_{ED} := 435kN$ Maximum normal force from Karamba 3D in the top chord

$f_y := 355 \cdot MPa$

$E := 210 \cdot GPa$

$A_{topchord} := 3580mm^2$

$L_{topchord} := 20m$

$n_{triangles} := 5$

$\gamma_{M1} := 1$

$I_{topchord.z} := 1223 \cdot 10^4 (mm)^4$ (weak axis)

Calculation procedure

$N_{unit} := 1000kN$

$\delta_{unitload} := 7.061m$ The value is taken from the Karamba 3D model of a Warren truss bridge of 20 m length and without a top chord. When appying a unit load of 1000 kN, the displacement sideways becomes δ.unitload.

$C_{unitload} := \frac{1000kN}{\delta_{unitload}} = 141.6 \cdot \frac{kN}{m}$ spring stiffness (sideways)

$a := \frac{L_{topchord}}{n_{triangles}} = 4\,m$ Distance between the connections of the diagonals to the top chord.

Fig :362g. [51]

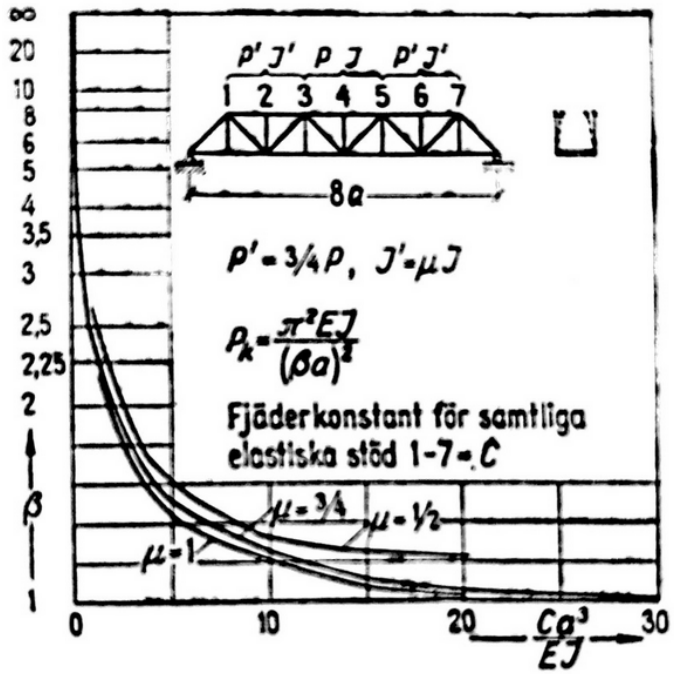

Fig :362i. Öppen fackverksbro i 8 fack. Sidoknäckningslast för tryckt övre horisontal vid jämnt fördelad last över hela bron [52]

The figure is taken from Bygg (Huvuddel 1A), page 664. With the quote calculated in equation (1) below, the beta-value can be retrieved.

$$\frac{C_{unitload} \cdot a^3}{E \cdot I_{topchord.z}} = 3.5$$ equation (1)

$\beta := 1.61$ From figure 362i

$$N_{cr} := \frac{\pi^2 \cdot E \cdot I_{topchord.z}}{(\beta \cdot a)^2} = 611.2 \cdot kN$$ According to (Wahlstrom, 1971)

$$\lambda_{LT} := \left(\frac{A_{topchord} \cdot f_y}{N_{cr}} \right)^{\frac{1}{2}} = 1.4$$ Accroding to SS-EN 1993-1-1 6.3.1.4 (2)

$L_{cr} := \beta \cdot a = 6.4\,m$

$\alpha_{LT} := 0.21$ Buckling curve a, varm calsed S355 steel
Accroding to SS-EN 1993-1-1 Table 6.2

$\phi_{LT} := 0.5 \cdot \left[1 + \alpha_{LT} \cdot \left(\lambda_{LT} - 0.2 \right) + \lambda_{LT}^{2} \right] = 1.7$ Accroding to SS-EN 1993-1-1 6.3.2.2 (1)

$$\chi_{LT} := \frac{1}{\phi_{LT} + \left(\phi_{LT}^{2} - \lambda_{LT}^{2} \right)^{\frac{1}{2}}} = 0.4$$ Accroding to SS-EN 1993-1-1 6.3.2.2 (1)

$$N_{bRd} := \frac{\chi_{LT} \cdot f_y \cdot A_{topchord}}{\gamma_{M1}} = 505.8 \cdot kN$$ Accroding to SS-EN 1993-1-1 6.3.1.1 (3)

$$Utilization := \frac{N_{ED}}{N_{bRd}} = 0.9$$ Smaller than 1 --> OK

I All optimization results for part 1 and part 2

In this section all results obtained from the optimization simulations for Warren, Pratt and Howe trusses for part 1 and part 2 are presented. Below, see Table I.1, the procedure of part 1 is presented followed by the procedure of part 2, see Table I.2 to get an overview. On the following pages, all optimization results from both part 1 and part 2 are presented.

Table I.1: Procedure of the optimization of part 1.

Plug-in	Optimization run	Cross section	Topology	Fitness function	Repetitions
Galapagos	A		x	Mass	1
	B	x		Mass	1
	C	x	x	Mass	3
	D		x	Transparency	1
	E	x		Transparency	1
	F	x	x	Transparency	3
Octopus	G	x	x	Mass and transparency	3

Table I.2: Procedure of the optimization of part 2.

Plug-in	Span length	Geometry	Cross section	Topology	Fitness function	Repetitions
Octopus	10 m	all 3	x	x	Mass and transparency	3
	20 m	all 3	x	x	Mass and transparency	3
	30 m	all 3	x	x	Mass and transparency	3

Settings for Galapagos	
Fitness	minimize
Max. Stagnant	50
Maintain	5%
Inbreeding (+)	75%
Population	100
Initial boost	2

Settings for Octopus	
Elitism	0,5
Mutation probabilty	0,1
Mutation rate	0,5
Cross over rate	0,8
Population	100
Initial boost	2

	Min	Max
nΔ	1	20
ncb	1	10

Height and width of the truss bridges are kept constant. First order analysis is used in Karamba 3D.
The start of every optimization run is with the perquisites from the case study.

*when optimizing only topology the cross sections are fixed to the values from the case study
**Irrelevant as the side view area is not considering the area of the cross beams
Best solution

	Plug-in	*Case study 20 m*	***Galapagos***										
	Geometry	*Warren*	*Warren*										
	Load case	*6.10b1 (ULS)*	*6.10b1 (ULS)*										
	Fitness function	-	*Mass*	*Mass*	*Mass*	*Mass*	*Mass*	*Transparency*	*Transparency*	*Transparency*	*Transparency*	*Transparency*	
	Optimization runs	-	*A*	*B*	*C*	*C*	*C*	*D*	*E*	*F*	*F*	*F*	
	Cross section	-	-	*x*	*x*	*x*	*x*	-	*x*	*x*	*x*	*x*	
	Topology	-	*x*	-	*x*	*x*	*x*	*x*	-	*x*	*x*	*x*	
	nΔ	5	6	5	6	6	6	5	*	5	5	5	
	ncb	5	2	5	1	1	1	16	*	6	6	6	
	Bottom chord	VKR 150x100x6.3	*	VKR 120x120x5	VKR120x60x4	VKR 120x60x4	VKR 120x60x4	*	VKR 120x80x8	VKR 100x100x8	VKR 100x100x8	VKR 100x100x10	
	Top chord	VKR 150x150x6.3	*	VKR 150x150x5	VKR 140x140x5	VKR 140x140x6	VKR 140x140x7	*	VKR 120x120x8	VKR 120x120x10			
	Diagonals	VKR 100x60x5	*	VKR 120x60x3.6	VKR 100x60x3.6	VKR 100x60x3.7	VKR 100x60x3.8	*	VKR 100x60x5.6	VKR 120x60x3.6	VKR 100x60x5.6	VKR 100x60x5	
	Vertical end posts	VKR 100x100x5	*	VKR 100x60x3.6	VKR 120x120x4.5	VKR 100x100x4	VKR 100x100x5	*	IPE 120	KCKR 76.1/4		KCKR 76.1/5	
	Cross beams	IPE 140	*	KCKR 76.1/4	VKR 120x120x4.5	VKR 120x120x4.6	VKR 120x120x4.7	*	VKR 150x100x6.3	VKR 120x80x6.3	VKR 120x60x3.6	VKR 100x60x5.6	
	End cross beams	IPE 180	*	KCKR 40.4/3	VKR 100x100x4	VKR 100x100x5	VKR 100x100x6	*	VKR 150x150x5	VKR 180x100x8	VKR 180x100x5.6	VKR 160x80x10	
20 m (Galapagos)	Displacement	0,021	0,012	0,021	0,017	0,017	0,017	0,010	0,011	0,012	0,012	0,012	
	Max. displacement	0,05	0,05	0,05	0,05	0,05	0,05	0,05	0,05	0,05	0,05	0,05	
	Utilization displacement	41%	23%	41%	34%	35%	35%	21%	22%	24%	24%	23%	
	Element where the max utilization ratio occurs	-				Bottom chord	Bottom chord				Bottom chord	Diagonal	
	Utilization ratio	65%	74%	84%	82%	82%	82%	71%	74%	82%	78%	74%	
	Max allowable utilization ratio	85%	85%	85%	85%	85%	85%	85%	85%	85%	85%	85%	
	Utilizaiton of utilization	77%	88%	99%	96%	96%	96%	84%	87%	97%	92%	88%	
	Ned [kN] (Max normal force in top chord)	435	425	426	371	371	371	467	445	455	450	454	
	NbRd [kN] (Max allowable normal force in top chord)	507	607	454	426	426	426	517	449	506	448	458	
	Utilization normal force (top chord)	86%	70%	94%	87%	87%	87%	90%	99%	90%	100%	99%	
	Area [m2]	7,74	7,85	7,14	7,10	7,05	7,05	7,74	6,60	6,08	6,08	6,08	
	Mass [kg]	8058	7602	7007	6490	6466	6466	9973	8785	8781	8204	8653	

	Plug-in	***Octopus***											
	Geometry	*Warren*											
	Fitness function	*Mass and trasparency*											
	Load case	*6.10b1 (ULS)*											
	Fitness function	*Mass and trasparency*											
	Optimization runs	*G*											
	Cross section	*x*											
	Topology	*x*											
	nΔ			6			6			5	6		6
	ncb			2			2			1	1		1
	Bottom chord			VKR 100x100x6.3			VKR 100x100x6.3			VKR 100x100x4	VKR 100x100x4		VKR 100x100x4
	Top chord			VKR 100x100x10			VKR 120x120x5			VKR 100x100x10	VKR 100x100x8		VKR 120x120x4.5
	Diagonals			VKR 120x60x3.6			VKR 120x60x4			VKR 120x60x3.6	VKR 100x60x3.6		VKR 100x60x4
	Vertical end posts			KCKR 76.1/5			KCKR 76.1/4			VKR 100x60x3.6	VKR 100x60x3.6		VKR 100x60x3.6
	Cross beams			VKR 120x60x3.6			VKR 120x60x3.6			KCKR 219.1/12.5	KCKR 219.1/12.5		KCKR 219.1/12.5
	End cross beams			IPE 120			IPE 120			VKR 100x60x3.6	VKR 100x60x3.6		VKR 100x60x3.6
20 m (Octopus)	Displacement [m] SLS	0,016	0,016	0,016	0,016	0,018	0,018	0,016	0,018	0,012	0,013	0,014	0,015
	Max allowable displacement [m] SLS 6.15ab1	0,05	0,05	0,05	0,05	0,05	0,05	0,05	0,05	0,05	0,05	0,05	0,05
	Utilization of displacement	31%	31%	33%	33%	35%	37%	33%	37%	25%	26%	28%	29%
	Element where the max utilization ratio occurs	Bottom chord	Bottom chord	End cross beam			End cross beam		End cross beam	Top chord		Top chord	Top chord
	Utilization ratio	80%	78%	83%	81%	77%	82%	82%	82%	83%	73%	75%	78%
	Max allowable utilization ratio	85%	85%	85%	85%	85%	85%	85%	85%	85%	85%	85%	85%
	Utilizaiton of utilization	94%	91%	97%	95%	90%	97%	97%	97%	97%	86%	88%	92%
	Ned [kN] (Max normal force in top chord)	426	410	422	422	406	419	423	419	381	373	386	371
	NbRd [kN] (Max allowable normal force in top chord)	433	429	429	429	410	420	440	420	390	374	395	379
	Utilization normal force (top chord)	98%	96%	98%	98%	99%	100%	96%	100%	98%	100%	98%	98%
	Mass	7314	7209	7087	7087	6825	6748	7132	6748	6690	6509	6402	6290
	Area	5,78	5,78	5,78	5,82	6,18	6,18	5,78	6,18	5,75	5,85	5,96	6,25
	Solution	1	2	3	4	5	6	7	8	9	10	11	12
	Repeated	-	-	-	-	-	-		x (reset)				

Fitness function	*Mass and trasparency*
Load case	*6.10b1 (ULS)*
Optimization run	*G*
Cross section	*x*
Topology	*x*

Span length 10 m (OCTOPUS)

Geometry	**Warren**								
nΔ	3	3	3	3	3	3	3	3	3
ncb	2	1	1	2	1	1	2	1	1
Bottom chord	VKR 100x60x4	VKR 100x60x3.6	VKR 100x60x3.6	VKR 100x60x4	VKR 100x60x3.6	VKR 100x60x3.6	VKR 100x60x4	VKR 100x60x3.6	VKR 100x60x3.6
Top chord	KCKR 88.9/5	KCKR 88.9/4	KCKR 88.9/4	KCKR 88.9/5	KCKR 88.9/4	KCKR 88.9/4	KCKR 88.9/5	KCKR 88.9/4	KCKR 88.9/4
Diagonals	VKR 100x60x3.6	VKR 100x60x3.6	VKR 100x60x3.6	VKR 100x60x3.6	VKR 100x60x3.6	VKR 100x60x3.6	VKr 100x60x3.6	VKR 100x60x3.6	VKR 100x60x3.6
Vertical end posts	KCKR 40.4/4	KCKR 40.4/4	KCKR 48.3/3	KCKR 40.4/4	KCKR 40.4/4	KCKR 48.3/3	KCKR 40.4/4	KCKR 40.4/4	KCKR 48.3/3
Cross beams	IPE 160	VKR 100x100x5	VKR 100x100x5	IPE 160	VKR 100x100x5	VKR 100x100x5	VKR 100x100x5	VKR 100x100x5	VKR 100x100x5
End cross beams	VKR 140x70x4	VKR 100x60x3.6	VKR 100x60x3.6	VKR 140x70x4	VKR 100x60x3.6	VKR 100x60x3.6	VKR 100x60x3.6	VKR 100x60x3.6	VKR 100x60x3.6
Displacement [m] SLS	0,006	0,009	0,009	0,006	0,009	0,009	0,008	0,009	0,009
Max allowable displacement [m] SLS 6.15ab1	0,025	0,025	0,025	0,025	0,025	0,025	0,025	0,025	0,025
Utilization of displacement	23%	37%	37%	23%	37%	37%	33%	37%	37%
Element where the max utilization ratio occurs	Vertical end post	Cross beam	Cross beam	Vertical end post	Cross beam	Cross beam	Vertical end post	Cross beam	Cross beam
Utilization ratio	84%	78%	78%	84%	78%	78%	84%	78%	78%
Max allowable utilization ratio	85%	85%	85%	85%	85%	85%	85%	85%	85%
Utilizaiton of utilization	99%	91%	91%	99%	91%	91%	99%	91%	91%
Ned [kN] (Max normal force in top chord)	111	91	91	111	91	91	111	91	91
NbRd [kN] (Max allowable normal force in top chord)	140	118	118	140	118	118	140	118	118
Utilization normal force (top chord)	79%	77%	77%	79%	77%	77%	79%	77%	77%
Mass [kg]	3096	2921	2919	3096	2921	2919	3059	2921	2919
Transparency (side view area) [m2]	2,79	2,79	2,81	2,79	2,79	2,81	2,79	2,79	2,81
Solution	1	2	3	4	5	6	7	8	9
Repeated	-	-	-	x	x	x		x	x

Geometry	**Pratt**										
nΔ	4			3	4		3	4			3
ncb	1			1	1		1	1			1
Bottom chord	KCKR 40.4/4			KCKR 40.4/3	KCKR 40.4/3		KCKR 40.4/3	KCKR 40.4/3			KCKR 40.4/3
Top chord	KCKR 101.6/6			KCKR 88.9/4	KCKR 101.6/6		KCKR 88.9/4	KCKR 101.6/6			KCKR 88.9/4
Diagonals	KCKR 40.4/3			KCKR 60.3/4	KCKR 40.4/3		KCKR 60.3/4	KCKR 40.4/3			KCKR 60.3/4
Vertical end posts	KCKR 48.3/4			KCKR 60.3/3	KCKR 48.3/4		KCKR 60.3/3	KCKR 48.3/4			KCKR 60.3/3
Cross beams	KCKR 139.7/4			KCKR 139.7/4	KCKR 139.7/4		KCKR 139.7/4	KCKR 139.7/4			KCKR 139.7/4
End cross beams	KCKR 114.3/4			KCKR 101.6/4	KCKR114.3/4		KCKR 101.6/4	KCKR114.3/4			KCKR 101.6/4
Displacement [m] SLS	0,0075	0,0107	0,0076	0,0077	0,0077	0,0076	0,0077	0,0077	0,0080	0,0076	0,0077
Max allowable displacement [m] SLS 6.15ab1	0,025	0,025	0,025	0,025	0,025	0,025	0,025	0,025	0,025	0,025	0,025
Utilization of displacement	30%	43%	30%	31%	31%	30%	31%	31%	32%	30%	31%
Element where the max utilization ratio occurs	Vertical end post	End cross beam	Vertical end post	Bottom chord	Vertical end post	Vertical end post	Bottom chord	Vertical end post	Bottom chord	Vertical end post	Bottom chord
Utilization ratio	83%	82%	84%	75%	83%	84%	75%	83%	75%	84%	75%
Max allowable utilization ratio	85%	85%	85%	85%	85%	85%	85%	85%	85%	85%	85%
Utilizaiton of utilization	97%	97%	99%	88%	98%	99%	88%	98%	88%	99%	88%
Ned [kN] (Max normal force in top chord)	104	104	104	104	104	104	104	104	104	104	104
NbRd [kN] (Max allowable normal force in top chord)	107	107	110	110	107	110	110	107	107	110	110
Utilization normal force (top chord)	98%	98%	94%	94%	98%	94%	94%	98%	98%	94%	94%
Mass [kg]	2812	2779	2755	2754	2794	2755	2754	2794	2786	2755	2754
Transparency (side view area) [m2]	2,24	2,27	2,39	2,43	2,24	2,39	2,43	2,24	2,27	2,39	2,43
Solution	1	2	3	4	5	6	7	8	9	10	11
Repeated	-	-	-	-		x	x	x		x	x

Geometry	**Howe**		
nΔ	4	4	4
ncb	1	1	1
Bottom chord	VKR 100x60x3.6	IPE 80	IPE 80
Top chord	KCKR 76.1/4	KCKR 76.1/4	KCKR 76.1/4
Diagonals	VKR 100x60x3.6	VKR 100x60x3.6	VKR 100x60x3.6
Vertical end posts	KCKR 40.4/3	KCKR 40.4/3	KCKR 40.4/3
Cross beams	VKR 120x80x4	VKR 120x80x4	VKR 120x80x4
End cross beams	VKR 100x60x3.6	VKR 100x60x3.6	VKR 100x60x3.6
Displacement [m] SLS	0,0087	0,0088	0,0088
Max allowable displacement [m] SLS 6.15ab1	0,025	0,025	0,025
Utilization of displacement	35%	35%	35%
Element where the max utilization ratio occurs	Cross beam	Cross beam	Cross beam
Utilization ratio	83%	83%	83%
Max allowable utilization ratio	85%	85%	85%
Utilizaiton of utilization	98%	98%	98%
Ned [kN] (Max normal force in top chord)	79	79	79
NbRd [kN] (Max allowable normal force in top chord)	124	123	123
Utilization normal force (top chord)	64%	64%	64%
Mass [kg]	2912	2860	2860
Transparency (side view area) [m2]	2,82	2,62	2,62
Solution	1	2	3
Repeated	-		x

Fitness function	*Mass and trasparency*
Load case	*6.10b1 (ULS)*
Optimization run	*G*
Cross section	*x*
Topology	*x*

	Geometry	**Warren**											
	nΔ			6			6			5	6		6
	ncb			2			2			1	1		1
	Bottom chord			VKR 100x100x6.3			VKR 100x100x6.3			VKR 100x100x4	VKR 100x100x4		VKR 100x100x4
	Top chord			VKR 100x100x10			VKR 120x120x5			VKR 100x100x10	VKR 100x100x8		VKR 120x120x4.5
	Diagonals			VKR 120x60x3.6			VKR 120x60x4			VKR 120x60x3.6	VKR 100x60x3.6		VKR 100x60x4
	Vertical end posts			KCKR 76.1/5			KCKR 76.1/4			VKR 100x60x3.6	VKR 100x60x3.6		VKR 100x60x3.6
	Cross beams			VKR 120x60x3.6			VKR 120x60x3.6			KCKR 219.1/12.5	KCKR 219.1/12.5		KCKR 219.1/12.5
	End cross beams			IPE 120			IPE 120			VKR 100x60x3.6	VKR 100x60x3.6		VKR 100x60x3.6
	Displacement [m] SLS	0,016	0,016	0,016	0,016	0,018	0,018	0,016	0,018	0,012	0,013	0,014	0,015
	Max allowable displacement [m] SLS 6.15ab1	0,05	0,05	0,05	0,05	0,05	0,05	0,05	0,05	0,05	0,05	0,05	0,05
	Utilization of displacement	31%	31%	33%	33%	35%	37%	33%	37%	25%	26%	28%	29%
	Element where the max	Bottom chord	Bottom chord	End cross beam			End cross beam		End cross beam	Top chord		Top chord	Top chord
	Utilization ratio	80%	78%	83%	81%	77%	82%	82%	82%	83%	73%	75%	78%
	Max allowable utilization ratio	85%	85%	85%	85%	85%	85%	85%	85%	85%	85%	85%	85%
	Utilizaiton of utilization	94%	91%	97%	95%	90%	97%	97%	97%	97%	86%	88%	92%
	Ned [kN] (Max normal force in top chord)	426	410	422	422	406	419	423	419	381	373	386	371
	NbRd [kN] (Max allowable normal force in top chord)	433	429	429	429	410	420	440	420	390	374	395	379
	Utilization normal force (top chord)	98%	96%	98%	98%	99%	100%	96%	100%	98%	100%	98%	98%
	Mass	7314	7209	7087	7087	6825	6748	7132	6748	6690	6509	6402	6290
	Area	5,78	5,78	5,78	5,82	6,18	6,18	5,78	6,18	5,75	5,85	5,96	6,25
	Solution	1	2	3	4	5	6	7	8	9	10	11	12
	Repeated	-	-	-	-	-	-		x (reset)				
	Natural frequency [Hz]									3,5			5,0
	With IPE 180 as end cross beam [kg]												6345

	Geometry	**Pratt**							
	nΔ	6	6	5				5	5
	ncb	1	1	1				1	1
	Bottom chord	VKR 100x60x5	VKR 100x60x5	VKR 120x60x4				VKR 100x100x4	VKR 100x100x4
	Top chord	VKR 100x100x8	VKR 120x120x5	VKR 120x120x5				VKR 100x100x8	VKR 120x120x5
	Diagonals	VKR 100x60x3.6	VKR 100x60x3.6	VKR 100x60x3.6				VKR 100x60x3.6	VKR 100x60x3.6
	Vertical end posts	KCKR 76.1/4	KCKR 76.1/4	KCKR 76.1/4				KCKR 76.1/4	KCKR 76.1/4
	Cross beams	KCKR 168.3/4	KCKR 168.3/4	KCKR 168.3/4				VKR 160x80x4	VKR 160x80x4
	End cross beams	KCKR 101.6/4	KCKR 101.6/4	KCKR 101.6/4				VKR 100x60x3.6	VKR 100x60x3.6
	Displacement [m] SLS	0,019	0,020	0,021	0,019	0,020	0,021	0,019	0,021
	Max allowable displacement [m] SLS 6.15ab1	0,05	0,05	0,05	0,05	0,05	0,05	0,05	0,05
	Utilization of displacement	37%	41%	42%	37%	41%	42%	38%	41%
	Element where the max utilization ratio occurs	Top chord	Vertical end post		Top chord	Vertical end post		Top chord	Top chord
	Utilization ratio	82%	82%	83%	82%	82%	83%	82%	81%
	Max allowable utilization ratio	85%	85%	85%	85%	85%	85%	85%	85%
	Utilizaiton of utilization	96%	96%	98%	96%	96%	98%	96%	95%
	Ned [kN] (Max normal force in top chord)	425	422	422	425	422	422	425	422
	NbRd [kN] (Max allowable normal force in top chord)	442	455	455	442	455	455	438	452
	Utilization normal force (top chord)	96%	93%	93%	96%	93%	93%	97%	93%
	Mass	6524	6335	6300	6524	6335	6300	6510	6321
	Area	5,94	6,33	6,73	5,94	6,33	6,73	5,93	6,33
	Solution	1	2	3	4	5	6	7	8
	Repeated	-	-	-	x	x	x (reset)		

Span length 20 m (OCTOPUS)

	Geometry	**Howe**							
	nΔ	7		7	7		7	10	12
	ncb	2		2	2		2	1	1
	Bottom chord	VKR 100x100x6.3		VKR 120x120x4.5	VKR 100x100x6.3		VKR 120x120x4.5	VKR 100x100x4	VKR 100x100x4
	Top chord	VKR 100x100x5		VKR 100x100x5	VKR 100x100x5		VKR 100x100x5	VKR 100x100x5	VKR 100x100x5
	Diagonals	VKR 140x70x5		VKR 140x80x4	VKR 140x70x5		VKR 140x80x4	VKR 120x60x5	VKR 120x60x3.6
	Vertical end posts	KCKR 40.4/3		KCKR 40.4/3	KCKR 40.4/3		KCKR 40.4/3	KCKR 40.4/3	KCKR 40.4/3
	Cross beams	VKR 100x60x3.6		VKR 100x60x3.6	VKR 100x60x3.6		VKR 100x60x3.6	VKR 120x60x3.6	VKR 120x60x3.6
	End cross beams	KCKR 60.3/3		KCKR 60.3/3	KCKR 60.3/3		KCKR 60.3/3	VKR 100x60x3.6	VKR 100x60x3.6
	Displacement [m] SLS	0,019	0,019	0,020	0,019	0,019	0,020	0,023	0,022
	Max allowable displacement [m] SLS 6.15ab1	0,05	0,05	0,05	0,05	0,05	0,05	0,05	0,05
	Utilization of displacement	38%	39%	41%	38%	39%	41%	45%	44%
	Element where the max utilization ratio occurs	Top chord	Top chord	Top chord	Top chord	Top chord	Top chord	Cross beam	Bottom chord
	Utilization ratio	85%	85%	85%	85%	85%	85%	85%	83%
	Max allowable utilization ratio	85%	85%	85%	85%	85%	85%	85%	85%
	Utilizaiton of utilization	100%	100%	100%	100%	100%	100%	100%	98%
	Ned [kN] (Max normal force in top chord)	406	404	403	406	404	403	409	412
	NbRd [kN] (Max allowable normal force in top chord)	423	418	424	423	418	424	432	432
	Utilization normal force (top chord)	96%	97%	95%	96%	97%	95%	95%	95%
	Mass	7080	6928	6842	7080	6928	6842	6692	6573
	Area	6,41	6,74	7,14	6,41	6,74	7,14	6,34	6,61
	Solution	1	2	3	4	5	6	7	8
	Repeated	-	-	-	x	x	x (reset)	x	x

Fitness function	*Mass and trasparency*
Load case	*6.10b1 (ULS)*
Optimization run	*0*
Cross section	*x*
Topology	*x*

Span length 30 m (OCTOPUS)

Geometry	**Warren**																						
ns	12									12			11		11								
ncb	1									1			1		1								
Bottom chord										VKR 100x100x10			VKR 100x100x10		VKR 140x140x6.3								
Top chord										VKR 140x140x10			VKR 180x180x6.3		VKR 180x180x6.3								
Diagonals										VKR 120x60x3.6			VKR 100x60x4		VKR 100x60x4								
Vertical end posts										KCKR 76.1/5			KCKR 76.1/5		KCKR 76.1/5								
Cross beams										KCKR 139.7/4			KCKR 139.7/4		KCKR 139.7/4								
End cross beams										KCKR 101.6/4			KCKR 88.9/4		KCKR 88.9/4								
Displacement [m] SLS	0,035	0,035	0,036	0,036	0,036	0,036	0,037	0,037	0,038	0,035	0,035	0,036	0,036	0,037	0,037	0,038	0,035	0,035	0,036	0,036	0,037	0,037	0,038
Max allowable displacement [m] SLS 6.15ab1	0,075	0,075	0,075	0,075	0,075	0,075	0,075	0,075	0,075	0,075	0,075	0,075	0,075	0,075	0,075	0,075	0,075	0,075	0,075	0,075	0,075	0,075	0,075
Utilization of displacement	46%	46%	48%	49%	48%	48%	50%	50%	51%	46%	46%	48%	48%	50%	50%	51%	46%	46%	48%	48%	50%	50%	51%
Element where the max utilization ratio occurs	Vertical end post		Vertical end post		Vertical end post	Vertical end post	Diagonals	Diagonals	Bottom chord	Vertical end post		Vertical end post	Vertical end post	Diagonals	Diagonals	Diagonals	Vertical end post		Vertical end post	Vertical end post	Diagonals	Diagonals	Diagonals
Utilization ratio	79%	78%	81%	78%	82%	83%	84%	84%	81%	79%	78%	82%	83%	84%	84%	84%	79%	78%	82%	83%	84%	84%	84%
Max allowable utilization ratio	85%	85%	85%	85%	85%	85%	85%	85%	85%	85%	85%	85%	85%	85%	85%	85%	85%	85%	85%	85%	85%	85%	85%
Utilizaiton of utilization	94%	92%	96%	92%	97%	97%	99%	99%	96%	94%	92%	97%	97%	99%	99%	99%	94%	92%	97%	97%	99%	99%	99%
Ned [kN] (Max normal force in top chord)	926,5	926,5	922,7	932,3	924,2	924,2	919,4	919,4	917,1	926,5	926,5	924,2	924,2	919,4	919,4	916,8	926,5	926,5	924,2	924,2	919,4	919,4	916,8
NbRd [kN] (Max allowable normal force in top chord)	927,2	927,3	923,2	974,9	930,0	928,8	926,6	926,0	978,3	927,2	927,3	930,0	928,8	926,6	926,0	932,2	927,2	927,3	930,0	928,8	926,6	926,0	932,2
Utilization normal force (top chord)	100%	100%	100%	96%	99%	100%	99%	99%	94%	100%	100%	99%	100%	99%	99%	98%	100%	100%	99%	100%	99%	99%	98%
Mass [kg]	12051	12049	11831	11830	11799	11790	11567	11558	11521	12051	12049	11799	11790	11567	11558	11500	12051	12049	11799	11790	11567	11558	11500
Transparency (side view area) [m2]	10,12	10,15	10,42	10,54	10,59	10,63	11,19	11,23	12,39	10,12	10,15	10,59	10,63	11,19	11,23	12,39	10,12	10,15	10,59	10,63	11,19	11,23	12,39
Solution	1	2	3	4	5	6	7	8	9	10	11	12	13	14	15	16	10	11	12	13	14	15	16
Repeated	-	-	-	-	-	-	-	-	-	x	x	x	x	x	x		x	x	x	x	x	x	x
Natural frequency [Hz]	4,4															4,2							

Geometry	**Pratt**																				
ns	10							9	10						9	10					9
ncb	1							1	1						1	1					1
Bottom chord	VKR 100x100x10							VKR 140x140x6.3	VKR 100x100x10						VKR 140x140x6.3	VKR 100x100x10					VKR 140x140x6.3
Top chord	VKR 140x140x10							VKR 180x180x6.3	VKR 140x140x10						VKR 180x180x6.3	VKR 140x140x10					VKR 180x180x6.3
Diagonals	VKR 120x60x4							VKR 120x60x4	VKR 120x60x4						VKR 120x60x4	VKR 120x60x4					VKR 120x60x4
Vertical end posts	VKR 100x60x6.3							VKR 120x60x3.6	VKR 100x60x6.3						VKR 120x60x3.6	VKR 100x60x6.3					VKR 120x60x3.6
Cross beams	VKR 160x80x6.3							VKR 140x70x4	VKR 160x80x6.3						VKR 140x70x4	VKR 160x80x6.3					VKR 140x70x4
End cross beams	VKR 100x100x4							VKR 100x100x4	VKR 100x100x4						VKR 100x100x4	VKR 100x100x4					VKR 100x100x4
Displacement [m] SLS	0,038	0,039	0,040	0,040	0,040	0,041	0,043	0,044	0,038	0,039	0,039	0,040	0,040	0,043	0,044	0,038	0,040	0,396	0,043	0,044	
Max allowable displacement [m] SLS 6.15ab1	0,075	0,075	0,075	0,075	0,075	0,075	0,075	0,075	0,075	0,075	0,075	0,075	0,075	0,075	0,075	0,075	0,075	0,075	0,075	0,075	
Utilization of displacement	51%	52%	53%	53%	54%	55%	58%	58%	51%	52%	52%	53%	53%	58%	58%	51%	53%	527%	58%	58%	
Element where the max utilization ratio occurs	Diagonals							Bottom chord	Diagonals	Diagonals	Bottom chord	Bottom chord	Bottom chord	Cross beam	Bottom chord	Diagonals	Top chord	Vertical end post	Cross beam	Bottom chord	
Utilization ratio	82%	81%	81%	82%	82%	83%	84%	85%	82%	83%	81%	81%	80%	84%	85%	82%	81%	81%	84%	85%	
Max allowable utilization ratio	85%	85%	85%	85%	85%	85%	85%	85%	85%	85%	85%	85%	85%	85%	85%	85%	85%	85%	85%	85%	
Utilizaiton of utilization	97%	95%	95%	96%	96%	98%	99%	100%	97%	98%	95%	95%	94%	99%	100%	97%	95%	96%	99%	100%	
Ned [kN] (Max normal force in top chord)	992,2	990,2	988,8	988,8	984,2	983,9	979,2	967,9	992,2	990,2	990,2	988,8	985,0	979,2	976,9	992,2	988,8	986,4	979,2	976,9	
NbRd [kN] (Max allowable normal force in top chord)	1009,7	990,4	991,7	991,7	993,8	988,0	981,1	999,1	1009,7	990,8	990,4	992,2	1014,2	981,1	999,1	1009,7	993,4	1034,8	981,1	999,1	
Utilization normal force (top chord)	98%	100%	100%	100%	99%	100%	100%	97%	98%	100%	100%	100%	97%	100%	98%	98%	100%	95%	100%	98%	
Mass [kg]	12280	12236	12121	12116	11941	11939	11659	11592	12280	12234	12231	12131	11922	11659	11592	12280	12139	12035	11659	11592	
Transparency (side view area) [m2]	10,22	10,47	10,52	10,58	11,07	11,42	11,42	12,62	10,22	10,47	10,52	10,58	10,82	11,42	12,62	10,22	10,58	10,82	11,42	12,62	
Solution	1	2	3	4	5	6	7	8	9	10	11	12	13	14	15	16	17	18	19	20	
Repeated	-	-	-	-	-	-	-	-	x					x	x	x			x	x	

Geometry	**Howe**														
ns							14				14		13		
ncb							1				1		1		
Bottom chord							VKR 100x100x10				VKR 100x100x10		VKR 100x100x10		
Top chord							VKR 120x120x10				VKR 160x160x6.3		VKR 120x120x10		
Diagonals							VKR 140x70x6.3				VKR 160x80x4		VKR 160x80x4		
Vertical end posts							KCKR 40.4/3				KCKR 40.4/3		KCKR 40.4/3		
Cross beams							KCKR 139.7/4				VKR 120x60x4		KCKR 139.7/4		
End cross beams							VKR 140x70x4				VKR 120x60x3.6		VKR 120x60x3.6		
Displacement [m] SLS	0,040	0,039	0,040	0,040	0,041	0,043	0,040	0,039	0,040	0,041	0,044	0,040	0,040	0,041	0,044
Max allowable displacement [m] SLS 6.15ab1	0,075	0,075	0,075	0,075	0,075	0,075	0,075	0,075	0,075	0,075	0,075	0,075	0,075	0,075	0,075
Utilization of displacement	53%	52%	54%	53%	55%	57%	53%	52%	54%	55%	59%	53%	54%	55%	59%
Element where the max utilization ratio occurs							Bottom chord				Top chord	Bottom chord	Bottom chord		Top chord
Utilization ratio	85%	84%	84%	84%	84%	85%	85%	84%	84%	84%	85%	85%	84%	84%	85%
Max allowable utilization ratio	85%	85%	85%	85%	85%	85%	85%	85%	85%	85%	85%	85%	85%	85%	85%
Utilizaiton of utilization	100%	99%	99%	99%	99%	100%	100%	99%	99%	99%	99%	100%	99%	99%	99%
Ned [kN] (Max normal force in top chord)	982,2	976,4	974,0	972,4	971,7	967,0	982,2	976,4	974,0	971,7	966,2	982,2	974,0	971,7	966,2
NbRd [kN] (Max allowable normal force in top chord)	986,7	993,0	975,8	977,4	1035,2	1007,7	986,7	999,3	975,8	1035,2	997,4	986,7	975,8	1035,2	997,4
Utilization normal force (top chord)	100%	98%	100%	99%	94%	96%	100%	98%	100%	94%	97%	100%	100%	94%	97%
Mass [kg]	12909	12555	12374	12304	12298	12089	12909	12569	12374	12298	12027	12909	12374	12298	12027
Transparency (side view area) [m2]	10,50	10,63	11,04	11,17	11,64	12,24	10,50	10,60	11,04	11,64	12,24	10,50	11,04	11,64	12,24
Solution	1	2	3	4	5	6	7	8	9	10	11	12	13	14	15
Repeated	-	-	-	-	-	-	x		x	x		x	x	x	x